CGER-REPORT

ISSN 1341-4356

CGER-I057-2004

CGER'S SUPERCOMPUTER MONOGRAPH REPORT Vol.9

Vortices, Waves and Turbulence in a Rotating Stratified Fluid

Takeshi Miyazaki, Shinsuke Fujishima, Masahiro Yamamoto,
Qin Wei and Hideshi Hanazaki

Center for Global Environmental Research

National Institute for Environmental Studies, Japan

CGER-REPORT

ISSN 1341-4356

CGER-I057-2004

CGER'S SUPERCOMPUTER MONOGRAPH REPORT Vol.9

Vortices, Waves and Turbulence in a Rotating Stratified Fluid

Takeshi Miyazaki, Shinsuke Fujishima, Masahiro Yamamoto,
Qin Wei and Hideshi Hanazaki

Center for Global Environmental Research

National Institute for Environmental Studies, Japan

Supercomputer Steering Committee (FY2003):

Dr. Takashi Aoki (Meteorological Research Institute)
Prof. Yasumasa Kanada (University of Tokyo)
Prof. Akimasa Sumi (University of Tokyo)
Prof. Hiromasa Ueda (Kyoto University)
Dr. Tsuneyuki Morita* (NIES)/Dr. Masayuki Tamura (NIES)
Dr. Yasuhiro Sasano (NIES)
Dr. Masataka Watanabe (NIES)
Mr. Yoshimi Matsui (EIC/NIES)
Dr. Gen Inoue (CGER/NIES)

*Dr. Tsuneyuki Morita passed away in September, 2003.

Coordination for Resource Allocation of the Supercomputer (FY2003):

Dr. Gen Inoue (Director, CGER/NIES)
Dr. Yasumi Fujinuma (CGER/NIES)
Dr. Hiroyuki Oguma (CGER/NIES)
Ms. Kazue Kawamura (CGER/NIES)
Dr. Masayuki Katsumoto (CGER/NIES)

Maintenance of the Supercomputer System (FY2003):

Mr. Yoshimi Matsui (Director, EIC/NIES)
Dr. Kunihiko Shirai (Head, EIC/NIES)
Mr. Hiroaki Abe (EIC/NIES)
Mr. Takahiro Nemoto (EIC/NIES)

Operation of the Supercomputer System:

System Engineers of NEC

Editors:

Dr. Yasumi Fujinuma (Chief)
Mr. Naruhiko Miyamoto
Ms. Kimie Tanaka
Ms. Hiroko Kaizu

Copies available from:

Center for Global Environmental Research
National Institute for Environmental Studies
16-2 Onogawa, Tsukuba, Ibaraki 305-8506 Japan
Fax: +81-29-858-2645
E-mail: cgerpub@nies.go.jp
http://www-cger.nies.go.jp

Copyright 2004:

NIES: National Institute for Environmental Studies

This book is printed on recycled paper.

Foreword

The Center for Global Environmental Research (CGER) of National Institute for Environmental Studies (NIES), Japan was established in October 1990. The main objectives of CGER are to contribute broadly to the scientific understanding of global environmental changes and to elucidate and provide solutions for pressing environmental problems. CGER conducts global environmental research with interdisciplinary and international cooperation, provides research support facilities such as a supercomputer and databases, and offers to the public its own data derived from long-term monitoring of the global environment.

In the context of supporting research programs that require supercomputer resources, we provide supervision for Supercomputer Steering Committee on research programs and aid in publishing results of these activities. We accept proposals by scientists from NIES and other organizations for computational research associated with earth systems, such as climate modeling, atmospheric and oceanic environment modeling, geophysical fluid dynamics, and so on. Proposed research programs are evaluated by the Supercomputer Steering Committee, which consists of leading Japanese scientists in the fields of climate modeling, atmospheric chemistry, oceanic circulation, and computer science. After approval of a program, authorization for system usage is provided. In March 2002, we finished installing a newer supercomputer system, which has higher performance and delivered substantial results to the understanding of earth system mechanisms.

To promote dissemination of the results, we publish both an Annual Activity Report and occasional Monograph Reports. The Annual Activity Report presents a single year's results for all current research programs. Each Monograph Report presents integrated results of a completed research program. This Monograph Report presents the outcome in 1992 to 2003 of a collaborative project of the Mechanical Engineering and Intelligent Systems, University of Electro-Communications and the Institute of Fluid Science, Tohoku University. The results will help shed light on the mechanism of geophysical fluid dynamics.

We will continue to support the global environmental research with CGER's supercomputer resources and the dissemination of useful information on the results in coming years.

January 2004

Shuzo Nishioka
Executive Director
Center for Global Environmental Research
National Institute for Environmental Studies

Preface

The present volume of CGER'S SUPERCOMPUTER MONOGRAPH REPORT series is the ninth publication of research outcomes achieved by the users of the supercomputer facilities at the Center for Global Environmental Research (CGER) of the National Institute for Environmental Studies (NIES). The computer resources have been provided to Prof. Takeshi Miyazaki (Univ. Electro-Communications), Prof. Hideshi Hanazaki (Tohoku Univ.) and their group for studies of global climate change.

Geophysical flows are subjected to strong influence by the Coriolis force and the buoyancy force, and two types of coherent motion with different time scales are observed. Vortices with larger time scales persist for a long time, and their interactions dominate the dynamics of geophysical turbulence. Inertial gravity waves of a much smaller time scale are superimposed on the slow vortex motion. The authors explore the vortex dynamics on the slow manifold by developing a vortex-based turbulence model. Direct numerical simulations using a Contour Advective Semi-Lagrangian algorithm (CASL) are performed in order to validate the model. The proposed model captures the essential mechanisms of the energy and momentum transport in geophysical turbulence. The fundamental aspects of stratified/rotating turbulence of smaller time scales are also investigated. The characteristics of stratified/rotating turbulence is strongly affected by the 'wave' components generated by the restoring forces, such as the buoyancy force and the Coriolis force. These wave effects, which have been studied extensively by the authors in this research project, but have often been ignored in the 'traditional' studies on turbulence, will make fundamental change in the future re-development of the turbulence models for geophysical flows.

I hope this publication contributes to further progress in the research of global environmental change, especially of global warming research.

January 2004

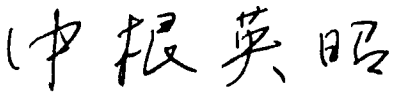

Hideaki Nakane
Head, Atmospheric Physics Section
Atmospheric Environment Division
National Institute for Environmental Studies

Contents

List of Figures

List of Tables

CGER'S SUPERCOMPUTER MONOGRAPH REPORT Vol.9
CGER-I057-2004, CGER/NIES

Vortices, Waves and Turbulence in a Rotating Stratified Fluid

Takeshi MIYAZAKI[1], Shinsuke FUJISHIMA[1], Masahiro YAMAMOTO[1],
Qin WEI[1] and Hideshi HANAZAKI[2]

[1]*Dept. Mech. Eng. and Intelligent Systems, Univ. of Electro-Commun., 1-5-1, Chofugaoka, Chofu, Tokyo, 182-8585, Japan*

[2]*Inst. Fluid Science, Tohoku Univ., 2-1-1, Katahira, Aoba-ku, Sendai, 980-8577, Japan*

Abstract

Two types of coherent motion with different time scale are observed in geophysical flows, which are subjected to strong influence of the Coriolis force and the buoyancy force. Vertical vortex structures with larger time scale persist for long time and their interactions dominate the dynamics of geophysical turbulence on 'slow manifold'. On the other hand, inertial gravity waves of much smaller time scale are excited and superimposed on the 'slow vortex motions'. Both vortices and waves contribute to transport of momentum, energy and scalar quantities in geophysical turbulence. We investigate the dynamical characteristics of vortices, waves and turbulence with their contribution to scalar transport phenomena. In chapter 1 the dynamics on the slow manifold is investigated, based on the quasigeostrophic approximation. Recently, Meacham *et al.* obtained a series of exact unsteady solution of the quasigeostrophic equation, which represents a uniform ellipsoidal vortex patch embedded in a uniform 3D shear field. A Hamiltonian dynamical system describing the interactions of N ellipsoidal vortices is introduced, where each coherent vortex is modeled by Meacham's ellipsoid. The equations of motion are derived following the procedure of Hamiltonian moment reduction. The center of vorticity and the angular momentum are conserved, besides the total energy and Casimirs of the system, such as the vortex height and the vortex volume. The degree of freedom of N interacting vortices is $3N$, whereas we have only three Poisson commutable invariants. Then even a two-body system shows chaotic behavior and the ellipsoidal moment model can predict merger of a co-rotating vortex pair placed within a critical distance. Direct numerical simulations based on a Contour Advective Semi-Lagrangian algorithm (CASL) are performed in order to assess the validity (and limitation) of the ellipsoidal moment model. In Chapter 2 we have investigated the 'unsteady' aspects of stratified/rotating turbulence which originate from the 'wave' components of the fluid motion. These wave components are generated by the buoyancy/Coriolis forces, which are usually the sources of internal/inertial waves. The unsteady aspects have been often ignored in the previous studies on the turbulent viscosity/diffusion, but our results show that they are, together with the initial conditions, often crucial to the long-time development of stratified/rotating turbulence. We have used Rapid Distortion Theory (RDT) for the theoretical investigation, and compared the results with the numerical simulations and the laboratory experiments.

Keywords: Stratified/rotating turbulence, Rapid distortion theory, Scalar transport, Quasigeostrophic turbulence, Coherent vortex structures, Ellipsoidal moment model, Instability of ellipsoidal vortices, Merger of co-rotating vortices, Counter-rotating vortex pair, Model-validation by CASL-computation

Chapter 1
Vortices in Geophysical Flows
- Quasigeostrophic Motions -

1.1 Introduction

Geophysical flows are under strong influence of the buoyancy force associated with stable density stratification and the Coriolis force due to the earth's rotation. The dynamics of such rotating stratified flows is characterized by inertial gravity waves superimposed on nearly geostrophic vortex motions. Since the time scales of vortex motions and waves are widely separated, it is helpful to consider a 'slow manifold of vortex motion' by smearing out 'fast inertial gravity waves'. In fact, isolated vortices with length scales comparable with the meso-scale can persist for a relatively long time. These nearly geostrophic fluid motions are known to be described by the quasi-geostrophic equation. Due to the effects of Coriolis force and stable stratification, vertical motions are suppressed. The fluid motion is confined within a horizontal plane, whereas different motions are allowed on different horizontal planes. We can introduce a stream function (the fluid mechanical sign-convention), which depends on the vertical coordinate z:

$$u = \frac{\partial \psi}{\partial y}, v = -\frac{\partial \psi}{\partial x}. \tag{1.1}$$

The quasi-geostrophic equations of motion (conservation of potential vorticity; e.g. Pedlosky (1979)) in a uniformly stratified rotating (an 'f-plane') fluid, are written as

$$\frac{\partial \Delta \psi}{\partial t} + \left(\frac{\partial \psi}{\partial y}\frac{\partial}{\partial x} - \frac{\partial \psi}{\partial x}\frac{\partial}{\partial y} \right) \Delta \psi = 0. \tag{1.2}$$

Here Δ denotes the three-dimensional Laplacian operator and the potential vorticity q is related to the stream function ψ as

$$q = -\Delta \psi. \tag{1.3}$$

Numerical simulations of decaying quasi-geostrophic turbulence by McWilliams (1989) and McWilliams *et al.* (1994) indicate that the vorticity field develops coherent vortex structures and that their interactions dominate the dynamics of the turbulence. It is tempting to develop a vortex-based turbulence model based on these observations.

There have been many theoretical works on two-dimensional elliptical vortices of uniform vorticity, beginning with Kirchhoff's elliptic vortex, moving on to steady solutions in a strain field by Moore and Saffman (1971) and then to Kida's general solutions (Kida, 1981). Meacham (1992) extended these two-dimensional vortices to three-dimensional ellipsoidal vortices of uniform potential vorticity using the quasi-geostrophic approximation, under which the fluid is uniformly stratified. Miyazaki *et al.* (1999) obtained exact solutions that represent tilted spheroids rotating steadily about the vertical axis, and investigated their stability against infinitesimal perturbations. Meacham *et al.* (1994) extended Kida's analysis to three-dimensional quasi-geostrophic cases and obtained exact unsteady solutions representing a uniform ellipsoidal vortex patch embedded in a uniform horizontal strain e and vertical shear τ with uniform background vorticity ω. Hashimoto *et al.* (1999) investigated the intrinsic stability of stationary ellipsoids in a uniform horizontal strain field. Meacham *et al.* (1997) gave a clear theoretical interpretation of their previous solutions from the viewpoint of Hamiltonian moment reduction. The dynamics of an ellipsoidal vortex in uniform shear is shown to be a Hamiltonian system of two degrees of freedom.

Miyazaki *et al.* (2000) developed a simple turbulence-vortex-model based on these findings, in which each vortex was represented by a slender spheroid; i.e., a wire-vortex model. The dynamical equations were derived systematically using the procedure of Hamiltonian moment reduction. The system of N interacting wire-vortices had $2N$ degree of freedom. Recently, Miyazaki *et al.* (2001) developed an ellipsoidal vortex model, by extending the previous wire model. Each coherent vortex is modeled by an ellipsoid of uniform potential vorticity embedded in a 'locally uniform shear field' induced by other vortices. The equations of motion were derived following a repeat of the procedure of Hamiltonian moment reduction. The center of vorticity and the angular momentum, in addition to the total energy and Casimirs of the system, such as the vortex height and the vortex volume, are conserved. The degree of freedom of N interacting vortices is $3N$, whereas we have only three Poisson commutable invariants. It is the case that even a two-body system shows chaotic behavior.

The objective of this chapter is to assess the validity of the Hamiltonian ellipsoidal moment model by performing direct numerical simulations based on a CASL-algorithm, in which dissipative effects are taken into account by 'surgery'. The dynamical equations of the ellipsoidal moment model are described in 1.2, briefly. The outline of the Contour Advective Semi-Lagrangian (CASL) algorithm is explained in 1.3. The instability of tilted spheroidal vortices is considered in 1.4, where we investigate nonlinear dissipative behavior, such as, filamentation and break-up of unstable vortices, in some detail. The interactions between two co-rotating vortices are studied in 1.5. It is shown that the ellipsoidal moment model can capture the merger of vortices fairly well. In 1.6, we investigate the behavior of a counter-rotating vortex pair (dipole). It is shown that the ellipsoidal moment model predicts infinite stretching of slender vortices. In contrast, such strong stretching is not observed in CASL-computations. The ellipsoidal model needs to be refined in order to circumvent the false singularity.

1.2 N Interacting Ellipsoidal Vortices -Ellipsoidal Moment Model-

We consider the motion of N interacting ellipsoidal vortices of uniform potential vorticity $q_i : i = 1, 2, \cdots, N$, whose center of vorticity is located at (X_i, Y_i, Z_i). Here, the z-axis denotes the vertical axis. The potential vorticity q_i is uniform inside the i-th ellipsoid, whose principal axes lengths are $\alpha_i, \beta_i, \gamma_i$, respectively. Their orientations are specified by the Euler angles ϕ_i, θ_i, ψ_i.

$$\begin{pmatrix} x_i \\ y_i \\ z_i \end{pmatrix} = \mathbf{M}_i \begin{pmatrix} \xi_i \\ \eta_i \\ \zeta_i \end{pmatrix}, \tag{1.4}$$

$$\mathbf{M}_i = \begin{pmatrix} \cos\phi_i & -\sin\phi_i & 0 \\ \sin\phi_i & \cos\phi_i & 0 \\ 0 & 0 & 1 \end{pmatrix} \begin{pmatrix} \cos\theta_i & 0 & \sin\theta_i \\ 0 & 1 & 0 \\ -\sin\theta_i & 0 & \cos\theta_i \end{pmatrix} \begin{pmatrix} \cos\psi_i & -\sin\psi_i & 0 \\ \sin\psi_i & \cos\psi_i & 0 \\ 0 & 0 & 1 \end{pmatrix}, \tag{1.5}$$

where (ξ_i, η_i, ζ_i) denote the principal axes-coordinates fixed to the i-th ellipsoid with (x_i, y_i, z_i) being the Cartesian coordinates centered at (X_i, Y_i, Z_i). The matrix $\mathbf{M}_i$ is the

SO_3 transformation matrix. The detailed derivation of equations of motion is presented in Miyazaki *et al.* (2001).

The state (location, shape, and orientation) of each ellipsoid is also specified by the values of 10 moments up to the second order:

$$\begin{array}{lll} \tilde{m}^{1+10(i-1)} = 1, & \tilde{m}^{2+10i} = x, & \tilde{m}^{3+10(i-1)} = y, \\ \tilde{m}^{4+10(i-1)} = z, & \tilde{m}^{5+10(i-1)} = x^2, & \tilde{m}^{6+10(i-1)} = y^2, \\ \tilde{m}^{7+10(i-1)} = z^2, & \tilde{m}^{8+10(i-1)} = xy, & \tilde{m}^{9+10(i-1)} = yz, \\ \tilde{m}^{10+10(i-1)} = zx, & & \end{array}$$

and

$$\tilde{a}^{j+10(i-1)} = \int_{D_i} q_i \tilde{m}^{j+10(i-1)} \mathrm{d}x\mathrm{d}y\mathrm{d}z. \tag{1.6}$$

Here,

$$\hat{\Gamma}_i = \frac{4\pi}{3} V_i q_i = \tilde{a}^{1+10(i-1)} \tag{1.7}$$

denotes the total vorticity of the $i-$th ellipsoid. The meaning of other variables becomes clearer if we shift the coordinate-origin to the center of each ellipsoid (X_i, Y_i, Z_i):

$$X_i = a^{2+10(i-1)}/\tilde{a}^{1+10(i-1)} = \tilde{a}^{2+10(i-1)}/\tilde{a}^{1+10(i-1)}, \tag{1.8}$$
$$Y_i = a^{3+10(i-1)}/\tilde{a}^{1+10(i-1)} = \tilde{a}^{3+10(i-1)}/\tilde{a}^{1+10(i-1)}, \tag{1.9}$$
$$Z_i = a^{4+10(i-1)}/\tilde{a}^{1+10(i-1)} = \tilde{a}^{4+10(i-1)}/\tilde{a}^{1+10(i-1)}, \tag{1.10}$$

and

$$a^{5+10(i-1)} = \tilde{a}^{5+10(i-1)} - X_i^2 \tilde{a}^{1+10(i-1)}, \tag{1.11}$$
$$a^{6+10(i-1)} = \tilde{a}^{6+10(i-1)} - Y_i^2 \tilde{a}^{1+10(i-1)}, \tag{1.12}$$
$$a^{7+10(i-1)} = \tilde{a}^{7+10(i-1)} - Z_i^2 \tilde{a}^{1+10(i-1)}, \tag{1.13}$$
$$a^{8+10(i-1)} = \tilde{a}^{8+10(i-1)} - X_i Y_i \tilde{a}^{1+10(i-1)}, \tag{1.14}$$
$$a^{9+10(i-1)} = \tilde{a}^{9+10(i-1)} - Y_i Z_i \tilde{a}^{1+10(i-1)}, \tag{1.15}$$
$$a^{10i} = \tilde{a}^{10i} - Z_i X_i \tilde{a}^{1+10(i-1)}. \tag{1.16}$$

These denote the second order moments of the $i-$th ellipsoid,

$$a^{5+10(i-1)} = a^{1+10(i-1)} \overline{x_i^2}, \tag{1.17}$$
$$a^{6+10(i-1)} = a^{1+10(i-1)} \overline{y_i^2}, \tag{1.18}$$
$$a^{7+10(i-1)} = a^{1+10(i-1)} \overline{z_i^2}, \tag{1.19}$$
$$a^{8+10(i-1)} = a^{1+10(i-1)} \overline{x_i y_i}, \tag{1.20}$$
$$a^{9+10(i-1)} = a^{1+10(i-1)} \overline{y_i z_i}, \tag{1.21}$$
$$a^{10i} = a^{1+10(i-1)} \overline{z_i x_i}, \tag{1.22}$$

which are related to the shape and orientation of the ellipsoid as

$$\overline{x_i^2} = \frac{1}{5}\{\alpha_i^2(\cos\phi_i \cos\theta_i \cos\psi_i - \sin\phi_i \sin\psi_i)^2$$

$$+\beta_i^2(\cos\phi_i\cos\theta_i\sin\psi_i+\sin\phi_i\cos\psi_i)^2+\gamma_i^2\cos^2\phi_i\sin^2\theta_i\}, \tag{1.23}$$

$$\overline{y_i^2} = \frac{1}{5}\{\alpha_i^2(\sin\phi_i\cos\theta_i\cos\psi_i+\cos\phi_i\sin\psi_i)^2$$
$$+\beta_i^2(\sin\phi_i\cos\theta_i\sin\psi_i-\cos\phi_i\cos\psi_i)^2+\gamma_i^2\sin^2\phi_i\sin^2\theta_i\}, \tag{1.24}$$

$$\overline{z_i^2} = \frac{1}{5}\{\alpha_i^2\sin^2\theta_i\cos^2\psi_i+\beta_i^2\sin^2\theta_i\sin^2\psi_i+\gamma_i^2\cos^2\theta_i\}, \tag{1.25}$$

$$\overline{x_iy_i} = \frac{1}{5}\{\alpha_i^2(\cos\phi_i\cos\theta_i\cos\psi_i-\sin\phi_i\sin\psi_i)(\sin\phi_i\cos\theta_i\cos\psi_i+\cos\phi_i\sin\psi_i)$$
$$+\beta_i^2(\cos\phi_i\cos\theta_i\sin\psi_i+\sin\phi_i\cos\psi_i)(\sin\phi_i\cos\theta_i\sin\psi_i-\cos\phi_i\cos\psi_i)$$
$$+\gamma_i^2\cos\phi_i\sin\phi_i\sin^2\theta_i\}, \tag{1.26}$$

$$\overline{y_iz_i} = \frac{1}{5}\{\alpha_i^2(\sin\phi_i\cos\theta_i\cos\psi_i+\cos\phi_i\sin\psi_i)(-\sin\theta_i\cos\psi_i)$$
$$+\beta_i^2(-\sin\phi_i\cos\theta_i\sin\psi_i+\cos\phi_i\cos\psi_i)\sin\theta_i\sin\psi_i$$
$$+\gamma_i^2\sin\phi_i\cos\theta_i\sin\theta_i\}, \tag{1.27}$$

$$\overline{z_ix_i} = \frac{1}{5}\{\alpha_i^2(\cos\phi_i\cos\theta_i\cos\psi_i-\sin\phi_i\sin\psi_i)(-\sin\theta_i\cos\psi_i)$$
$$+\beta_i^2(-\cos\phi_i\cos\theta_i\sin\psi_i-\sin\phi_i\cos\psi_i)\sin\theta_i\sin\psi_i$$
$$+\gamma_i^2\cos\phi_i\cos\theta_i\sin\theta_i\}. \tag{1.28}$$

The equations of motion are expressed, using a Poisson bracket, as

$$\frac{\mathrm{d}\tilde{a}^i}{\mathrm{d}t}=\{\tilde{a}^i,H\}=\sum_j^{10N}\tilde{J}^{ij}\frac{\partial H}{\partial\tilde{a}^j}, \tag{1.29}$$

where $\tilde{J}$ is the cosymplectic matrix of the Lie-Poisson form

$$\tilde{J}=\begin{bmatrix}\tilde{J}_1 & 0 & \cdots & 0\\ 0 & \tilde{J}_2 & 0 & 0\\ 0 & 0 & \ddots & 0\\ 0 & 0 & 0 & \tilde{J}_N\end{bmatrix}, \tag{1.30}$$

and

$$\tilde{J}_i=\begin{bmatrix}
0 & 0 & 0 & 0 & 0 & 0 & 0 & 0 & 0 & 0\\
0 & 0 & \tilde{a}^{1+10(i-1)} & 0 & 0 & 2\tilde{a}^{3+10(i-1)} & 0 & \tilde{a}^{2+10(i-1)} & \tilde{a}^{4+10(i-1)} & 0\\
0 & -\tilde{a}^{1-10(i-1)} & 0 & 0 & -2\tilde{a}^{2+10(i-1)} & 0 & 0 & -\tilde{a}^{3+10(i-1)} & 0 & -\tilde{a}^{4+10(i-1)}\\
0 & 0 & 0 & 0 & 0 & 0 & 0 & 0 & 0 & 0\\
0 & 0 & 2\tilde{a}^{2+10(i-1)} & 0 & 0 & 4\tilde{a}^{8+10(i-1)} & 0 & 2\tilde{a}^{5+10(i-1)} & 2\tilde{a}^{10i} & 0\\
0 & -2\tilde{a}^{3+10(i-1)} & 0 & 0 & -4\tilde{a}^{8+10(i-1)} & 0 & 0 & -2\tilde{a}^{6+10(i-1)} & 0 & -2\tilde{a}^{9+10(i-1)}\\
0 & 0 & 0 & 0 & 0 & 0 & 0 & 0 & 0 & 0\\
0 & -\tilde{a}^{2-10(i-1)} & \tilde{a}^{3+10(i-1)} & 0 & -2\tilde{a}^{5+10(i-1)} & 2\tilde{a}^{6+10(i-1)} & 0 & 0 & \tilde{a}^{9+10(i-1)} & -\tilde{a}^{10i}\\
0 & -\tilde{a}^{4-10(i-1)} & 0 & 0 & -2\tilde{a}^{10i} & 0 & 0 & -\tilde{a}^{9+10(i-1)} & 0 & -\tilde{a}^{7+10(i-1)}\\
0 & 0 & \tilde{a}^{4+10(i-1)} & 0 & 0 & 2\tilde{a}^{9+10(i-1)} & 0 & \tilde{a}^{10i} & \tilde{a}^{7+10(i-1)} & 0
\end{bmatrix}. \tag{1.31}$$

Without specifying the actual form of the Hamiltonian, we notice that $\tilde{a}^{1+10(i-1)}$, $\tilde{a}^{4+10(i-1)}$, and $\tilde{a}^{7+10(i-1)}$ are Casimirs. Physically, $\tilde{a}^{1+10(i-1)}=a^{1+10(i-1)}$ is the total vorticity (or the volume) of the i-th ellipsoidal vortex, and $Z_i=\tilde{a}^{4+10(i-1)}/\tilde{a}^{1+10(i-1)}$ denotes the z-coordinate of the center of the i-th ellipsoid. The conserved quantity $\tilde{a}^{7+10(i-1)}$ is linked with the vortex-height zh_i of the i-th ellipsoid.

Expressing all variables $\tilde{a}^i$ by a^i, and using the chain rule for differentiations, we obtain the equations of motion:

$$\frac{\mathrm{d}a^2}{\mathrm{d}t} = a^1\frac{\partial H}{\partial a^3}, \tag{1.32}$$

$$\frac{\mathrm{d}a^3}{\mathrm{d}t} = -a^1\frac{\partial H}{\partial a^2}, \tag{1.33}$$

$$\frac{\mathrm{d}a^5}{\mathrm{d}t} = 4a^8\frac{\partial H}{\partial a^6} + 2a^5\frac{\partial H}{\partial a^8} + 2a^{10}\frac{\partial H}{\partial a^9}, \tag{1.34}$$

$$\frac{\mathrm{d}a^6}{\mathrm{d}t} = -4a^8\frac{\partial H}{\partial a^5} - 2a^6\frac{\partial H}{\partial a^8} - 2a^9\frac{\partial H}{\partial a^{10}}, \tag{1.35}$$

$$\frac{\mathrm{d}a^8}{\mathrm{d}t} = -2a^5\frac{\partial H}{\partial a^5} + 2a^6\frac{\partial H}{\partial a^6} + a^9\frac{\partial H}{\partial a^9} - a^{10}\frac{\partial H}{\partial a^{10}}, \tag{1.36}$$

$$\frac{\mathrm{d}a^9}{\mathrm{d}t} = -2a^{10}\frac{\partial H}{\partial a^5} - a^9\frac{\partial H}{\partial a^8} - a^7\frac{\partial H}{\partial a^{10}}, \tag{1.37}$$

$$\frac{\mathrm{d}a^{10}}{\mathrm{d}t} = 2a^9\frac{\partial H}{\partial a^6} + a^{10}\frac{\partial H}{\partial a^8} + a^7\frac{\partial H}{\partial a^9}. \tag{1.38}$$

Similar equations hold for the $i-$th vortex, where all superscripts are added by $10(i-1)$.

The final task is to write down the Hamiltonian of the system, using these moments up to the second order:

$$H = \sum_{i=1}^{N} H_{si} + \sum_{(i,j)} H_{mij}. \tag{1.39}$$

The first term denotes the summation of the self-energy of each vortex and the second term, which is the summation over $N(N-1)/2$ pairs of vortices, represents the mutual interaction energy. As for the self-energy H_{si} of the $i-$th ellipsoid, we can use the classical result (Chandrasekhar, 1987):

$$H_{si} = \frac{2\pi}{15}V_i^2 q_i^2 \int_0^\infty \frac{\mathrm{d}s}{\sqrt{(s+\alpha_i^2)(s+\beta_i^2)(s+\gamma_i^2)}}. \tag{1.40}$$

We must introduce an approximation in order to express the Hamiltonian H_{mij} corresponding the mutual interaction, by using only the moments up to second order:

$$\begin{aligned}
H_{mij} &= \frac{1}{2}\{\int_{D_i}\psi_j q_i \mathrm{d}x\mathrm{d}y\mathrm{d}z + \int_{D_j}\psi_i q_j \mathrm{d}x\mathrm{d}y\mathrm{d}z\} \\
&= \frac{1}{4\pi}[\frac{1}{R_{ij}}a^{1+10(i-1)}a^{1+10(j-1)} \\
&\quad -\frac{1}{2R_{ij}^3}(a^{5+10(i-1)}a^{1+10(j-1)} + a^{1+10(i-1)}a^{5+10(j-1)} + a^{6+10(i-1)}a^{1+10(j-1)} \\
&\quad +a^{1+10(i-1)}a^{6+10(j-1)} + a^{7+10(i-1)}a^{1+10(j-1)} + a^{1+10(i-1)}a^{7+10(j-1)}) \\
&\quad +\frac{3}{2R_{ij}^5}\{(\frac{a^{2+10(i-1)}}{a^{1+10(i-1)}} - \frac{a^{2+10(j-1)}}{a^{1+10(j-1)}})^2(a^{5+10(i-1)}a^{1+10(j-1)} + a^{1+10(i-1)}a^{5+10(j-1)}) \\
&\quad +(\frac{a^{3+10(i-1)}}{a^{1+10(i-1)}} - \frac{a^{3+10(j-1)}}{a^{1+10(j-1)}})^2(a^{6+10(i-1)}a^{1+10(j-1)} + a^{1+10(i-1)}a^{6+10(j-1)})
\end{aligned}$$

$$
\begin{aligned}
&+\left(\frac{a^{4+10(i-1)}}{a^{1+10(i-1)}}-\frac{a^{4+10(j-1)}}{a^{1+10(j-1)}}\right)^2\left(a^{7+10(i-1)}a^{1+10(j-1)}+a^{1+10(i-1)}a^{7+10(j-1)}\right)\\
&+2\left(\frac{a^{2+10(i-1)}}{a^{1+10(i-1)}}-\frac{a^{2+10(j-1)}}{a^{1+10(j-1)}}\right)\left(\frac{a^{3+10(i-1)}}{a^{1+10(i-1)}}-\frac{a^{3+10(j-1)}}{a^{1+10(j-1)}}\right)\\
&\quad\times\left(a^{8+10(i-1)}a^{1+10(j-1)}+a^{1+10(i-1)}a^{8+10(j-1)}\right)\\
&+2\left(\frac{a^{3+10(i-1)}}{a^{1+10(i-1)}}-\frac{a^{3+10(j-1)}}{a^{1+10(j-1)}}\right)\\
&\quad\times\left(\frac{a^{4+10(i-1)}}{a^{1+10(i-1)}}-\frac{a^{4+10(j-1)}}{a^{1+10(j-1)}}\right)\left(a^{9+10(i-1)}a^{1+10(j-1)}+a^{1+10(i-1)}a^{9+10(j-1)}\right)\\
&+2\left(\frac{a^{4+10(i-1)}}{a^{1+10(i-1)}}-\frac{a^{4+10(j-1)}}{a^{1+10(j-1)}}\right)\left(\frac{a^{2+10(i-1)}}{a^{1+10(i-1)}}-\frac{a^{2+10(j-1)}}{a^{1+10(j-1)}}\right)\left(a^{10i}a^{1+10(j-1)}+a^{1+10(i-1)}a^{10j}\right)\}|\\
&+H.O.T.,
\end{aligned}
\tag{1.41}
$$

where

$$
\begin{aligned}
R_{ij} &= \sqrt{\left(\frac{a^{2+10(i-1)}}{a^{1+10(i-1)}}-\frac{a^{2+10(j-1)}}{a^{1+10(j-1)}}\right)^2+\left(\frac{a^{3+10(i-1)}}{a^{1+10(i-1)}}-\frac{a^{3+10(j-1)}}{a^{1+10(j-1)}}\right)^2+\left(\frac{a^{4+10(i-1)}}{a^{1+10(i-1)}}-\frac{a^{4+10(j-1)}}{a^{1+10(j-1)}}\right)^2}\\
&= \sqrt{(X_i-X_j)^2+(Y_i-Y_j)^2+(Z_i-Z_j)^2}.
\end{aligned}
\tag{1.42}
$$

The motion of the center of the $i-$th ellipsoidal vortex is computed from (1.32) and (1.33), as

$$
\begin{aligned}
\dot{X}_i &= \sum_{j\neq i}\Bigg(-\frac{V_j}{3R_{ij}^3}[(Y_i-Y_j)\\
&\quad-\frac{3}{R_{ij}^2}\{(\overline{x_iy_i}+\overline{x_jy_j})(X_i-X_j)+(\overline{y_i^2}+\overline{y_j^2})(Y_i-Y_j)+(\overline{y_iz_i}+\overline{y_jz_j})(Z_i-Z_j)\}\\
&\quad-\frac{3}{2R_{ij}^2}(Y_i-Y_j)(\overline{x_i^2}+\overline{x_j^2}+\overline{y_i^2}+\overline{y_j^2}+\overline{z_i^2}+\overline{z_j^2})\\
&\quad+\frac{15}{2R_{ij}^4}(Y_i-Y_j)\{\\
&\quad+2(\overline{x_iy_i}+\overline{x_jy_j})(X_i-X_j)(Y_i-Y_j)+(\overline{x_i^2}+\overline{x_j^2})(X_i-X_j)^2\\
&\quad+2(\overline{y_iz_i}+\overline{y_jz_j})(Y_i-Y_j)(Z_i-Z_j)+(\overline{y_i^2}+\overline{y_j^2})(Y_i-Y_j)^2\\
&\quad+2(\overline{z_ix_i}+\overline{z_jx_j})(Z_i-Z_j)(X_i-X_j)+(\overline{z_i^2}+\overline{z_j^2})(Z_i-Z_j)^2\}]\Bigg),
\end{aligned}
\tag{1.43}
$$

$$
\begin{aligned}
\dot{Y}_i &= \sum_{j\neq i}\Bigg(\frac{V_j}{3R_{ij}^3}[(X_i-X_j)\\
&\quad-\frac{3}{R_{ij}^2}((\overline{x_i^2}+\overline{x_j^2})(X_i-X_j)+(\overline{x_iy_i}+\overline{x_jy_j})(Y_i-Y_j)+(\overline{z_ix_i}+\overline{z_jx_j})(Z_i-Z_j))\\
&\quad-\frac{3}{2R_{ij}^2}(X_i-X_j)(\overline{x_i^2}+\overline{x_j^2}+\overline{y_i^2}+\overline{y_j^2}+\overline{z_i^2}+\overline{z_j^2})\\
&\quad+\frac{15}{2R_{ij}^4}(X_i-X_j)\{\\
&(\overline{x_i^2}+\overline{x_j^2})(X_i-X_j)^2+2(\overline{x_iy_i}+\overline{x_jy_j})(X_i-X_j)(Y_i-Y_j)\\
&+(\overline{y_i^2}+\overline{y_j^2})(Y_i-Y_j)^2+2(\overline{y_iz_i}+\overline{y_jz_j})(Y_i-Y_j)(Z_i-Z_j)
\end{aligned}
$$

$$+(\overline{z_i^2}+\overline{z_j^2})(Z_i-Z_j)^2+2(\overline{z_ix_i}+\overline{z_jx_j})(Z_i-Z_j)(X_i-X_j)\}]\Big). \tag{1.44}$$

The first terms on the right hand sides denote the induced velocity by the 'virtual point vortices $\hat{\Gamma}_j$' located at (X_j, Y_j, Z_j). The correction terms proportional to the quadratic moments with the subscript i are due to the vorticity-weighted average inside the $i-$th ellipsoid of the velocity field induced by the 'virtual point vortex $\hat{\Gamma}_j$', and those proportional to the quadratic moments with the subscript j represent the corrections due to vorticity distribution inside the $j-$th ellipsoid (non point vortex effect).

The remaining equations (1.34)-(1.38) determine the time-evolution of the shape, and the orientation of the i-th ellipsoid. Since the volume of the ellipsoid is invariant, $\alpha_i, \beta_i, \gamma_i$ are not independent and we can introduce the following new variables a_i, b_i:

$$a_i = \frac{\alpha_i}{\gamma_i}, \tag{1.45}$$

$$b_i = \frac{\beta_i}{\gamma_i}. \tag{1.46}$$

After straightforward (but lengthy) algebraic manipulations, we can rewrite the equations of motion using the primitive variables a_i, b_i and ϕ_i, θ_i, ψ_i (see also Meacham *et al.* (1997)). The shape of the ellipsoid changes as

$$\begin{aligned}\frac{\dot{a}_i}{a_i} = &\sum_{j\neq i}\{\frac{1}{2}e_{ij}\{\cos\theta_i\sin 2\psi_i\cos 2(\phi_i-\epsilon_{ij})\\ &+[\cos 2\psi_i-\sin^2\theta_i(1+\cos^2\psi_i)]\sin 2(\phi_i-\epsilon_{ij})\}\\ &+\tau_{ij}\sin\theta_i[\frac{1}{2}\sin 2\psi_i\sin(\phi_i-\chi_{ij})-\cos\theta_i(1+\cos^2\psi_i)\cos(\phi_i-\chi_{ij})]\},\end{aligned} \tag{1.47}$$

$$\begin{aligned}\frac{\dot{b}_i}{b_i} = &\sum_{j\neq i}\{-\frac{1}{2}e_{ij}\{\cos\theta_i\sin 2\psi_i\cos 2(\phi_i-\epsilon_{ij})\\ &+[\cos 2\psi_i+\sin^2\theta_i(1+\sin^2\psi_i)]\sin 2(\phi_i-\epsilon_{ij})\}\\ &-\tau_{ij}\sin\theta_i[\frac{1}{2}\sin 2\psi_i\sin(\phi_i-\chi_{ij})+\cos\theta_i(1+\sin^2\psi_i)\cos(\phi_i-\chi_{ij})]\}.\end{aligned} \tag{1.48}$$

If it were not for the horizontal strain and the vertical shear induced by other vortices, each ellipsoid would rotate rigidly. The orientation of the principal axes ϕ_i, θ_i, ψ_i changes as

$$\begin{aligned}\dot{\phi}_i = &\frac{1}{2}(\Omega_i^{(1)}+\Omega_i^{(2)})+\frac{1}{2}(\Omega_i^{(1)}-\Omega_i^{(2)})\cos 2\psi_i\\ &+\sum_{j\neq i}\{\frac{1}{2}\omega_{ij}-\frac{1}{2}e_{ij}[\left(\frac{a_i^2+1}{a_i^2-1}\sin^2\psi_i+\frac{b_i^2+1}{b_i^2-1}\cos^2\psi_i\right)\cos 2(\phi_i-\epsilon_{ij})\\ &+(\frac{1}{a_i^2-1}-\frac{1}{b_i^2-1})\cos\theta_i\sin 2\psi_i\sin 2(\phi_i-\epsilon_{ij})]\\ &+\frac{\tau_{ij}}{\sin\theta_i}[\cos\theta_i(\frac{\sin^2\psi_i}{a_i^2-1}+\frac{\cos^2\psi_i}{b_i^2-1})\sin(\phi_i-\chi_{ij})\\ &-\frac{1}{2}(\frac{1}{a_i^2-1}-\frac{1}{b_i^2-1})\cos 2\theta_i\sin 2\psi_i\cos(\phi_i-\chi_{ij})]\},\end{aligned} \tag{1.49}$$

$$\dot{\theta}_i = \frac{1}{2}\sin\theta_i\sin 2\psi_i(\Omega_i^{(2)}-\Omega_i^{(1)})$$

$$+\sum_{j\neq i}\{-\frac{1}{2}e_{ij}\sin\theta_i[(\frac{a_i^2+1}{a_i^2-1}\cos^2\psi_i+\frac{b_i^2+1}{b_i^2-1}\sin^2\psi_i)\cos\theta_i\sin 2(\phi_i-\epsilon_{ij})$$
$$+(\frac{1}{a_i^2-1}-\frac{1}{b_i^2-1})\sin 2\psi_i\cos 2(\phi_i-\epsilon_{ij})]$$
$$+\tau_{ij}\{[\sin^2\theta_i-\cos 2\theta_i\left(\frac{\cos^2\psi_i}{a_i^2-1}+\frac{\sin^2\psi_i}{b_i^2-1}\right)]\cos(\phi_i-\chi_{ij})$$
$$+\frac{1}{2}(\frac{1}{a_i^2-1}-\frac{1}{b_i^2-1})\cos\theta_i\sin 2\psi_i\sin(\phi_i-\chi_{ij})\}\}, \tag{1.50}$$

$$\dot{\psi}_i = \cos\theta_i[\Omega_i^{(3)}-\frac{1}{2}(\Omega_i^{(1)}+\Omega_i^{(2)})-\frac{1}{2}(\Omega_i^{(1)}-\Omega_i^{(2)})\cos 2\psi_i]$$
$$+\sum_{j\neq i}\left[\frac{1}{2}e_{ij}\{\cos\theta_i(\frac{a_i^2+1}{a_i^2-1}\sin^2\psi_i+\frac{b_i^2+1}{b_i^2-1}\cos^2\psi_i+(\frac{a_i^2+b_i^2}{a_i^2-b_i^2})\cos 2\psi_i)\cos 2(\phi_i-\epsilon_{ij})\right.$$
$$+[(\frac{1}{a_i^2-1}-\frac{1}{b_i^2-1})\cos^2\theta_i-\frac{1}{2}(\frac{a_i^2+b_i^2}{a_i^2-b_i^2})(1+\cos^2\theta_i)]\sin 2\psi_i\sin 2(\phi_i-\epsilon_{ij})\}$$
$$-\frac{\tau_{ij}}{\sin\theta_i}\{[\cos^2\theta_i(\frac{\sin^2\psi_i}{a_i^2-1}+\frac{\cos^2\psi_i}{b_i^2-1})-\sin^2\theta_i(\frac{a_i^2\cos^2\psi_i-b_i^2\sin^2\psi_i}{a_i^2-b_i^2})]\sin(\phi_i-\chi_{ij})$$
$$\left.-\frac{1}{2}[(\frac{1}{a_i^2-1}-\frac{1}{b_i^2-1})\cos\theta_i\cos 2\theta_i+\frac{1}{2}(\frac{a_i^2+b_i^2}{a_i^2-b_i^2})\sin\theta_i\sin 2\theta_i]\sin 2\psi_i\cos(\phi_i-\chi_{ij})\}\right]. \tag{1.51}$$

Here,

$$\omega_{ij} = \frac{V_j q_j(3\cos^2\Theta_{ij}-1)}{3R_{ij}^3}, \tag{1.52}$$
$$e_{ij} = -\frac{V_j q_j\sin^2\Theta_{ij}}{R_{ij}^3}, \tag{1.53}$$
$$\epsilon_{ij} = \Phi_{ij}, \tag{1.54}$$
$$\tau_{ij} = \frac{V_j q_j\cos\Theta_{ij}\sin\Theta_{ij}}{R_{ij}^3}, \tag{1.55}$$
$$\chi_{ij} = \Phi_{ij}-\frac{\pi}{2} \tag{1.56}$$

with

$$\Theta_{ij} = \cos^{-1}\{\frac{Z_i-Z_j}{R_{ij}}\}, \tag{1.57}$$
$$\Phi_{ij} = \tan^{-1}\{\frac{Y_i-Y_j}{X_i-X_j}\} \tag{1.58}$$

denote the background vorticity ω_{ij}, the strain field e_{ij} and the vertical shear τ_{ij} induced at the center of the $i-$th ellipsoidal vortex by the '$j-$th virtual point vortex', respectively. The variables $\Omega_i^{(j)}$ are the self-rotation rates:

$$I_i^{(1)} \equiv \int_0^\infty \frac{1}{2}\frac{a_i b_i s^1 ds}{[(s+a_i^2)(s+b_i^2)(s+1)]^{3/2}}, \tag{1.59}$$
$$I_i^{(2)} \equiv \int_0^\infty \frac{1}{2}\frac{a_i b_i s^2 ds}{[(s+a_i^2)(s+b_i^2)(s+1)]^{3/2}}, \tag{1.60}$$

$$\Omega_i^{(1)} = q_i(a_i^2 I_i^{(1)} + I_i^{(2)}), \tag{1.61}$$

$$\Omega_i^{(2)} = q_i(b_i^2 I_i^{(1)} + I_i^{(2)}), \tag{1.62}$$

$$\Omega_i^{(3)} = q_i(I_i^{(1)} + I_i^{(2)}). \tag{1.63}$$

These complete the derivation of the equations of motion of N interacting ellipsoidal vortices. Although these equations are very lengthy, they are actually the same as those of Meacham *et al.* (1997), who considered the motion of an ellipsoidal vortex embedded in a uniform horizontal strain, background vorticity, and vertical shear field. What we have done here is to sum up the background vorticity ω_{ij}, the strain field e_{ij}, and the vertical shear τ_{ij} induced at the center of the $i-$th ellipsoidal vortex by the '$j-$th virtual point vortex', based on the fact that the terms representing these effects are linear.

The above Hamiltonian dynamical system has several invariants. As noted already, three invariants are Casimirs; i.e., the total vorticity (vortex volume) of the ith ellipsoid $\hat{\Gamma}_i$, the $z-$coordinate of the center of the ith ellipsoid Z_i, and the vortex-height of the ith ellipsoid

$$zh_i = \sqrt{\gamma_i^2 \cos^2\theta_i + \sin^2\theta_i(\alpha_i^2 \cos^2\psi_i + \beta_i^2 \sin^2\psi_i)}. \tag{1.64}$$

Then the degree of freedom of each ellipsoid is reduced to three (six independent variables). Other conserved quantities are the total energy H, the vorticity center of the whole system

$$P = \sum_i \int_{D_i} q_i x \mathrm{d}\tau = \sum_i \hat{\Gamma}_i X_i, \tag{1.65}$$

$$Q = \sum_i \int_{D_i} q_i y \mathrm{d}\tau = \sum_i \hat{\Gamma}_i Y_i \tag{1.66}$$

and the angular momentum

$$\begin{aligned} L &= \sum_i \int_{D_i} q_i(x^2 + y^2)\mathrm{d}\tau \\ &= \sum_i \hat{\Gamma}_i(X_i^2 + Y_i^2 + \overline{x_i^2} + \overline{y_i^2}). \end{aligned} \tag{1.67}$$

As in the case of the two-dimensional point vortices, we notice that $H, P^2 + Q^2, L$ are Poisson-commutable invariants. Even a two-ellipsoids system has 'six degrees of freedom', which exceeds the number of the Poisson-commutable invariants (three). According to the Liouville-Arnol'd theorem, this dynamical system is not integrable. Miyazaki *et al.* (2001) investigated the interaction of two co-rotating spheroidal vortices of the same shape, by adjusting the initial distance between the vortices. When two vortices were placed close enough initially, the motion became chaotic, the horizontal distance $D(t) = \sqrt{(X_2 - X_1)^2 + (Y_2 - Y_1)^2}$ between two vortices oscillated irregularly with a large amplitude, and a 'merger' of vortices occurred. By defining the 'merger' to be a phenomenon in which the following two conditions were satisfied (i.e., the vertical overlap ($|Z_2 - Z_1| < zh_1 + zh_2$) and the horizontal overlap ($D(t) < V_1^{1/3} + V_2^{1/3}$) with $V_1^{1/3} + V_2^{1/3}$ denoting the 'average-radius'), they determined the threshold of the initial distance leading to the merger. It was found that the threshold of the merger was almost the same as that of the chaotic motions.

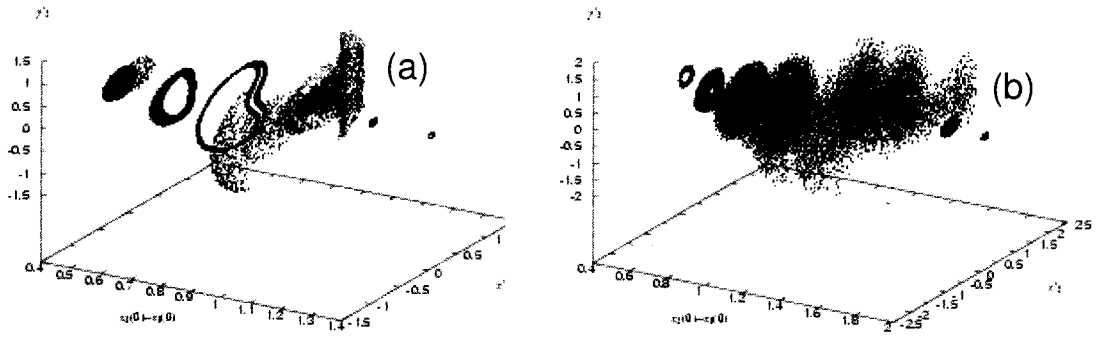

Fig. 1.1: **Poincare sections** for the cases of (a) $V_{1,2} = 0.1$, $zh_{1,2} = 1.0$, $\theta_1(0) = 0$, $\tan\theta_2(0) = 0.1$, $\hat{\Gamma}_{1,2} = 1.0$, (b) $V_{1,2} = 0.5$, $zh_{1,2} = 1.0$, $\theta_1(0) = 0$, $\tan\theta_2(0) = 0.1$, $\hat{\Gamma}_{1,2} = 1.0$.

The range of the initial distance $X_2(0) - X_1(0)$, where chaotic motions (and the merger) are found, becomes larger as the ellipsoid becomes fatter (larger V). Figures 1.1a and b show the Poincare sections for the cases of $V_{1,2} = 0.1, (\alpha_1(0) = \alpha_2(0) = 0.4, \beta_1(0) = 0.25, \beta_2(0) = 0.247, \gamma_1(0) = 1.0, \gamma_2(0) = 1.005)$ and $V_{1,2} = 0.5, (\alpha_1(0) = \alpha_2(0) = 0.8, \beta_1(0) = 0.625, \beta_2(0) = 0.622, \gamma_1(0) = 1.0, \gamma_2(0) = 1.005)$, respectively. We can see that the chaos-region expands as the value of $V = \alpha\beta\gamma$ increases. This is mainly because the precession angular velocity decreases as the ellipsoid becomes fatter. Roughly speaking, chaotic motions are found if the induced vertical shear τ increases more than about 30% of the averaged precession angular velocity $\frac{\Omega^{(1)}+\Omega^{(2)}}{2}$.

We have constructed an ellipsoidal moment model with the intention to simulate the vortex interactions in a quasi-geostrophic turbulence. The dynamics of ellipsoidal vortices is shown to be a Hamiltonian system of finite degrees of freedom, which can be extracted from the partial differential equations governing the dynamics of quasi-geostrophic fluid motion by a systematic 'Hamiltonian moment reduction' procedure. In many body interactions, the center of vorticity and the angular momentum, in addition to the total energy, are conserved. Because the number of Poisson-commutable invariants are three, chaotic motions are observed even in a two-body system. It is found that the distance between two ellipsoids, which move around chaotically, oscillates rapidly with time. If the initial distance is less than a certain critical value, two vortices approach each other suggesting the occurrence of a 'merger'. We attempted to derive a simple rule for the merger (i.e., to determine the critical distance) using the ellipsoidal moment model, and found that such a simple criterion known to hold for two-dimensional vortex interactions does not hold for quasi-geostrophic cases. Further investigations are required to construct a useful rule. If we can do this and, additionally, define the properties of the ellipsoidal vortex created after the merger, we can perform a 'quasi-turbulence simulation'.

These results might, however, be of limited value, given that the truncation error in representing the mutual energy by the moments up to the second order becomes large as the distance between vortices decreases. The shape of vortices will largely deviate from the ellipsoidal form, and they may not be approximated by ellipsoids. It is necessary to check the prediction based on the ellipsoidal moment model very carefully. In the following sections, we assess the validity of the ellipsoidal model by performing direct numerical simulations (Miyazaki *et al.*, 2002).

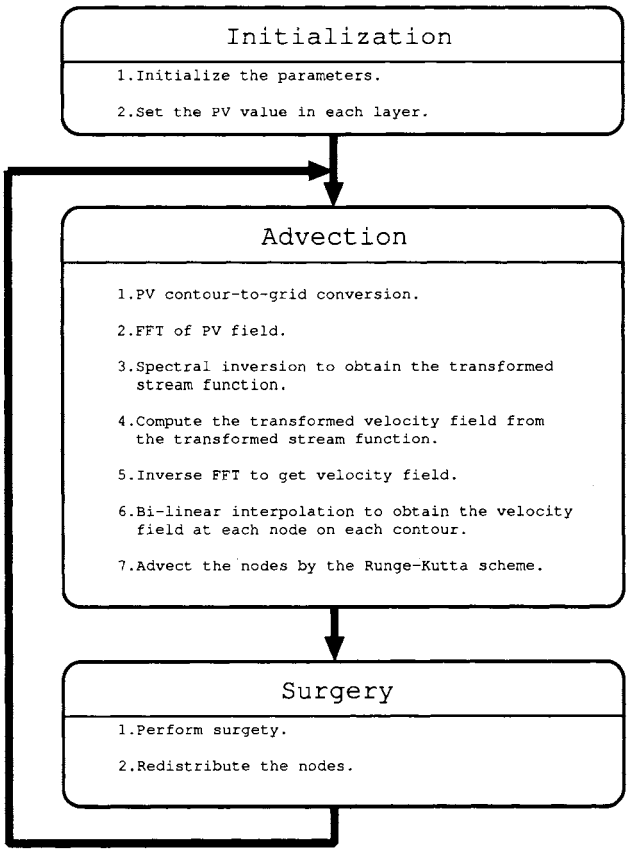

Fig. 1.2: Flow chart of the CASL-algorithm.

1.3 CASL-Algorithm

In order to investigate the effects of the shape deformation from an ellipsoid and the dissipative processes, which are neglected in the ellipsoidal moment model completely, we consider typical nonlinear dissipative events in quasi-geostrophic turbulence; i.e., filamentation and break-up of unstable spheroidal vortices and the merger of co- and counter-rotating vortices. These dynamical events are very important in the understanding of energy and enstrophy cascades of the quasi-geostrophic turbulence.

The following direct numerical simulations are performed using a CASL-algorithm developed by Dritschel and Ambaum (1997). The outline of the CASL-algorithm is illustrated in Fig.1.2. The distribution of the potential vorticity is represented by nested contour-lines corresponding to gaps of the potential vorticity value (Initialization). The value of potential vorticity at a grid point is computed by an efficient contour-to-grid conversion technique. Next, the potential vorticity field is inverted to obtain the stream function and the velocity field (Inversion). This inversion process is performed in the spectral space. Then, each contour is advected by the velocity field induced by the vorticity field (Contour advection by a Runge-Kutta scheme); the velocity at a node on the contour is computed by a linear interpolation, again. Surgery is performed if the distance between two contours containing the same potential vorticity becomes less than the cut-off scale δ (Surgery). This operation introduces an artificial viscosity into the

numerical computation. Although its relation to the physical viscosity is not clear, we expect that dissipative effects are, at least approximately, incorporated by the surgery process. After surgery, nodes on each contour are redistributed in order to represent the contour accurately (Node redistribution). These steps complete a cycle of the CASL-computation.

The CASL-algorithm has several advantages compared with conventional algorithms such as a pseudo-spectral algorithm (McWilliams, 1989 and McWilliams *et al.*, 1994) and a finite-difference algorithm (Hardenberg and McWilliams, 2000). Pseudo-spectral algorithms are more accurate and less time-consuming than finite-difference algorithms, as long as the computed flow field is sufficiently smooth. Pseudo-spectral schemes, however, suffer from the so-called 'Gibbs phenomena' at any jump in potential vorticity. It is impossible to compare the numerical results with the theoretical predictions wherein all vortices are assumed to have a uniform potential vorticity anomaly. Since finite-difference algorithms are, in general, less accurate, it is rather inefficient to capture fine structures such as filaments emitted from the main vortices. In contrast, the CASL-algorithm can capture the fine structures, because it follows the Lagrangian movement of contours. In addition, it uses FFT in the inversion process, which accelerates the computation considerably in comparison with the original Contour Surgery algorithm.

1.4 Tilted Spheroids

In this section, we study the behavior of perturbed spheroidal vortices ($\alpha = \beta$). A prolate spheroid, tilted from the vertical (z) axis by Θ, rotates steadily about the z-axis with the constant angular velocity Ω:

$$\Omega = \frac{q}{4}\cosh\Xi_0 \sinh^2\Xi_0 \left\{ \log\left(\frac{\cosh\Xi_0 - 1}{\cosh\Xi_0 + 1}\right)(3\cosh^2\Xi_0 - 1) - 6\cosh\Xi_0 \right\}. \qquad (1.68)$$

This is a function of the aspect ratio $\alpha/\gamma = \tanh\Xi_0$, and it is independent of the inclination angle Θ from the vertical axis. The linear stability of a tilted prolate spheroid was investigated by Miyazaki *et al.* (1999). We plot the instability ($n = 3$ Legendre mode) growth rate as contour lines in Fig.1.3. Roughly speaking, a prolate spheroid becomes unstable against the third Legendre mode when $\alpha/\gamma < 0.44$ and $\Theta > 0.48$. Two peaks of growth rate, one at 0.0522 and one at 0.0531, of the third mode are attained at $(\alpha/\gamma = 0.250, \Theta = 1.275)$ and $(\alpha/\gamma = 0.254, \Theta = \pi/2)$. Similarly, a prolate spheroidal vortex becomes unstable to the fourth mode ($n = 4$) for $\alpha/\gamma < 0.27$ and $\Theta > 0.55$, and to the fifth mode ($n = 5$) if $\alpha/\gamma < 0.23$ and $\Theta > 0.58$, respectively. The parameter region, where the instability is observed, becomes narrower as the order of Legendre function becomes higher.

Nonlinear development is computed numerically by the CASL-algorithm, where 64^3 grid points are used in most of the computations. The grid points are increased up to 128^3 to check the accuracy. No substantial difference is found between the results using the usual and finer grid points.

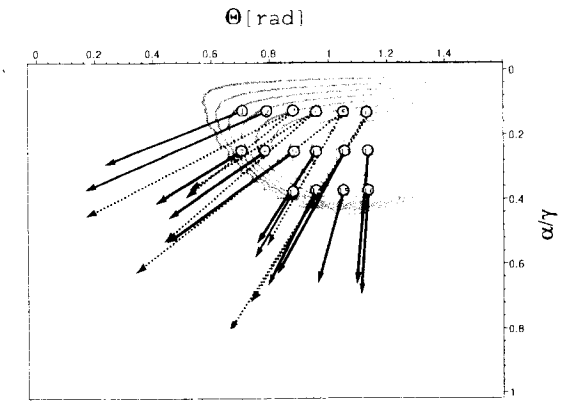

Fig. 1.3: **Instability of a tilted prolate spheroid** ($n = 3$ Legendre mode) and the spheroid (or spheroids) born after the dissipative processes, i.e., filamentation (solid arrow) and splitting (dotted arrow).

Table 1.1: **Instability of an inclined spheroid.**

No.	α/γ	$\Theta(deg)$	$\gamma cos\Theta$	α'/γ'	Θ'	category
1	0.125	40	1.00	0.260	17.6	filamentation
2	0.125	45	1.00	0.317	12.9	filamentation
3	0.125	50	0.75	0.462	12.8	splitting
			0.398	33.3		
4	0.125	55	0.75	0.371	34.5	splitting
			0.526	27.9		
5	0.125	60	0.75	0.535	47.0	splitting
			0.630	20.7		
6	0.125	65	0.75	0.656	46.4	splitting
			0.792	38.5		
7	0.250	40	1.00	0.391	26.6	filamentation
8	0.250	45	1.00	0.436	28.5	filamentation
9	0.250	50	0.75	0.525	28.8	filamentaion
10	0.250	55	0.75	0.518	43.3	filamentation
11	0.250	60	0.75	0.611	45.9	filamentation
12	0.250	65	0.75	0.619	61.3	filamentation
13	0.375	50	0.75	0.537	42.1	filamentation
14	0.375	55	0.75	0.649	46.6	filamentation
15	0.375	60	0.75	0.607	55.4	filamentation
16	0.375	65	0.75	0.628	63.0	filamentation

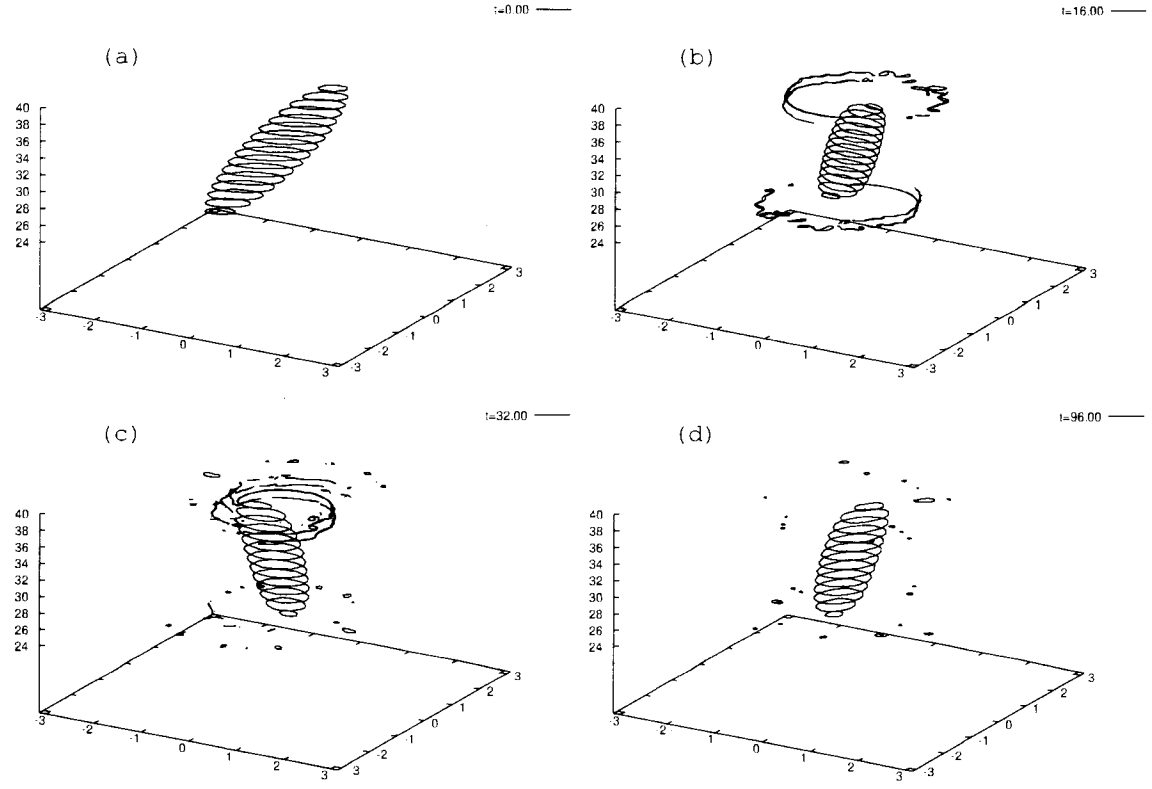

Fig. 1.4: **Weakly unstable spheroid**: Filamentaion, $\alpha/\gamma = 0.25$, $\Theta = 1.05$ (No.11), (a) $t = 0$, (b) $t = 16$, (c) $t = 32$, (d) $t = 96$.

We can classify the behavior into three categories; steady stable rotation, unstable filamentation, and splitting (break-up) into two pieces. If a spheroidal vortex is linearly stable, it rotates rigidly about the vertical axis and the angular velocity observed in the DNS result coincides with the theoretical value within 3%, which confirms the accuracy of the numerical computation. These cases are not shown in Fig.1.3 or in Table 1.1, since they are of little dynamical interest. The circles with a solid arrow in Fig.1.3 show the initially unstable spheroids that nutate (nod up) to become stable, after emitting thin filaments from both top and bottom.

Figure 1.4 illustrates the typical time evolution in this category (No.11). This occurs when the initial spheroid is not so slender or so highly unstable. A solid arrow in Fig.1.3 indicates the 'stable spheroid' created after the filamentation. Although the reset-vortex should be fitted by a general ellipsoid, it is difficult to properly estimate the three principal axes-lengths and the Euler angles from the computational results. In the following, we consider that the vortices created after dissipative events are inclined spheroids that rotate rigidly around the vertical axis. The aspect ratio and the inclination angle of the spheroid are estimated from the height $zh' = \sqrt{\alpha'^2 \sin^2\theta' + \gamma'^2 \cos^2\theta'}$, the semi-minor axis α' and the semi-major axis $\alpha'\gamma'/zh'$ of the elliptical cross section at $z = 0$ (Table 1.1). Note that the precession angular velocity increases as the aspect ratio increases.

If the initial spheroid is slender and strongly unstable (open circles with two dotted arrows in Fig.1.3), it splits into two volumes of uniform potential vorticity, which are identified as two stable spheroids (Table 1.1). Figure 1.5 depicts the typical time evolution of this category (No.4). The splitting occurs at a relatively early stage of the time

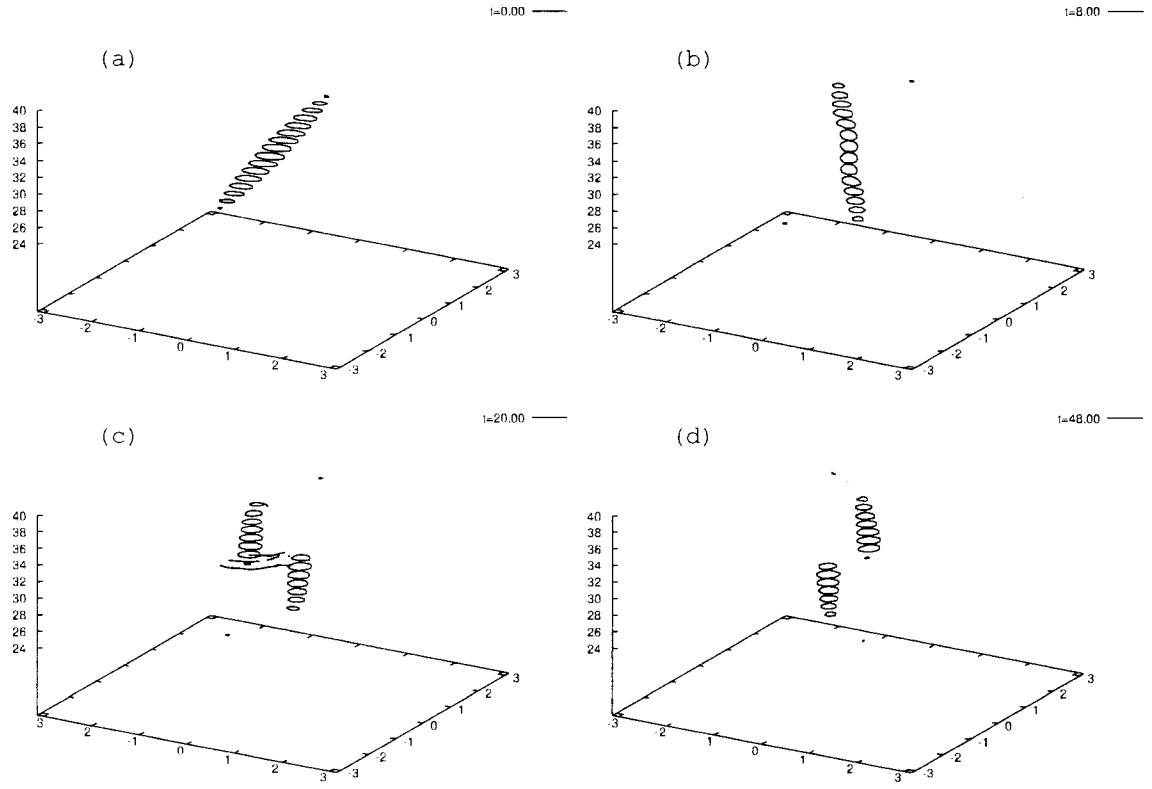

Fig. 1.5: **Strongly unstable spheroid**: Splitting, $\alpha/\gamma = 0.125$, $\Theta = 0.96$ (No.4), (a) $t = 0$, (b) $t = 8$, (c) $t = 20$, (d) $t = 48$.

evolution and the dissipative process is completed rapidly. The dotted arrows in Fig.1.3 show the spheroids created after the splitting. The resulting spheroids are almost of the same height, whereas the aspect ratios and the inclination angles differ slightly. These asymmetries become larger as the instability becomes weaker, because the asymmetries are induced stochastically during the splitting process, which takes longer to be completed if the instability is weak.

In the filamentation (No.11) and splitting (No.4) processes, considerable amounts of energy and enstrophy are 'dissipated' as shown in Figs.1.6 and 1.7, respectively. Here, the energy is the sum of the kinetic energy (x, y-derivatives) and the potential energy (z-derivative):

$$E = \frac{1}{2}\int\int\int [(\frac{\partial\psi}{\partial x})^2 + (\frac{\partial\psi}{\partial y})^2 + (\frac{\partial\psi}{\partial z})^2] dxdydz. \tag{1.69}$$

The enstrophy is defined by

$$S = \int\int\int (\Delta\psi)^2 dxdydz, \tag{1.70}$$

which is proportional to the vortex volume, given that the potential vorticity is uniform (and constant) inside the vortices and zero outside. The horizontal axis denotes the time and the vertical axis the relative energy and enstrophy (normalized by their initial values). The results concerning 'dissipation' are rather qualitative, for the dissipation by the surgical operation is not 'real'. What kind of dissipative processes should be taken in

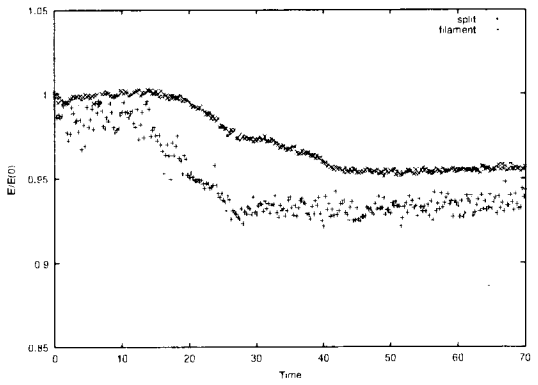

Fig. 1.6: **Time evolution of the relative energy**: filamentation × (No.11), splitting + (No.4).

account is a very complicated physical problem, and an open question to be investigated. Nevertheless, these results are insensitive to the surgical scale δ, so long as it is taken to be smaller than a tenth of the grid scale, although the energy fluctuates slightly due to the presence of fine filaments. Note that the energy dissipation is larger for the splitting process, but that the enstrophy dissipation is larger for the filamentation. In the filamentation, the energy dissipation is smaller than the enstrophy dissipation, indicating the occurence of an enstrophy cascade that is not associated with the energy cascade. This is the direct cascade of enstrophy from a large to a small scale. These dissipative processes terminate when most of the filaments emitted from the main spheroid are wrapped tightly by the differential rotation around the main vortex, and they are eliminated by the surgical operation. It takes longer for the filamentation process to settle down. The final vortex height (the sum of the heights of two vortices for the splitting cases) becomes smaller than the initial value, too (Table 1.1). The change in the vortex height is considerably large, because the filaments emitted from both the top and the bottom are finally dissipated by the surgery.

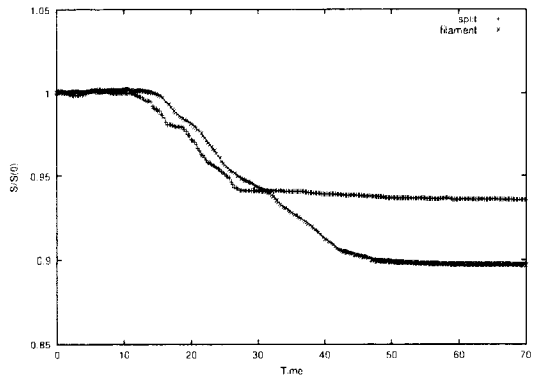

Fig. 1.7: **Time evolution of the relative enstrophy**: filamentaion × (No.11), splitting + (No.4).

In contrast, almost no height change is observed in the break-up cases. This is because filaments are emitted from the central part, and substantial portions of the potential vorticity are redistributed into two fragments created after the splitting process. Both

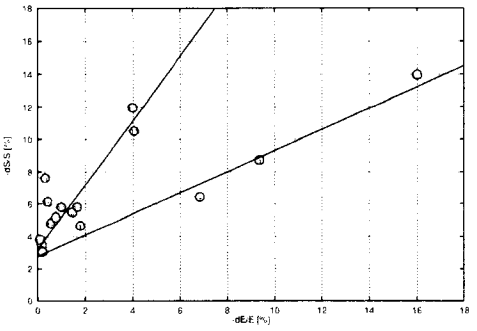

Fig. 1.8: **Correlation of the energy and enstrophy dissipation**: unstable prolate spheroidal vortices.

the energy and the enstrophy are cascaded into smaller scales in the vortex splitting process. The energy cascade in the usual direction has not been reported in previous numerical simulations of quasi-geostrophic turbulence, and its absence is linked to the fact that the break-up occurs only if the vortex is very slender and highly inclined from the vertical axis. Such vortices are rarely observed in pseudo-spectral computations, where the majority of vortices are nearly vertical and rotate stably so long as they are located sufficiently far apart. It is of interest to investigate what occurs when two vortices come closer together and interact strongly, which is the subject of the next section.

Figure 1.8 depicts the correlation between the energy dissipation and enstrophy dissipation. The horizontal axis is the energy loss and the vertical axis is the enstrophy (vorticity) loss. If the 'filamentation' and the 'break-up' are fitted separately, the data points align on two straight lines showing good correlations, although the points corresponding to filamentation scatter slightly. Noting the difference in the gradient of between the two correlation-lines, we may construct a refined vortex-based turbulence model, incorporating the dissipative effects of the filamentation and splitting.

Let us comment on the instability of oblate spheroids, briefly. An oblate spheroid, inclined from the vertical (z) axis by Θ, rotates steadily about the z-axis with a constant angular velocity Ω':

$$\Omega' = q\cosh^2\Xi_0'\sinh\Xi_0'\left\{\tan^{-1}\left(\frac{1}{\sinh\Xi_0'}\right)\left(\frac{3}{2}\cosh^2\Xi_0' - 1\right) - \frac{3}{2}\sinh\Xi_0'\right\}. \qquad (1.71)$$

This is a function of the aspect ratio $\alpha/\gamma = \coth\Xi_0'$ and it is independent of the inclination angle Θ from the vertical axis. The linear stability of a tilted oblate spheroid was investigated by Miyazaki *et al.* (1999). We plot the instability ($n = 3$ Legendre mode) growth rate as contour lines in Fig.1.9. An oblate spheroid becomes unstable against the third Legendre mode when $\alpha/\gamma >$ about 1.62. This instability is caused by a resonance phenomenon, which occurs even if the inclination angle is very small for certain aspect ratios such as 1.617, 1.796, 3.259. Similar resonance-induced instability is found for higher modes. An oblate spheroid becomes unstable against the fourth Legendre mode when $\alpha/\gamma >$ about 2.13. The parameter region, where the instability is observed, becomes narrower as the order of the Legendre function becomes higher.

Nonlinear development is computed numerically by the CASL-algorithm, and 128^3 grid points are used in most of the computations. An unstable oblate spheroid emits vortex sheets vigorously and becomes a stable spheroid. The arrows in Fig.1.9 show

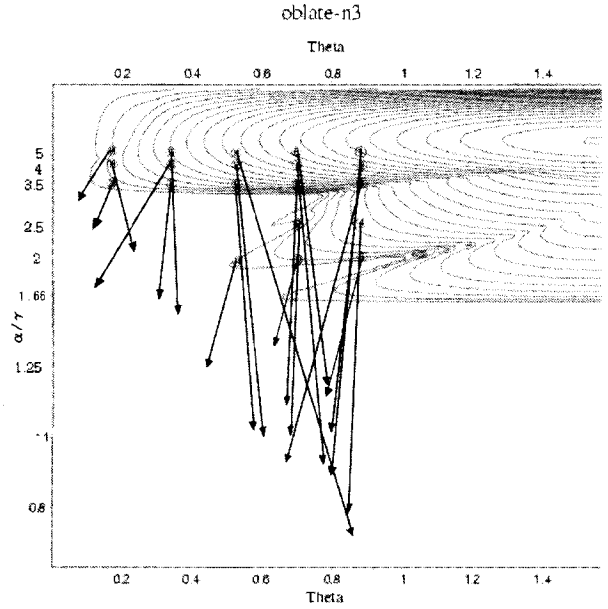

Fig. 1.9: **Instability of a tilted oblate spheroid** ($n = 3$ Legendre mode) and the spheroid born after the dissipative processes (i.e., sheet emission).

what remains after dissipative processes. In many cases the resulting vortex is a stable oblate spheroid, though even a prolate spheroid sometimes appears.

The correlation between the energy dissipation and the enstrophy dissipation is shown in Fig.1.10. We could not identify a simple relation between them, because the data points scatter widely on these plots compared those for prolate spheroids (Fig.1.8).

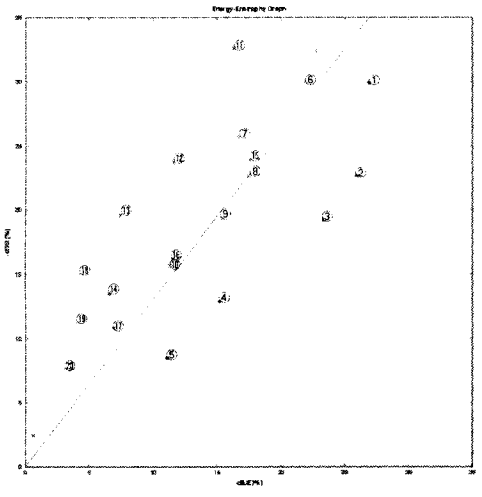

Fig. 1.10: **Correlation of the energy and enstrophy dissipation**: unstable oblate spheroidal vortices.

1.5 Merger of Co-rotating Vortices

The merger of two co-rotating vortices of like-sign plays a key role in the dynamics of quasi-geostrophic turbulence. It determines the vortex population and it is linked with the inverse energy cascade from a small to a large scale. In a vortex-based model of two-dimensional turbulence (Benzi *et al.*, 1992, Carnevale, 1991), the merging process is assumed to occur whenever the distance between two co-rotating vortices of radius R_1 and R_2 is less than $\sigma(R_1 + R_2)$ (critical distance). Here the threshold value σ was estimated to be about 1.7, based on the Elliptical Moment Model (a two-dimensional version of the ellipsoidal moment model) (Melander *et al.* 1986), and subsequent direct numerical simulations supported this value. The aim of this section is to examine whether the ellipsoidal moment model can capture the merger of two vortices.

We defined the 'merger' in the ellipsoidal moment model by the following two conditions (Miyazaki *et al.*, 2001). First, two vortices should overlap vertically; i.e., $|Z_2 - Z_1| < zh_1 + zh_2$. Second, the horizontal distance between two ellipsoids should be less than the sum of the 'average radius' of the vortices; i.e., $(\alpha_1\beta_1\gamma_1)^{1/3} + (\alpha_2\beta_2\gamma_2)^{1/3} > D(t)$. Next, we estimated the critical distance by integrating the model equations numerically (using LSODE). Figure 1.11 shows the region of the initial position of the second vortex ($a = X_2(0) - X_1(0), h = Z_2 - Z_1$), relative to the first vortex, for the case of $V_{1,2} = 0.1, zh_{1,2} = 1$. The shadowed region represents the 'defined' merger region, i.e., $a < (\alpha_1\beta_1\gamma_1)^{1/3} + (\alpha_2\beta_2\gamma_2)^{1/3}$. Starting from the region inside the broken curve (model-threshold), a merger according to the above definition occurs; i.e., the relative position $(X_2 - X_1, Z_2 - Z_1)$ falls into the shadowed zone over the course of time. We noted previously that the critical distance for a merger was almost the same as that for chaotic motions. When the motion became chaotic, the horizontal distance between two vortices oscillated irregularly with a large amplitude, which circumstance also caused the merger. Because the initial inclination angles had a minor influence on the critical distance, we have taken them to be zero ($\theta_{1,2}(0) = 0$).

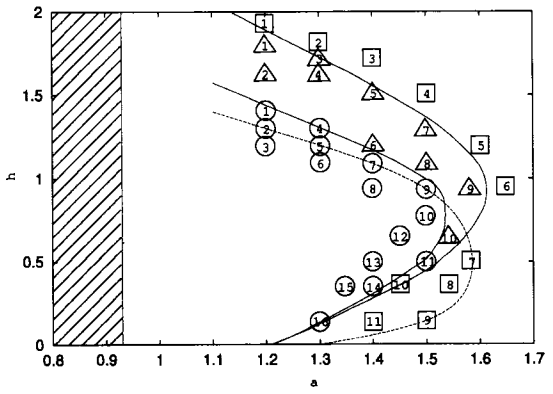

Fig. 1.11: **Merger threshold** for the cases of $V_{1,2} = 0.1$ and $\alpha_{1,2}/\gamma_{1,2} = 0.32$, $\theta_{1,2} = 0$.

1.5.1 Symmetric merger

We performed numerical simulations (CASL) in order to assess the validity of predictions based on the ellipsoidal moment model. First, symmetric merger between two vortices of the same volume, the same potential vorticity, and the same shape is investigated. The results are classified into three categories: no-merger, merger, and inter-

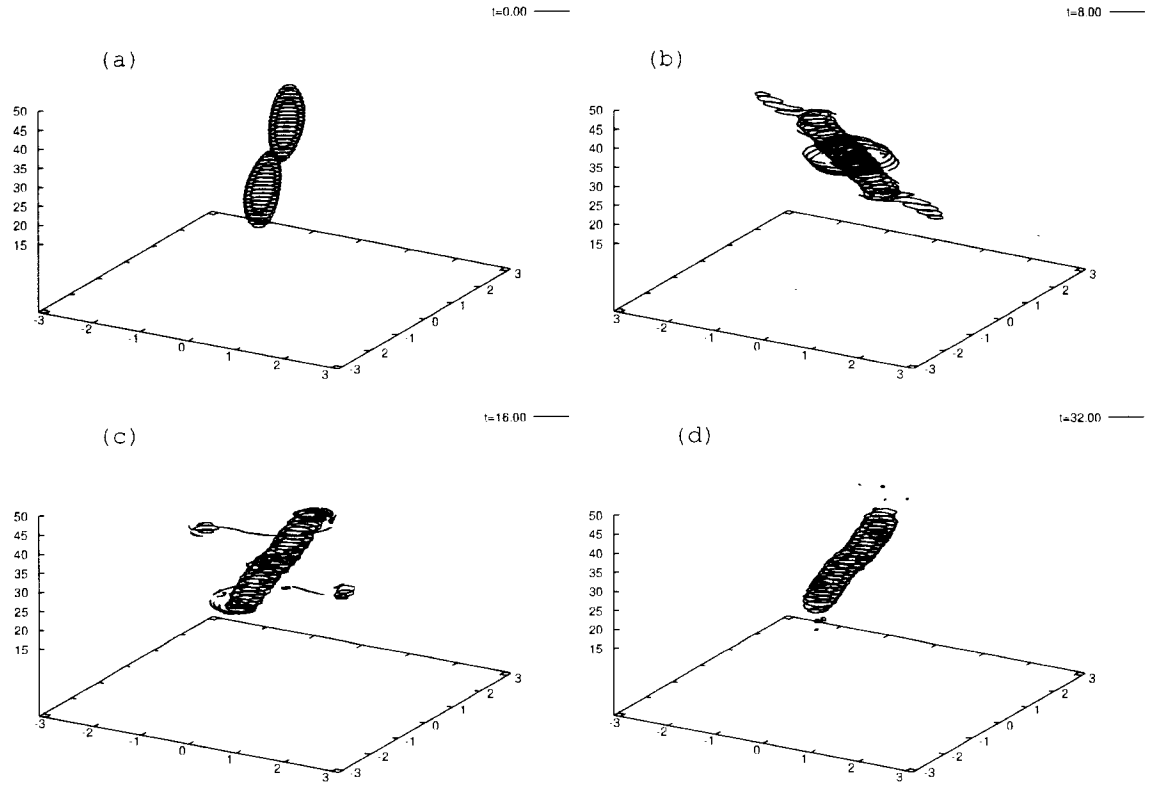

Fig. 1.12: **Merger of co-rotating vortices**: $V_{1,2} = 0.1$, $a = 1.2$, $h = 1.25$ (No.2), (a) $t = 0$, (b) $t = 8$, (c) $t = 16$, (d) $t = 32$.

mediate cases. The open squares in Fig.1.11 indicate the cases in which the vortices do not merge. The open circles denote the cases in which the merger is observed. Figure 1.12 depicts the typical time evolution of a merger (No.2 in Table 1.4). We see that thin filaments are emitted from both vortices during the merger. The time duration of the merging process becomes longer near the threshold line. The open triangles indicate the cases of intermediate and marginal behavior. The vortices merge once, then separate again into two vortices that are different from the initial vortices. This occurs because the transiently created vortex is unstable (being slender and highly inclined). The boundary between the stable and intermediate zones is represented by a solid line. The boundary between the triangle-zone and the square-zone is shown by another solid line. If the triangles are taken to belong to non-merger cases, the ellipsoidal vortex model (broken line) seems to work fairly well for the region $h > 0.5$ (large vertical off-set). The model, however, over-estimates the critical distance in the region $h < 0.5$; i.e., when the vortices are placed on nearly the same horizontal plane. The reason the ellipsoidal moment model gives poorer predictions in that region, may be traced back to the 'definition of merger' using average radii. The merger-definition can be refined by considering the geometrical shapes more properly in future work.

The next important step is to assess the properties of a vortex (or vortices) created after a merger and marginal interaction. Tables 1.3,1.4 show the list of the computed cases, which belong to the intermediate and merger categories. In contrast, Table 1.2 shows the list of stable cases, in which no dissipative event was observed. The simplest idea is to replace the merger-product by a single stable spheroid of certain energy, enstro-

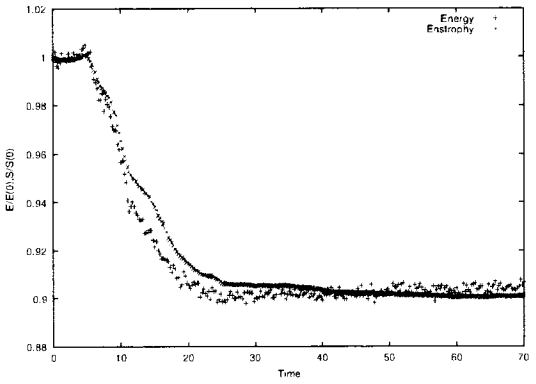

Fig. 1.13: Time-developments of the relative energy and the relative enstrophy (No.2).

phy, and angular momentum. These values are linked in some way with the properties of the parent spheroids before the merger. Here, H denotes the total height of the two vortices; i.e.,

$$H = zh_1 + zh_2 + h, \tag{1.72}$$

and ΔH is the change in H after merger. The energy and enstrophy dissipation processes during merger depend on the details of filamentation in general. Figure 1.13 shows the time-developments of the energy and the enstrophy (normalized by their initial values), corresponding to Fig.1.12 (No.2). We see that the dissipative processes end finally after merger, and a stable 'spheroid' is produced. The behavior of the relative energy is almost indistinguishable from that of the relative enstrophy. In Table 1.4, the aspect ratio and the inclination angle of the merger-product are listed. The aspect ratio decreases for large h and increases for small h, as is expected. In the latter case, the filamentation is very vigorous and substantial volumes of the initial spheroids are emitted and dissipated by surgical operations. In contrast to the merger of vortices on the same horizontal plane, which always produces a comparatively flatter vortex (Hardenberg and McWilliams, 2000), after a merger of vortices on different vertical levels a slender vortex may appear. It is of great interest whether the distribution of the aspect ratio statistically approaches the 'isotropic' state (i.e., $\alpha'/\gamma' =$ about 1), which is one of classical theoretical predictions in the inertial range (Charney, 1971). Although Hardenberg and McWilliams (2000), who considered mergers of vortices on the same horizontal plane, claims that slightly flatter vortices ($\alpha'/\gamma' < 1$) dominate the vortex-population, extensive 3D-studies are needed to verify the classical prediction. Recently, Reinaud *et al.* (2003) performed a very large numerical simulation based on the CASL-algorithm. They showed that the average height-to-width ratio of vortices was about 0.83 (i.e., an oblate spheroid), although tall vortices (prolate spheroids) are more energetic.

The correlation between the energy dissipation and the enstrophy dissipation is plotted in Fig.1.14. The non-merger cases are not plotted, based on the fact that the energy and the enstrophy are conserved within 3% if the co-rotating vortices do not merge. The numbered circles represent the merger-cases. Although the circles scatter widely, they are almost on a single line. The correlation between the energy dissipation and the enstrophy dissipation is rather good, which suggests the possibility of a simple workable law of merging reset. The reason the energy correlates so well with the enstrophy is not

Table 1.2: Stably rotating symmetric vortex pair.

No.	a	h	$-\Delta S/S(\%)$	$-\Delta E/E(\%)$	$-\Delta H/H(\%)$
1	1.20	1.90	0	0	0
2	1.30	1.80	0	0	0
3	1.40	1.70	0	0	0
4	1.50	1.50	0	0	0
5	1.60	1.30	0	0	0
6	1.65	0.90	0	0	0
7	1.58	0.50	0	0	0
8	1.54	0.30	0	0	0
9	1.50	0.13	0	0	0
10	1.45	0.30	0	0	0
11	1.40	0.13	0	0	0

Table 1.3: Marginal cases.

No.	a	h	α'/γ'	Θ'	$-\Delta S/S(\%)$	$-\Delta E/E(\%)$	$-\Delta H/H(\%)$
1	1.20	1.80	0.335	14.0	2.07	1.05	0
			0.362	4.73			
2	1.20	1.60	0.370	11.4	3.18	2.74	5.56
			0.354	23.0			
3	1.30	1.70	0.342	17.7	1.43	1.32	0
			0.357	13.0			
4	1.30	1.60	0.314	22.8	2.31	2.11	2.78
			0.354	6.56			
5	1.40	1.50	0.373	15.1	2.09	1.59	0
			0.370	6.47			
6	1.40	1.15	0.339	3.20	9.30	10.0	9.38
			0.464	25.4			
7	1.50	1.40	0.337	16.9	4.39	5.20	0
			0.381	7.83			
8	1.50	1.08	0.400	31.9	8.68	9.31	3.33
			0.487	7.18			
9	1.58	0.90	0.345	19.0	9.89	11.8	0
			0.400	13.4			
10	1.54	0.63	0.503	21.6	19.8	21.8	3.85
			0.460	16.6			

Table 1.4: Merger of co-rotating symmetric vortex pair.

No.	a	h	α'/γ'	Θ'	$-\Delta S/S(\%)$	$-\Delta E/E(\%)$	$-\Delta H/H(\%)$
1	1.20	1.40	0.137	42.4	6.14	4.12	11.8
2	1.20	1.25	0.197	35.1	9.78	8.97	18.8
3	1.20	1.15	0.279	20.3	12.6	12.0	25.0
4	1.30	1.25	0.153	43.6	7.90	6.75	12.5
5	1.30	1.15	0.239	32.1	11.0	10.4	21.9
6	1.30	1.08	0.269	28.4	13.2	12.4	23.3
7	1.40	1.08	0.377	8.93	13.4	13.2	33.3
8	1.40	0.90	0.428	7.89	19.2	17.3	32.1
9	1.50	0.90	0.372	29.7	15.9	14.8	35.7
10	1.50	0.75	0.491	20.8	18.7	15.3	42.9
11	1.50	0.50	0.556	46.5	25.3	26.3	50.0
12	1.45	0.63	0.474	38.4	19.8	17.3	46.2
13	1.40	0.50	0.660	23.0	26.4	26.5	45.8
14	1.40	0.30	0.758	35.5	28.6	28.6	54.2
15	1.35	0.30	0.830	15.3	31.9	32.5	54.2
16	1.30	0.13	0.789	33.8	29.7	29.0	50.0

clear. It might be a result of the artificial dissipation by surgery, though the behavior of the relative energy differs from that of the relative enstrophy in the filamentation process of a weakly unstable spheroid. These dissipative quantities seem to be well correlated when the dissipative processes occur and end rapidly.

We plot in Fig.1.15 the energy dissipation as a function of $\cot^{-1}(h/a)$, which is the angle from the vertical axis of the initial relative position (a, h). This variable is useful to represent a point on and around the merger threshold. The points in Fig.1.15 are fitted approximately by

$$-\frac{\Delta E}{E_0} = 0.38 \cot^{-1}(h/a) - 0.22, \tag{1.73}$$

giving a rule of thumb for the dissipative effects in the symmetric merger $V_{1,2} = 0.1, zh_{1,2} = 1$. The solid and the broken lines in Fig.1.16, show the aspect ratio α'/γ' of the merger-product as a function of $\cot^{-1}(h/a)$. Although the plotted values scatter slightly, α'/γ' seems to align on a line

$$\alpha'/\gamma' = 0.91 \cot^{-1}(h/a) - 0.50, \tag{1.74}$$

which provides a rough deterministic estimate of the merger-product.

1.5.2 Asymmetric merger

Next, let us consider asymmetric mergers; i.e., $V_1 = 0.1$, $V_2 = 0.5$, $zh_{1,2} = 1$, $\theta_{1,2} = 0$. The second vortex with the aspect ratio $\alpha_2/\gamma_2 = 0.71$ is flatter than the first vortex of the $\alpha_1/\gamma_1 = 0.32$. Figure 1.17 shows a comparison between the prediction of the ellipsoidal moment model (broken line) and the numerical results of the CASL-computation. When the vortices merge (open circles) fully, the first (slender) vortex emits filaments from its

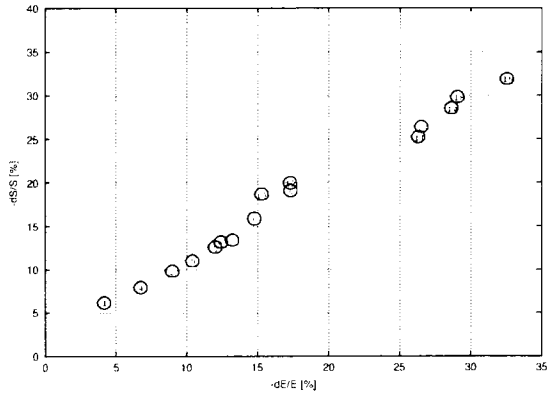

Fig. 1.14: **Correlation between the energy dissipation and the enstrophy dissipation**: merger of co-rotating vortices.

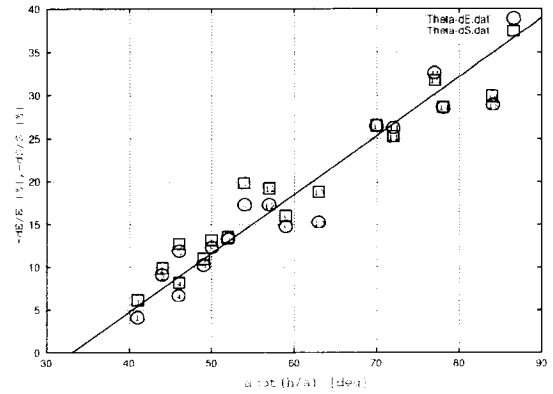

Fig. 1.15: **Energy and enstrophy dissipation** as functions of $\cot^{-1}(h/a)$.

top and bottom and then it is absorbed entirely into the second (flatter) vortex. The triangles show intermediate cases (partial merger), in which only the filaments emitted from the top of the slender vortex are captured by the flatter vortex, and the lower part of the slender vortex remains apart from the flatter vortex (Fig.1.18). This region spreads widely along the threshold line (broken line) determined by the ellipsoidal moment model. The products after the dissipative interaction are listed in Tables 1.5-1.7. We see that the first vortex loses almost half of its original volume, whereas the second vortex retains its original shape or expands slightly, absorbing some of the filaments ejected from the first vortex. This process, which has not yet been reported, is a new dynamical process linked to the energy and enstrophy cascades. Unfortunately, the prediction of the ellipsoidal moment model is not so accurate (quantitatively) in these asymmetric interactions, for the intermediate zone expands widely outside the merger region of the model. Two solid lines in Fig.1.17 represent the contours of equi-relative energy dissipation ($-\Delta E/E_0$=0.1(outer), 0.05(inner)). This suggests that 'two-to-one' mergers might not be dominant dissipative events in quasi-geostrophic turbulence, but that vorticity-exchange between two vortices plays a substantial role. During the vorticity-exchange, the enstrophy is cascaded into a smaller scale, whereas the energy is transferred partly to a smaller scale and partly to a larger scale. It is important to estimate the contribution of the vorticity-exchange process to the energy and enstrophy transfer in the

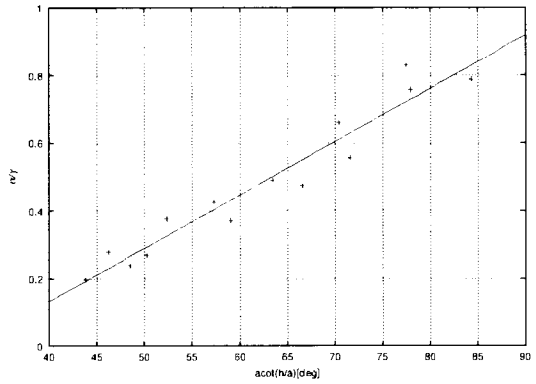

Fig. 1.16: **Aspect ratio of the merger-product** as a function of $\cot^{-1}(h/a)$.

Table 1.5: **Stably rotating asymmetric vortex pair.**

No.	a	h	$-\Delta S/S(\%)$	$-\Delta E/E(\%)$	$-\Delta H/H(\%)$
1	1.60	2.20	0	0	0
2	1.60	2.00	2.49	2.08	0
3	1.80	2.20	0	0	0
4	1.80	2.00	2.80	2.09	0
5	2.00	2.20	0	0	0
6	2.00	2.00	0	0	0
7	2.00	1.76	3.60	3.07	0
8	2.16	1.90	0	0	0
9	2.16	1.46	4.87	4.26	0
10	2.30	1.76	0	0	0
11	2.30	1.00	5.35	4.49	0
12	2.40	0.20	0	0	0

quasi-geostrophic turbulence.

The aspect ratios $\alpha'_{1,2}/\gamma'_{1,2}$ of the first (initially slender) and second (initially flatter) vortices after vorticity-exchange are plotted as functions of $\cot^{-1}(h/a)$ in Fig.1.19. The slender vortex becomes considerably flatter, for it loses almost half of its original volume. It is noted that the aspect ratio does not depend on $\cot^{-1}(h/a)$. This is similar to the splitting of the highly unstable slender spheroid, observed in the previous section. The second vortex does not change at all for larger $\cot^{-1}(h/a)$, in which cases the filaments emitted from the first vortex dissipated completely. The second vortex becomes slightly taller for smaller $\cot^{-1}(h/a)$ by capturing some filaments emitted from the first vortex at its bottom. This vorticity-exchange between an asymmetric vortex pair has a profound effect on the vortex population dynamics. The vorticity-exchange events must be taken properly into account in order to construct a workable 'dissipative vortex-based model' of quasi-geostrophic turbulence. Much more extensive and elaborate studies are required to this end.

We performed direct numerical simulations (CASL) in order to assess the validity of the ellipsoidal moment model, which was extracted from the partial differential equations

Table 1.6: Merger of asymmetric vortex pair.

No.	a	h	α'/γ'	Θ'	$-\Delta S/S(\%)$	$-\Delta E/E(\%)$	$-\Delta H/H(\%)$
1	1.60	1.14	0.720	16.1	12.1	10.7	37.5
2	1.80	0.93	0.702	17.0	12.5	10.3	28.6
3	1.90	0.50	0.696	23.4	12.5	10.3	16.7
4	1.90	0.21	0.789	27.7	12.0	10.4	25.0
5	1.80	0.21	0.802	18.7	13.6	11.4	25.0

Table 1.7: Partial merger of asymmetric vortex pair.

No.	a	h	α'/γ'	Θ'	$-\Delta S/S(\%)$	$-\Delta E/E(\%)$	$-\Delta H/H(\%)$
1	1.60	1.76	0.809,0.523	12.9,29.4	6.90	6.26	16.7
2	1.60	1.64	0.645,0.563	10.6,18.1	9.32	8.25	11.1
3	1.60	1.56	0.618,0.787	19.6,44.4	9.35	7.73	22.2
4	1.60	1.28	0.667,0.576	25.9,47.5	11.5	10.2	18.8
5	1.70	1.60	0.634,0.599	13.6,39.1	8.70	7.54	11.1
6	1.70	1.56	0.663,0.702	12.3,27.9	9.03	8.27	16.7
7	1.70	1.46	0.644,0.471	14.4,25.6	9.75	8.85	22.2
8	1.70	1.14	0.707,0.753	19.8,43.9	12.8	12.2	18.8
9	1.80	1.50	0.708,0.561	9.12,40.0	9.38	8.16	22.2
10	1.80	1.46	0.722,0.539	8.64,46.2	8.49	7.47	22.2
11	1.80	1.28	0.676,0.808	23.7,51.8	10.6	9.79	18.8
12	1.90	1.46	0.706,0.510	13.2,35.1	7.55	6.67	16.7
13	1.90	1.28	0.711,0.590	18.2,39.0	9.66	8.29	12.5
14	1.90	1.14	0.711,0.670	18.5,30.9	11.8	9.84	12.5
15	1.90	0.93	0.676,0.471	20.7,53.1	13.4	10.8	7.14
16	2.00	1.28	0.720,0.540	11.7,19.1	9.66	8.23	6.25
17	2.00	1.14	0.737,0.550	14.5,46.4	10.6	8.85	12.5
18	2.00	0.93	0.719,0.679	10.0,27.6	11.3	9.28	0
19	2.00	0.50	0.675,0.572	20.9,47.7	12.8	10.1	0
20	2.00	0.21	0.769, 0.392	15.1,62.1	12.6	9.95	16.7
21	2.10	1.14	0.716,0.619	9.98,21.6	9.35	7.85	6.25
22	2.10	0.93	0.720,0.605	16.2,10.2	9.69	7.77	0
23	2.10	0.50	0.715,0.710	4.13,6.63	11.8	9.58	0
24	2.10	0.21	0.796,0.524	11.3,34.9	9.78	7.92	16.7
25	2.16	0.93	0.700,0.509	16.8,29.7	8.75	6.84	0
26	2.16	0.50	0.709,0.568	17.1,25.3	9.97	7.85	0
27	2.30	0.21	0.696,0.412	29.9,23.6	8.52	6.42	16.7

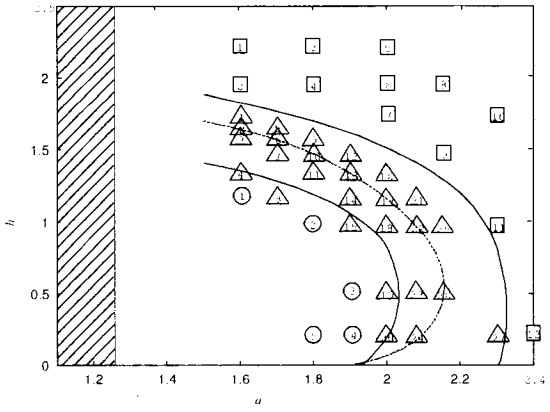

Fig. 1.17: Asymmetric interaction between two co-rotating vortices.

governing the dynamics of quasi-geostrophic fluid motion, by a systematic 'Hamiltonian moment reduction' procedure. According to the CASL simulation, weakly unstable tilted spheroidal vortices emit thin filaments, and strongly unstable spheroidal vortices are broken up into two pieces. In both cases, considerable amounts of energy and enstrophy are dissipated. We found that the critical distance of a merger is well estimated by the ellipsoidal moment model. If we can define the properties of the ellipsoidal vortex (vortices) created after the filamentation, the break-up, and the merger of co-rotating vortices, we can perform a dissipative 'quasi-turbulence simulation'. We have proposed a deterministic rule for the symmetric merger ($V_1 = V_2 = 0.1$), although stochastic description seems to be required in the asymmetric merger ($V_1 = 0.1, V_2 = 0.5$). It will be of interest to investigate the statistical properties of quasi-geostrophic turbulence, especially to see what kind of similarity laws will hold in the quasi-geostrophic turbulence, where the energy is inversely cascading.

1.6 Counter-rotating Vortex Pair

The remaining phenomenon to be studied in this section is the interaction of a counter-rotating vortex pair. We investigate the motion of a counter-rotating pair of two vortices of the same shape, a so-called 'dipole'(Miyazaki *et al.*, 2003). Here a 'dipole' means a counter-rotating pair of ellipsoids with vanishing total vorticity: $\hat{\Gamma}_1 + \hat{\Gamma}_2 = 0$. They are vertically off-set, i.e., they are placed on two horizontal planes of slightly different vertical height. A stable dipole translates for a long distance and may play an important role in the 'long range scalar transport' that occurs in geophysical flows. There have been many reports on the motion and stability of a two-dimensional dipole (Flierl, 1987), and Berestov obtained three-dimensional quasi-geostrophic dipole-solutions (under uniform stratification) (Brestov, 1979), but we know little about the behavior of a vertically off-set three-dimensional dipole.

1.6.1 Prediction of the Ellipsoidal Moment Model

We consider the motion of two interacting ellipsoidal vortices of uniform potential vorticity $q_1 = -q_2$, whose centers of vorticity are located at $(X_{1,2}, Y_{1,2}, Z_{1,2})$. The potential vorticity is uniform inside both ellipsoids and the principal axes lengths are denoted by $\alpha_{1,2}, \beta_{1,2}, \gamma_{1,2}$. Their orientations are specified by the Euler angles $\phi_{1,2}, \theta_{1,2}, \psi_{1,2}$. We have seen that there are three Casimirs linked with the volume $V_i = \alpha_i\beta_i\gamma_i$, Z_i and the

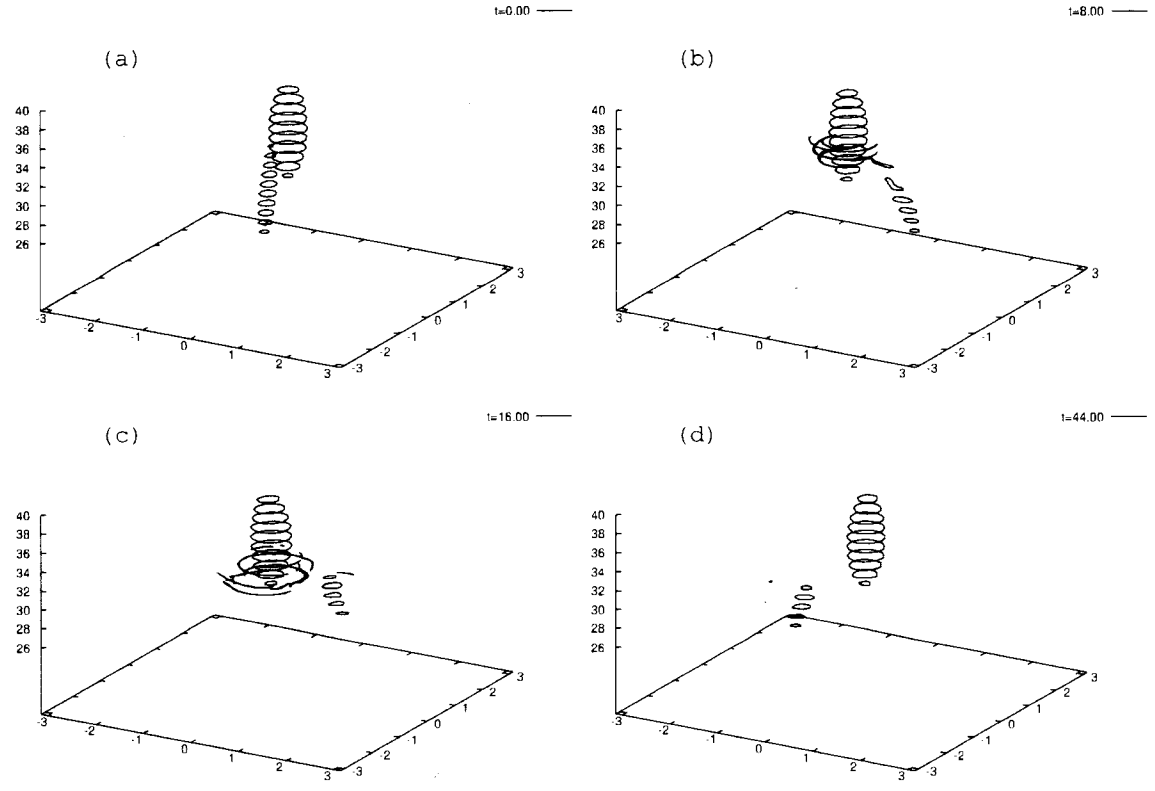

Fig. 1.18: **Partial merger of co-rotating vortices** (No.22), (a) $t = 0$, (b) $t = 8$, (c) $t = 16$, (d) $t = 44$.

vortex-height

$$zh_i = \sqrt{(\alpha_i^2 \cos^2 \psi_i + \beta_i^2 \sin^2 \psi_i) \sin^2 \theta_i + \gamma_i^2 \cos^2 \theta_i}. \tag{1.75}$$

Then the number of independent variables is reduced to 6; i.e., three degrees of freedom for each vortex. Actually, we can extract the set of canonical variables $X_i, Y_i, R_i, \Theta_i, S_i, \Phi_i$ as shown in Miyazaki *et al.* (2000). Even a two-ellipsoids system with 'six degrees of freedom' is not integrable, because the number of the Poisson-commutable invariants (i.e., 'three'), is less than the degrees of freedom of the system. In this section we consider a counter-rotating vortex pair ($\Gamma_1 + \Gamma_2 = 0$). If we assume, further, the symmetry $X_1 = -X_2$, $Y_1 = Y_2$ and $\alpha_1 = \alpha_2$, $\beta_1 = \beta_2$, $\gamma_1 = \gamma_2$ (one of them being implied in the relation $V_1 = V_2$), and $\theta_1 = \theta_2$, $\phi_1 = -\phi_2$, $\psi_1 = -\psi_2$ (one of them being implied in the relation $zh_1 = zh_2$), the degree of freedom is reduced to 3 (i.e., equal to that of a single body problem) and the system becomes integrable; 6 additional constraints are imposed upon 12 independent variables.

We integrate the equations of motion numerically, using the package code 'LSODE', starting from a set of initial conditions. In Case A, we consider very slender spheroids with aspect ratios $\alpha_{1,2}/\gamma_{1,2} = 0.1$. Both spheroids are vertically standing at the initial time. The vortex heights are taken to be unity: $zh_{1,2} = 1$. The initial vortices are placed on the $x - z$ plane and off-set vertically, in general. The interaction of symmetric fatter spheroids is studied in Case B. The initial aspect ratios of vortices are taken to be 0.3162. Other parameters are the same as those in Case A. Finally, in Case C, we investigate symmetric spheroids fatter than those in Case B. The aspect ratios are taken to be 0.7071

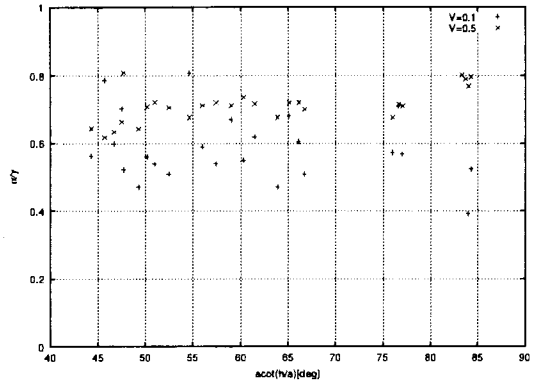

Fig. 1.19: **Aspect ratios of two vortices after partial merger** as functions of $\cot^{-1}(h/a)$: initially slender vortex (+) and initially flatter vortex (×).

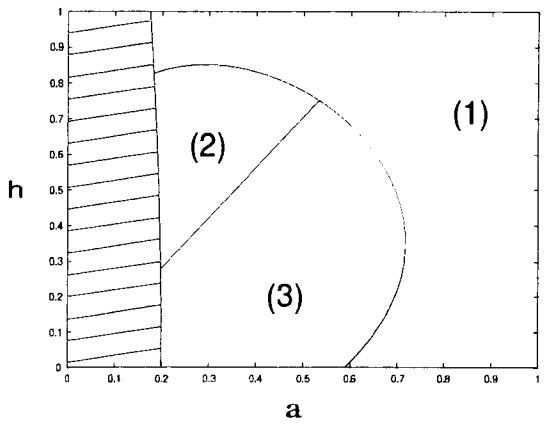

Fig. 1.20: **Three patterns found in Case A.**

and no singular behavior is observed.

Figure 1.20 shows the results for Case A, where the horizontal axis denotes $a = X_2(0) - X_1(0)$ and the vertical axis $h = Z_2(0) - Z_1(0)$. The shadowed region represents the region where two vortices initially overlap. The behavior is classified into three categories. If the vortices are far apart initially as in region (1), they translate in the positive y direction. Figure 1.21 shows the y component of the translation velocity for the case of $a = 0.8, h = 0.4$. The average value of the y component is positive in region (1), although negative values are observed when the vortex inclination is large. The inclination angle from the vertical axis oscillates periodically (the time period is about 22.5), as shown in Fig.1.22, where $\theta_1 = \theta_2$ is plotted as a function of time. Figure 1.23 depicts the orientation in the horizontal plane $\phi_1 = -\phi_2$. The first ellipsoid rotates counter-clockwise periodically during a time period of 22.5, and the second vortex rotates in the clockwise direction during the same time period. When the vortex stands almost vertically, ϕ_1 changes from $3\pi/2(-\pi/2)$ to $\pi/2$ very quickly.

When the vortices are located closer initially, two qualitatively different motions are observed. If the vortices are initially within a critical distance and off-setted vertically, as in region (2) of Fig.1.20, where h/a is larger than some critical value near 1.4 (whose meaning will be explained later), the dipole translates in the negative y direction ($a = 0.3, h = 0.6$: Fig.1.24). The oscillation amplitude of the inclination angle increases

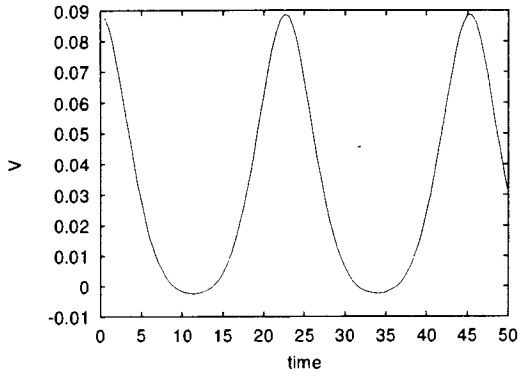

Fig. 1.21: **The y component of the translation velocity of the dipole**: $(a, h) = (0.8, 0.4)$, region (1).

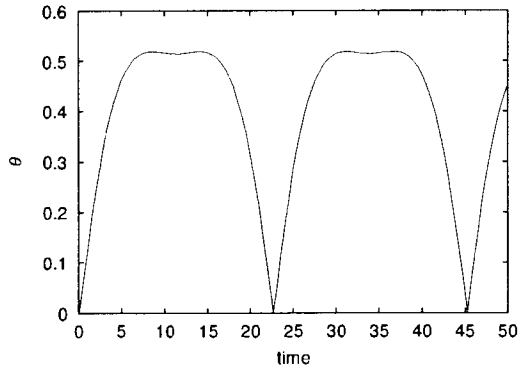

Fig. 1.22: **The inclination angle $\theta_1 = \theta_2$**: (a, h) $(0.8, 0.4)$, region (1).

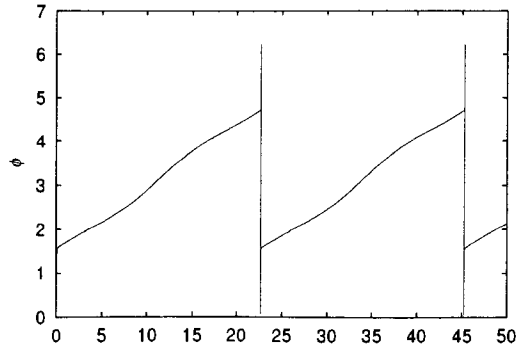

Fig. 1.23: **The orientation angle $\phi_1 = -\phi_2$**: $(a, h) = (0.8, 0.4)$, region (1).

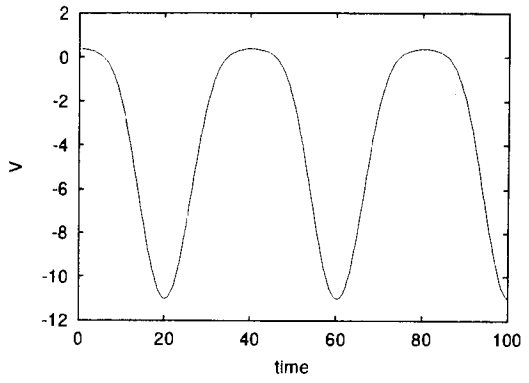

Fig. 1.24: **The y component of the translation velocity of the dipole**: $(a, h) = (0.3, 0.6)$, region (2).

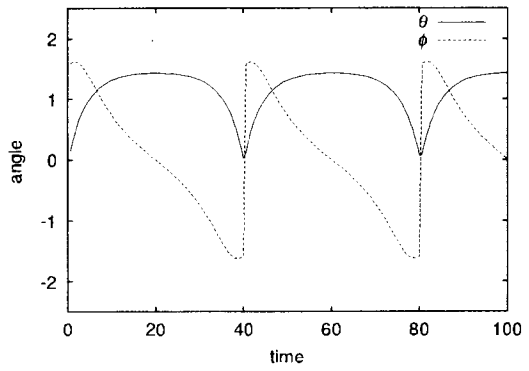

Fig. 1.25: **The inclination angle $\theta_1 = \theta_2$ (solid line) and the orientation angle $\phi_1 = -\phi_2$ (broken line)**: $(a, h) = (0.3, 0.6)$, region (2).

$(a = 0.3, h = 0.6$: broken line in Fig.1.25), and the maximum value of $\theta_1 = \theta_2$ approaches $\pi/2$ but cannot exceed $\pi/2$ because the vortex heights $zh_{1,2}$ are Casimirs and both the top and the bottom of vortices move on the same horizontal planes where they are placed initially. The orientation of the first vortex in the horizontal plane rotates clockwise, and $\phi_1 (= -\phi_2)$ again changes from $3\pi/2 (-\pi/2)$ to $\pi/2$ very quickly (see Fig.1.25). Along the threshold line between regions (1) and (2), there may be found a series of initial positions starting from which the vortices do not translate on average and only precess. In this region, the correction terms in the equations of the vortex centroid translation exceed the basic terms due to point vortex approximation. We will assess the validity of the model prediction carefully by performing direct numerical simulations, since the truncated higher order terms might exert a substantial influence.

The most striking thing occurs when the vertical off-set becomes smaller (region (3) in Fig.1.20). Both vortices are stretched infinitely, and their inclination angles $\theta_{1,2}$ tend to $\pi/2$ monotonically $(a = 0.4, h = 0.2$: solid line in Fig.1.26). Simultaneously, the orientation angle $\phi_1 = -\phi_2$ tends to a certain limiting value $(a = 0.4, h = 0.2$: broken line in Fig.1.26). The vortex pair translates in the negative y direction (Fig.1.27), and the magnitude of the translation velocity increases exponentially. Because of this singular behavior, the numerical computation of the ellipsoidal moment model stops in region (3), which is a serious drawback of the ellipsoidal moment model (and of the Wire-Vortex

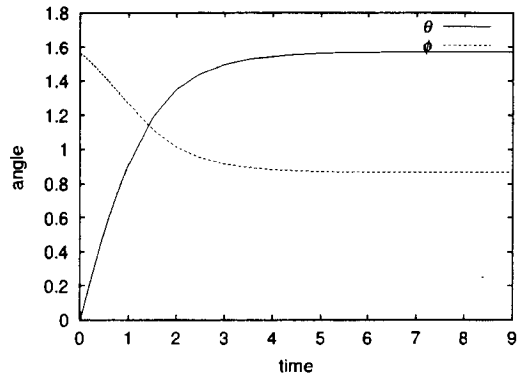

Fig. 1.26: **The inclination angle $\theta_1 = \theta_2$ (solid line) and the orientation angle $\phi_1 = -\phi_2$ (broken line)**: $(a, h) = (0.4, 0.2)$, region (3).

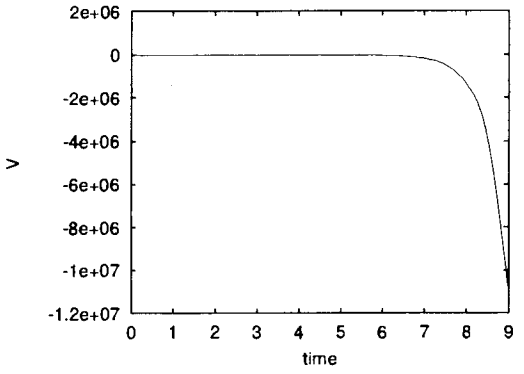

Fig. 1.27: **The y component of the translation velocity of the dipole**: $(a, h) = (0.4, 0.2)$, region (3).

model, which was derived in the limit of a very slender ellipsoid) in computing 'turbulent interaction' of many ellipsoidal vortices with both positive and negative potential vorticities. Nevertheless, this singularity is of some interest from the theoretical viewpoint. Because the ellipsoidal moment model has been derived systematically from the partial differential equation (i.e., the 'quasi-geostrophic equation'), which is thought to be a good approximation for describing geophysical fluid motions, this singularity might be carried over from the original partial differential equation. We will come back to this issue in the following subsection, where the results of direct numerical computations (CASL) are described.

We consider symmetric interaction between fatter (but still slender) vortices $\alpha_{1,2}/\gamma_{1,2} = 0.316$ in Case B. As in Case A, we find three patterns, depicted in Fig.1.28, as follows: (1) stable translation in the positive y direction, (2) translation in the negative y direction with large precessions, and (3) singular behavior (tilting down) of both vortices.

In region (1), as shown in Figs.1.29,1.30 ($a = 1.2, h = 0.6$), the motion is doubly time-periodic with a main period of 46.2 and the secondary period of 6.18. The translation velocity in the region (1) is always positive. The translation velocity for the same values of (a, h) is faster than that in Case A, because the shortest distance between vortices decreases as the vortices become fatter, which accelerates the translation. The faster oscillation of smaller amplitude is superimposed on the main precession. The secondary

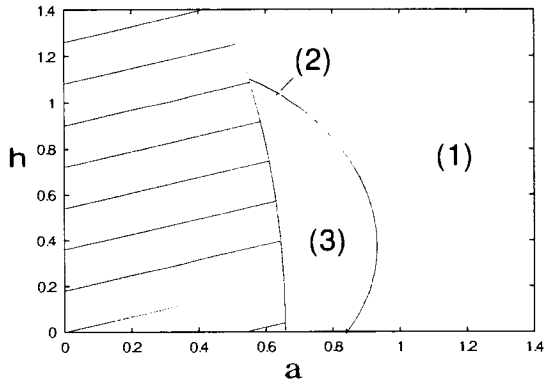

Fig. 1.28: Three patterns found in Case B.

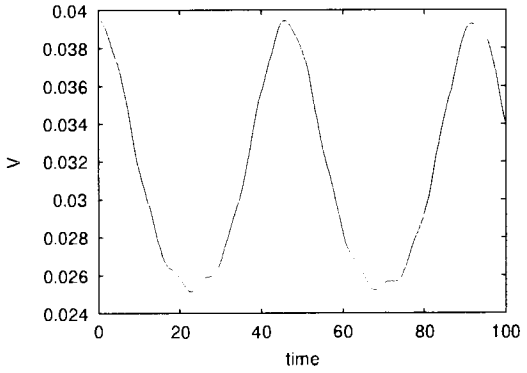

Fig. 1.29: The y component of the translation velocity: $(a, h) = (1.2, 0.6)$, region (1).

oscillation is associated with a change in aspect ratio $\alpha_{1,2}/\beta_{1,2}$ in the plane perpendicular to the longest principal axis ($\gamma_{1,2}$). The principal axes lengths $\alpha_{1,2}, \beta_{1,2}, \gamma_{1,2}$ oscillate rapidly (Fig.1.30), where $\gamma_{1,2}$ remain the longest principal semi-axes. The inclination angle $\theta_1 = \theta_2$ and the orientation angle $\phi_1 = -\phi_2$ (not shown) behave mainly as they do in Case A (Figs.1.22 and 1.23), though small secondary faster oscillations are superimposed on the main oscillation.

In region (2), both the inclination and orientation change slowly and non-periodically, as illustrated in Fig.1.31 ($a = 0.6, h = 0.95$). This is because the selected initial data point is located close to the threshold line ($h/a = 1.41$) between (2) and (3). Until $t =$ about 160, the inclination angle increases and so does the longest principal semi-axis γ_1, whereas the translation velocity decreases. For $t > 160$, the largest axis γ_1 decreases and each ellipsoid takes a pancake-like form (not a wire-like form), because α_1 remains of the order of unity and only β_1 decreases to zero. For $t > 275$, $\theta_1 = \theta_2$ exceeds $\pi/2$, which seems quite strange if we imagine only wire-like vortices. This is, however, geometrically possible for pancake-like vortices, although pancake-like vortices thus inclined might be unstable (Miyazaki *et al.*, 2002). A similar tendency is found in Case A (region (2)) in the area above the straight line $h/a = 1.41$. The translation velocity increases for $t > 160$ as the top point returns to the initial position (Fig.1.32).

In region (3), both vortices are stretched infinitely as was observed in Case A (Fig.1.34). The critical distance considerably increases compared with that of Case A,

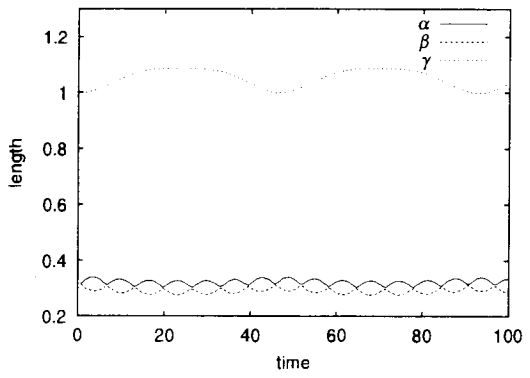

Fig. 1.30: **The principal semi-axes lengths** $\alpha_1 = \alpha_2$, $\beta_1 = \beta_2$ and $\gamma_1 = \gamma_2$: $(a, h) = (1.2, 0.6)$, region (1).

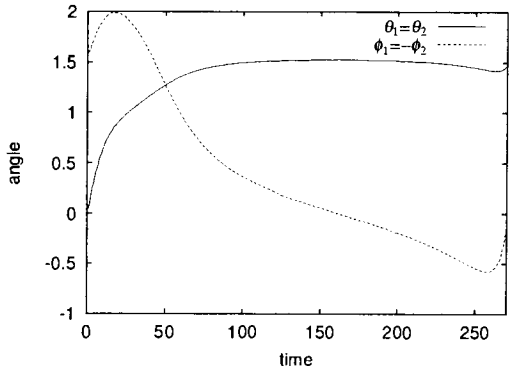

Fig. 1.31: **The inclination angle** $\theta_1 = \theta_2$ **and the orientation angle** $\phi_1 = -\phi_2$ for $a = 0.6, h = 0.95$: $(a, h) = (0.6, 0.95)$, region (2).

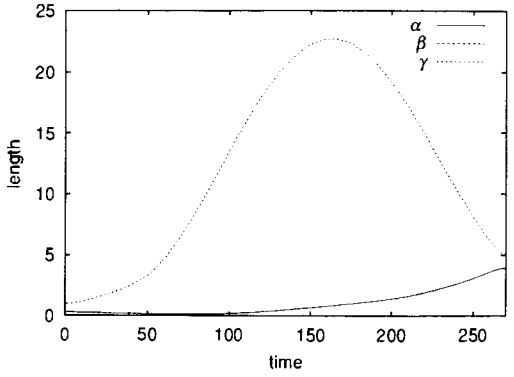

Fig. 1.32: **The principal semi-axes lengths** $\alpha_1 = \alpha_2$, $\beta_1 = \beta_2$ and $\gamma_1 = \gamma_2$: $(a, h) = (0.6, 0.95)$, region (2).

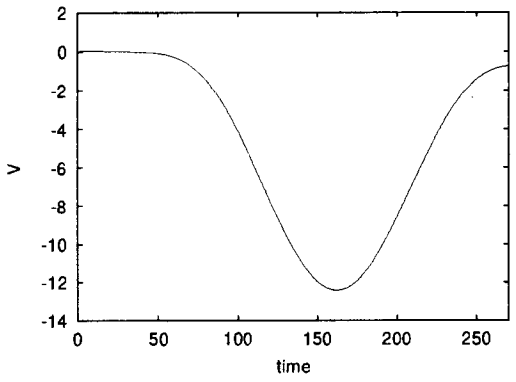

Fig. 1.33: **The y component of the translation velocity**: $(a, h) = (0.6, 0.95)$, region (2).

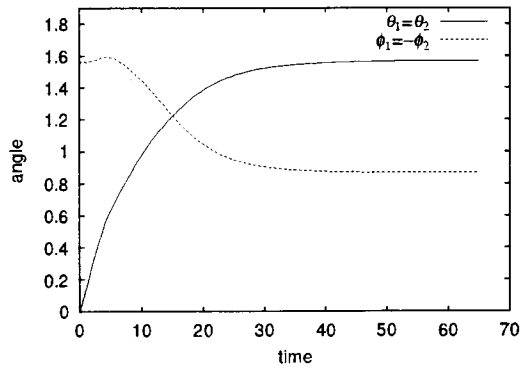

Fig. 1.34: **The inclination angle $\theta_1 = \theta_2$ and the orientation angle $\phi_1 = -\phi_2$**: $(a, h) = (0.8, 0.4)$, region (3).

whereas only a small portion of the region (2) is out of the shadowed zone showing the initial overlap. Tilting down takes much longer for the fatter pair starting from $(0.8, 0.4)$ than for the slender pair starting from $(0.4, 0.2)$ (Case A). The gradient h/a of the boundary-line between the regions (2) and (3) is again about 1.41. The tilting pair translates along the y axis in the negative direction, as it does in Case A.

Finally, it is noteworthy that no singular behavior is observed in the symmetric interactions between still fatter vortices, such as $V_{1,2} = 0.5$ (Case C). If the vortices do not overlap initially, any dipole translates in the positive y direction with moderate precessional motion. Then we see that the singularity occurs 'only for tall vortices'. The ellipsoidal moment model appears to be able to describe the interactions between fatter vortices with $\alpha/\gamma >$ about 2/3. In the recent numerical simulations of quasi-geostrophic turbulence (Reinaud *et al.*, 2003), it has been shown that the major vortices in the turbulence are identified as 'oblate spheroids' whose aspect ratio α/γ is greater than unity.

It will be of interest to investigate, by direct numerical simulations of the full quasi-geostrophic equations of motion, what occurs in the catastrophic regions for tall vortices. The above model predictions might be of limited value in these regions, where the truncation error in representing the mutual interaction by the moments up to the second order becomes larger and the shape of vortex largely deviates from the ellipsoidal form. It is necessary to check the prediction based on the ellipsoidal moment model carefully. In particular, the singular behavior of slightly off-setted vortex pairs ($h/a < 1.41$) might

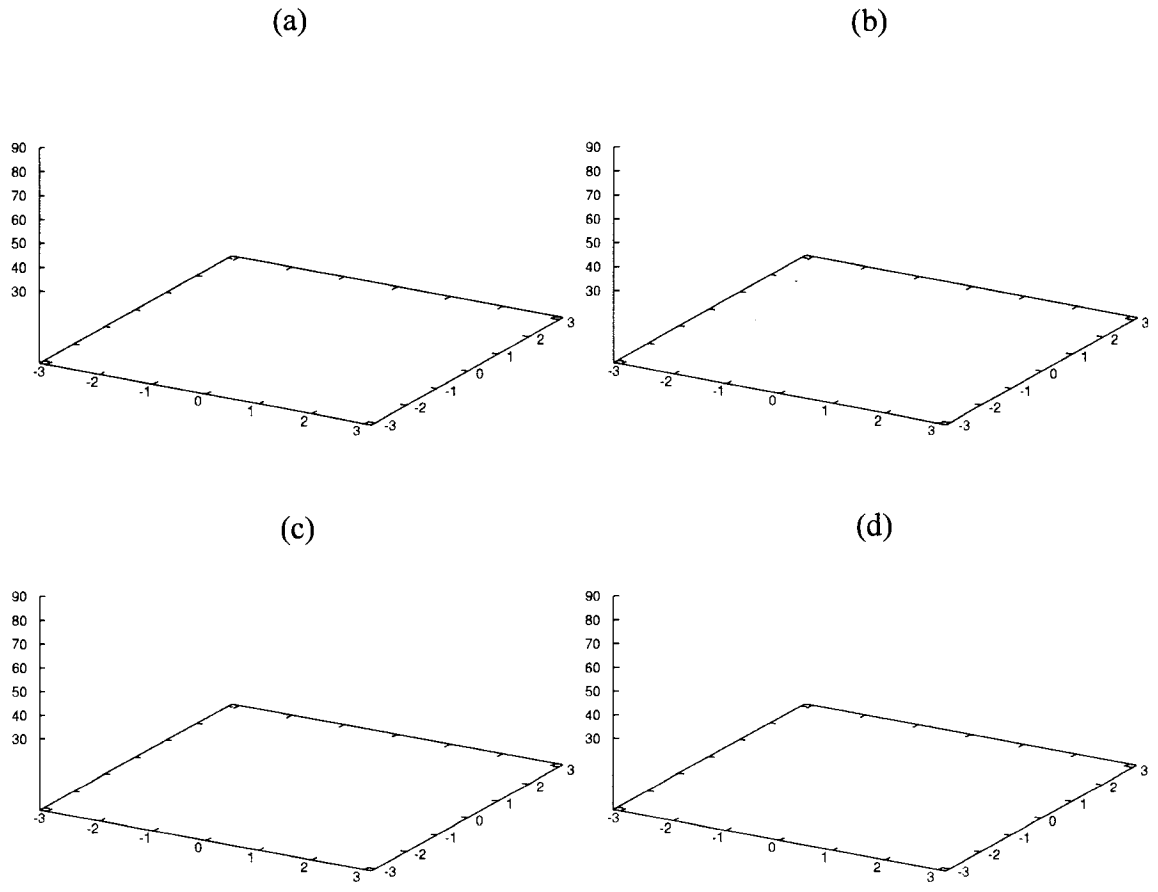

Fig. 1.35: **Time evolution of the stable dipole**: case (1), $(a, h) = (1.2, 0.6)$.

be circumvented in the 'original quasi-geostrophic approximation'.

1.6.2 CASL-Simulations

In order to investigate the effects of the shape deformation of an ellipsoid and the dissipative processes that are neglected in the ellipsoidal moment model, we performed direct numerical simulations of the quasi-geostrophic equation based on the CASL-algorithm. The dissipative effects are taken into account by an artificial procedure called 'surgery'. A surgical operation is performed whenever the distance between two contours containing the same potential vorticity becomes less than a surgical scale δ. This operation introduces an artificial viscosity into the numerical computation. Although its relation to the physical viscosity is not clear, we expect that dissipative effects are approximately incorporated by the surgery process. The computational results are insensitive to the surgical scale δ as long as it is taken to be less than one tenth of the grid scale Δ, although the computational time depends severely on δ.

We performed numerical computations corresponding to Case B (vertically standing symmetric spheroids of $\alpha_{1,2}/\gamma_{1,2} = \beta_{1,2}/\gamma_{1,2} = 0.316$), with the resolution $\Delta = 2\pi/256$ (128^3 Fourier modes) and the surgical scale $\delta = \Delta/10$. A rigid-lid boundary condition of Neumann-type is applied at the top and bottom boundaries. Three runs, with the initial conditions $(a, h) = (1.2, 0.6), (0.6, 1.0)$, and $(0.8, 0.4)$, are illustrated in Figs.1.35-1.37, respectively. These correspond to three qualitatively different cases of Case B, as follows; (1) stable translation in the positive y-direction: $(a, h) = (1.2, 0.6)$; (2) translation in the

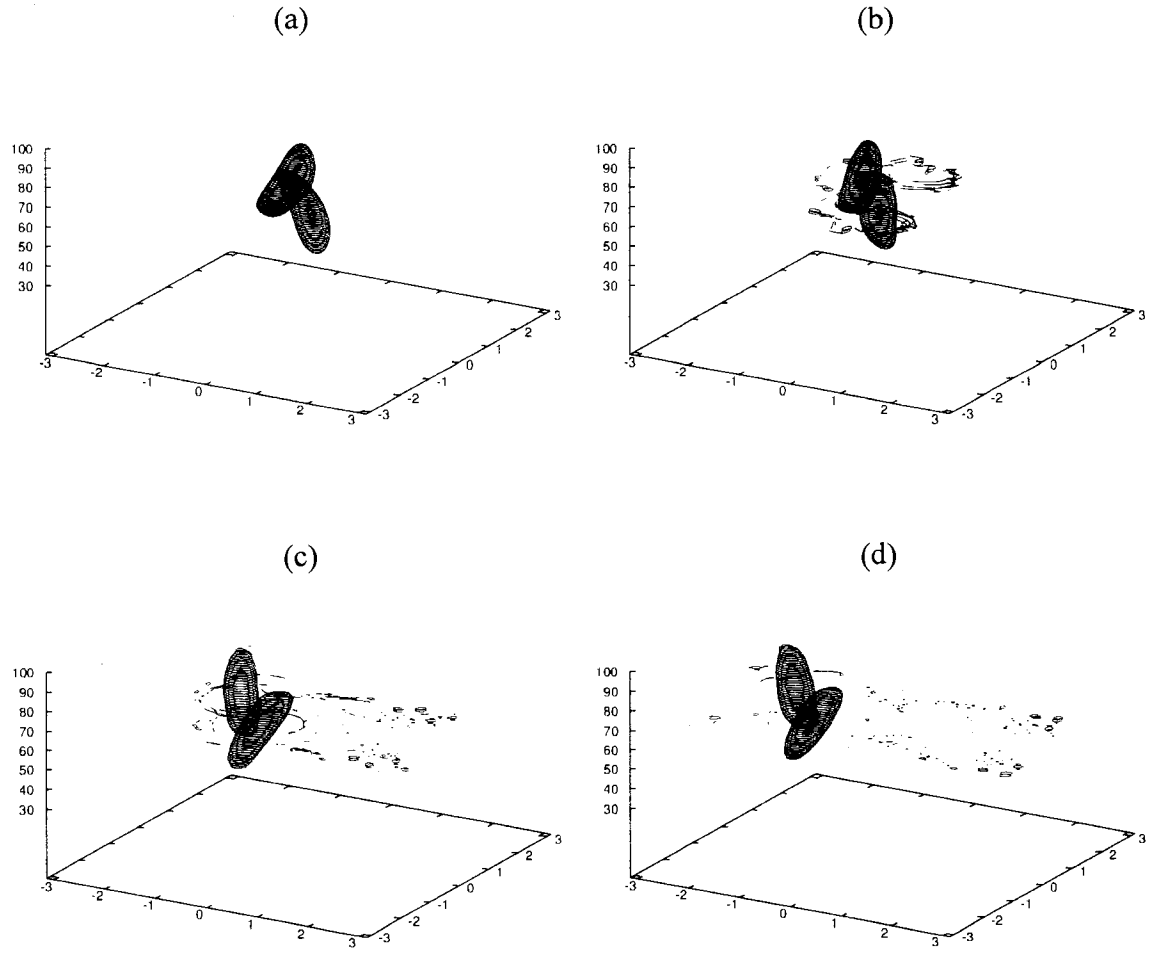

Fig. 1.36: **Time evolution of the dipole emitting filaments and satellites**: case (2), $(a, h) = (0.6, 1.0)$.

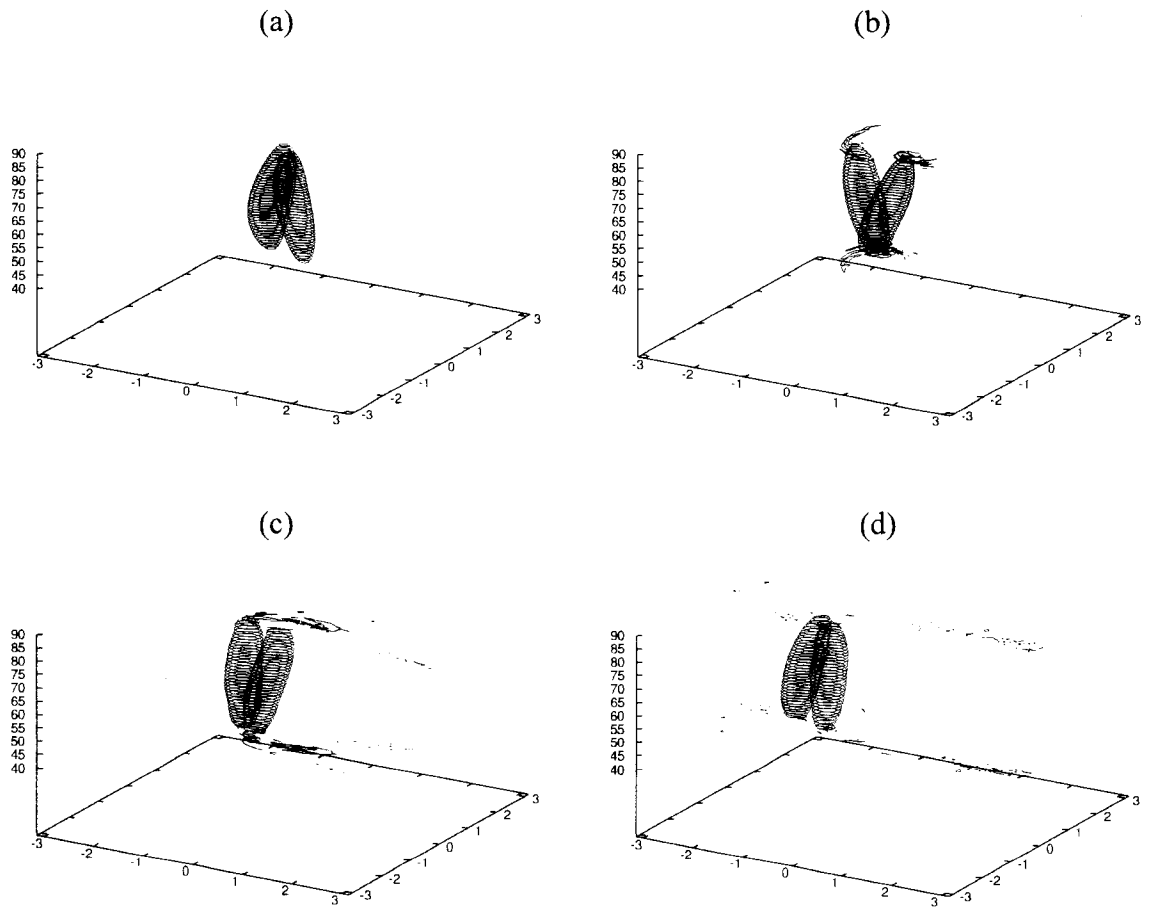

Fig. 1.37: **Time evolution of the dipole emitting filaments** (with negligible satellites): case (3), $(a, h) = (0.8, 0.4)$.

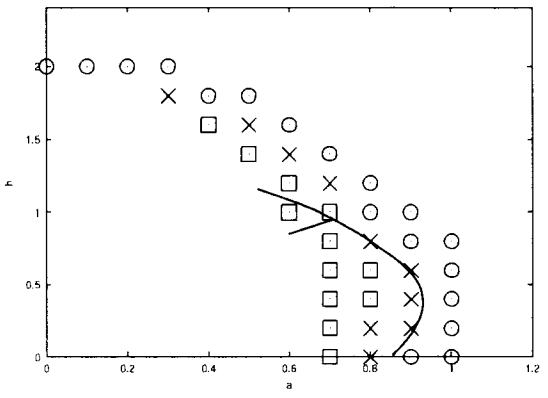

Fig. 1.38: **Pattern map of nonlinear development of counter-rotating vortices**: Open circles: stable translation; Crosses: dissipative dancing; Squares: dissipative dancing with satellites.

negative y direction with large precessions: $(a, h) = (0.6, 1.0)$; and (3) tilting down of both vortices (a singular case): $(a, h) = (0.8, 0.4)$.

In case (1), both vortices precess slightly, retaining the ellipsoidal forms, and the energy and enstrophy are conserved. In cases (2) and (3), the vortices tilt largely in the early stage of computation. Later, the vortices emit filaments from the top and bottom and the inclination angles decrease after filamentation (dancing). In case (2), many small 'satellites' remain after the vigorous filamentation. Similarly, filaments are emitted in case (3), but the remaining 'satellites' are negligibly small and almost dissipated later. The singular behavior predicted by the ellipsoidal moment model is not observed; it appears to be circumvented via the dissipative filamentation. In Fig.1.38, the nonlinear behavior is summarized as a pattern map in the (a, h) plane. Open circles show the cases of stable translation without dissipation, and crosses represent the cases of vortex-dancing with considerable filamentation. Squares represent the cases in which many satellites remain after filamentation. The solid lines are thresholds predicted by the ellipsoidal moment model (see the previous subsection). The dotted line shows the region within which the vortices initially overlap. We can see that practically, the model works well if the vortices are not off-setted vertically ($h < 1$), for it captures the dissipative processes by giving alarms; i.e., by showing infinite stretching or large precession of one or both of the contour-rotating vortices. When the vortices are largely off-setted ($h > 1$), non-ellipsoidal deformation becomes important, even if the ellipsoidal moment model predicts no singular behavior.

Figure 1.39 plots the time evolution of the translational velocity of the vorticity center. Here the thin broken line depicts the values computed by the ellipsoidal moment model and the pluses (thick line) show the results of the CASL-computation. Agreement is fairly good. The difference in the oscillation amplitude is due to the non-dissipative deviations of the vortices from ellipsoids observed in the CASL-computations. The small difference of the oscillation frequency may also be attributed to this. The model prediction is satisfactory only in the case (1). This is because many filaments are emitted in cases (2) and (3), and each vortex loses considerable enstrophy. It is of interest to investigate whether the energy dissipation is correlated to the enstrophy dissipation. It is, however, difficult to obtain conclusive findings from the present simulations, in which the observed energy dissipation is rather small (though almost within the limit of 3% computational

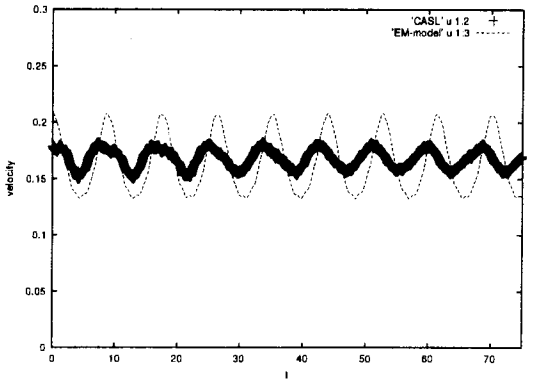

Fig. 1.39: **Translation velocity of the stable dipole** of case (1): $(a, h) = (1.2, 0.6)$. Thin broken line: ellipsoidal moment model; Thick line (pluses): CASL-computation

accuracy). This tendency is similar to that observed in the filamentation of an unstable tilted spheroid. Note that the dipoles never translate in the negative direction in the present CASL-computations.

We have investigated the interaction of two counter-rotating vortices of the same strength (vortex dipole) based on the ellipsoidal moment model, which was extracted from the partial differential equations governing the dynamics of quasi-geostrophic fluid motion. Direct numerical simulations (CASL) have been performed in order to assess the validity (limitations) of the model's predictions.

The ellipsoidal moment model indicates that one of or both vortices are stretched infinitely when they are initially placed within a certain critical distance. This is a serious drawback of the model; the computation based on the model stops whenever this phenomenon occurs. We have derived an asymptotic solution of the ellipsoidal moment model equation in the limit of very slender vortices, which corresponds to the catastrophic behavior and supports the results of numerical integrations of the model equations.

According to the CASL simulations, a dipole vigorously emits filaments near the region where the ellipsoidal moment model predicts singular behavior (small off-set). No really catastrophic behavior has been observed in the CASL simulations. The dipole structure remains robust, even if the two counter-rotating vortices are initially almost in touch. The critical distance of the model does not coincide sharply with the results of the CASL simulations for largely off-setted cases. After dissipative processes, many 'satellites' remain in (and around) the parameter region in which the ellipsoidal model predicts the occurrence of large precessions. Thus, the ellipsoidal moment model, by giving 'alarms' (i.e., the infinite stretching of one of (or both of) the contour-rotating vortices), captures only the tendency of the occurrence of dissipative events. The model needs refinements such as those proposed by Dritschel and his group (McKiver and Dritschel, 2003), in which an ellipsoid is represented by seven point vortices, not by a single point vortex as it is in the ellipsoidal moment model. According to their model computations, only doubly periodic motions have been observed in the symmetric case B (private communication).

Enstrophy is dissipated during the filamentation and the satellite-production processes. The energy dissipation is so small that it is masked by numerical errors, and we could not find out any correlation between the energy and enstrophy dissipations. It should, however, be kept in mind that many satellites result after dipole-filamentation processes, depending on the properties of the initial dipole, suggesting a new mechanism

of energy and enstrophy cascades. Due to the complex nature of the phenomena, much more extensive studies are required in order to establish a workable reset-rule after dipole interactions.

1.7 Acknowledgment

We are grateful to Professor D.G. Dritschel and his colleague for the stimulating discussion they provided on the ellipsoidal moment model and on the CASL computations. This work has been partially supported by a Grant-in-Aid for Scientific Research on Priority Areas (B) from the Ministry of Education, Science, Sports and Culture of Japan. The CASL-computations were performed on the super-computer (NEC SX-6) of the Center for Global Environmental Research (CGER), National Institute for Environmental Studies (NIES).

References

Benzi, R., Colella, M., Briscolini, M. and Santangelo, P. (1992) A simple point vortex model for two-dimensional decaying turbulence, *Phys. Fluids*, **A4**: 1036–1039.

Brestov, A. L. (1979) Solitary Rossby waves. *Izv. Acad. Sci. USSR Atmos. Oceanic Phys.*, **15**: 648–654.

Carnevale, G.F., McWilliams, J.C., Pomeau, Y., Weiss, J.B. and Young, W.R. (1991) Evolution of vortex statistics in two-dimensional turbulence, *Phys. Rev. Lett.*, **66**: 2735–2737.

Chandrasekhar, S. (1987) *Ellipsoidal figures of equilibrium* (Dover Publications, New York, 254pp.)

Charney, J.G. (1971) Geostrophic turbulence, *J. Atmos. Sci.*, **28**: 1087–1095.

Dritschel, D.G. and Ambaum, M.H.P. (1997) A contouradvective semi-Lagrangian numerical algorithm for simulating fine-scale conservative dynamical fields, *Q. J. R. Meteorol. Soc.*, **123**: 1097–1130.

Flierl, G. R. (1987) Isolated Eddy Models in Geophysics, *Annu. Rev. Fluid Mech.*, **19**: 493–530.

Hardenberg, J. and McWilliams, J.C. (2000) Vortex merging in quasi-geostrophic flows, *J. Fluid Mech.*, **412**: 331–353.

Hashimoto, H., Shimonishi, T. and Miyazaki, T. (1999) Quasigeostrophic ellipsoidal vortices in a two-dimensional strain field, *J. Phys. Soc. Jpn.*, **68**: 3863–3880.

Kida, S. (1981) Motion of an Elliptic Vortex in a Uniform Shear Flow, *J. Phys. Soc. Jpn.*, **50**: 3517–3520.

McKiver, W. and Dritschel, D.G. (2003) The motion of a fluid ellipsoid in a general linear background flow, *J. Fluid Mech.*, **474**: 147–173.

McWilliams, J.C. (1989) Statistical properties of decaying geostrophic turbulence, *J. Fluid Mechanics*, **198**: 199–230.

McWilliams, J.C., Weiss, J.B. and Yavneh, I. (1994) Anisotropy and coherent vortex structures in planetary turbulence, *Science*, **264**: 410–413.

Meacham, S.P. (1992) Quasigeostrophic, ellipsoidal vortices in a stratified fluid, *Dyn. Atmos. Oceans*, **16**: 189–223.

Meacham, S.P., Pankratov, K.K., Shchepetkin, A.F. and Zhmur, V.V. (1994) The interaction of ellipsoidal vortices with background shear flows in a stratified fluid, *Dyn. Atmos. Oceans*, **21**: 167–212.

Meacham, S.P., Morrison, P.J. and Flierl, G.R. (1997) Hamiltonian moment reduction for describing vortices in shear, *Phys. Fluids*, **9**: 2310–2328.

Melander, M., Zabusky, N.J. and Styczek, A.S. (1986) A Moment Model for Vortex Interactions of the 2D Euler Equations I. Computational Validation of a Hamiltonian Elliptical Representation, *J. Fluid Mech.*, **167**: 95–115.

Miyazaki, T., Ueno, K. and Shimonishi, T. (1999) Quasigeostrophic, tilted spheroidal vortices, *J. Phys. Soc. Jpn.*, **68**: 2592–2601.

Miyazaki, T., Shimada, M. and Takahashi, N. (2000) Quasigeostrophic wire-vortex model, *J. Phys. Soc. Jpn.*, **69**: 3233–3243.

Miyazaki, T., Furuichi, Y. and Takahashi, N. (2001) Quasigeostrophic Ellipsoidal Vortex Model, *J. Phys. Soc. Jpn.*, **70**: 1942–1953.

Miyazaki, T., Asai, A., Yamamoto, M. and Fujishima, S. (2002) Numerical Validation of Quasigeostrophic Ellipsoidal Vortex Model, *J. Phys. Soc. Jpn.*, **71**: 2687–2699.

Miyazaki, T., Yamamoto, M. and Fujishima, S. (2003) Counter-Rotating Quasigeostrophic Ellipsoidal Vortex Pair, *J. Phys. Soc. Jpn.*, **72**: 1948–1962.

Moore, D.W. and Saffman, P.G. (1971) Structure of a line vortex in an imposed strain, *Aircraft Wake Turbulence* (Olsen, J.H., Goldburg, A. and Rogers, M. eds., Plenum, 602pp.), 339–354.

Pedlosky, J. (1979) *Geophysical Fluid Dynamics* (Springer, New York, 624pp.)

Reinaud, J. N., Dritschel, D. G. and Koudella, C. R. (2003) The shape of vortices in quasi-geostrophic turbulence, *J. Fluid Mech.*, **474**: 175–191.

Chapter 2
Heat, Mass and Passive Scalar Transfer in Stratified Rotating Turbulence

2.1 Unsteady Stably Stratified Turbulence

2.1.1 Introduction

The transport of mass and heat in the atmosphere and ocean depends critically on how turbulence is affected by the presence of the stable density gradients in these flows. Recent laboratory experiments and numerical simulations on the unsteady turbulence in uniformly stratified fluid have shown how these effects are quite complex even without mean shear. Since the effects of stratification obviously affect the vertical transfer of both the dynamical scalars such as heat or density, and the passive scalars such as the concentrations of a pollutant, the most controversial and unresolved problem has been the qualitative and quantitative explanation of the counter-gradient transport of dynamical and passive scalars, which means that the heat and mass are transported by turbulent flux against the stratification. This phenomenon is sometimes observed as a net time-averaged effect (e.g., Komori, Ueda, Ogino & Mizushina, 1983), though more often only as a weak transient effect (e.g., Itsweire, Helland & Van Atta, 1986; Lienhard & Van Atta, 1990; Yoon & Warhaft, 1990). Similar effects have been noted in several numerical simulations such as that of Gerz & Yamazaki (1993). With little theoretical justification, this mechanism has hitherto been explained by the nonlinear, oscillatory turbulent 'mixing' of fluid. However, any theoretical explanations of the phenomena should clarify in what respects the phenomenon is nonlinear, and in what respects it is linear; a fuller knowledge of the linear effect should be the starting point of the study of nonlinear phenomena.

In this study we examined linear mechanisms for stratification effects and for the counter-gradient flux in particular. We applied linear rapid distortion theory (RDT) to unsheared stratified turbulence and obtained the analytical form of the three-dimensional spectrum functions, In an attempt to understand the differences in the time-dependent spectral behavior of the low ($Pr < 1$) and high ($Pr > 1$) Prandtl number flows, we applied linear rapid distortion theory (RDT) to unsheared stratified turbulence and obtained the analytical form of the three-dimensional spectrum functions. We show the special character of turbulence when $Pr = 1$, which, surprisingly, is in many respects similar to that of a non-diffusive fluid. We also consider the effects of the initial conditions, particularly the effect of the initial turbulent kinetic/potential energy, and their spectral form. These calculations extend those of Hunt, Stretch & Britter (1988) by obtaining the results in analytical form, from which several new insights emerge. We note that the dependence on Pr is different in one-dimensional spectra and three-dimensional spectra near $Pr = 1$. This difference is important, given that only the one-dimensional spectra are measured in experiments. We also consider those long-time asymptotics of the covariances that change with time very slowly or not at all, as explained by Townsend (1976) and Hunt & Carruthers (1990), these particular asymptotic results of linear theories are often applicable to steady state turbulent flows such as those in atmospheric and oceanic stratified turbulence. We have compared our theoretical results with those of recent experiments and direct numerical simulations (hereafter denoted as DNS). The comparison of results of our theory with those of the experiments and DNS helps to clarify which phenomena are truly linear and which nonlinear in these flows.

2.1.2 RDT equations

We consider a homogeneous unsheared turbulent flow placed in a uniform density gradient ($d\overline{\rho}/dx_3$) in the x_3-direction, which is anti-parallel to the gravitational acceleration. The governing equations by rapid distortion theory (RDT) (Townsend, 1976) in the frame of reference moving with the uniform mean flow are

$$\left(\frac{d}{dt} + \nu k^2\right)\hat{u}_i = \left(\frac{k_i k_3}{k^2} - \delta_{i3}\right)\hat{\rho}, \tag{2.1}$$

and

$$\left(\frac{d}{dt} + \kappa k^2\right)\hat{\rho} = N^2 \hat{u}_3, \tag{2.2}$$

where N is the Brunt-Väisälä frequency given by $N^2 = -(g/\rho_0)(d\overline{\rho}/dx_3)$, and the Fourier coefficients $\hat{u}_i (i = 1, 2, 3)$ and $\hat{\rho}$ are defined in terms of the velocity and density fluctuation by

$$u_i = \sum_{\boldsymbol{k}} \hat{u}_i(\boldsymbol{k}, t) e^{i\boldsymbol{k}\boldsymbol{x}}, \tag{2.3}$$

and

$$\frac{g}{\rho_0}\rho = \sum_{\boldsymbol{k}} \hat{\rho}(\boldsymbol{k}, t) e^{i\boldsymbol{k}\boldsymbol{x}}. \tag{2.4}$$

Here, ρ_0 is the reference density, g is the acceleration due to gravity, ρ is the density perturbation from $\overline{\rho}(x_3)$, ν is the viscosity coefficient, and κ is the diffusion coefficient. When there is no shear, the wavenumber does not change with time , i.e.

$$\frac{dk_i}{dt} = 0. \tag{2.5}$$

and it greatly simplifies the analysis.

In the nondimensionalized form of the governing equations (2.1),(2.2), there are three nondimensional parameters, i.e., the Prandtl number $Pr = \nu/\kappa$, the Reynolds number of the turbulence $Re = UL/\nu$, and the Froude number $Fr = U/NL$ (e.g., Riley, Metcalfe & Weissman, 1981). While the Prandtl number is a constant of the fluid, Re and Fr are defined by the local turbulence parameters, i.e., the integral length scale L, and the r.m.s. velocity U, which is determined by the large scale eddies. The relative effects of viscous stresses and stable stratification on different sizes (l) of the eddies, whose velocities are $u(l)$, are characterized by 'eddy' Reynolds and Froude numbers defined as $Re_l = u(l)l/\nu$ and $Fr_l = u(l)/Nl$.

However, for characterising the overall features of laboratory experiments where the length scale and r.m.s. turbulence velocity vary with time (in the moving frame), it is conventional to use the 'mean flow' Froude number $\overline{Fr} = \overline{U}/NL_0$ and the mean flow Reynolds number $\overline{Re} = \overline{U}L_0/\nu$, where $\overline{U}$ is the mean velocity and L_0 is the grid size often denoted by M. Given that in most experiments $U \sim 10^{-2}\overline{U}$, it follows that $\overline{Fr} \gg Fr$.

2.1.3 Inviscid fluid

Calculation for spectra

We first consider the inviscid fluid. By assuming $\nu = \kappa = 0$ in (2.1)-(2.5), we obtain $\hat{u}_i$ $(i = 1, 2, 3)$ and $\hat{\rho}$ as

$$\hat{\rho} = \hat{\rho}_0 \cos at + \frac{N^2}{a}\hat{u}_{30} \sin at. \tag{2.6}$$

$$\hat{u}_1 = \hat{u}_{10} + \frac{k_1 k_3}{k^2}\left\{\frac{\hat{\rho}_0}{a}\sin at - \frac{N^2}{a^2}\hat{u}_{30}(\cos at - 1)\right\}, \tag{2.7}$$

$$\hat{u}_2 = \hat{u}_{20} + \frac{k_2 k_3}{k^2}\left\{\frac{\hat{\rho}_0}{a}\sin at - \frac{N^2}{a^2}\hat{u}_{30}(\cos at - 1)\right\}, \tag{2.8}$$

$$\hat{u}_3 = \frac{1}{N^2}\frac{d\hat{\rho}}{dt} = \hat{u}_{30}\cos at - \frac{a}{N^2}\hat{\rho}_0 \sin at, \tag{2.9}$$

where

$$a = \frac{\sqrt{k_1^2 + k_2^2}}{k}N, \tag{2.10}$$

and the subscript 0 denotes the initial values. Then we can calculate all the three-dimensional spectrum functions. The result, for example, is

$$\begin{aligned}\Phi_{\rho 3}(\vec{k}, t) &= \frac{1}{2}\overline{\hat{\rho}^* \hat{u}_3 + \hat{\rho}\hat{u}_3^*} \\ &= \left\{-\frac{a}{2N^2}\Phi_{\rho\rho}(\vec{k}, 0) + \frac{N^2}{2a}\Phi_{33}(\vec{k}, 0)\right\}\sin 2at,\end{aligned} \tag{2.11}$$

where an overbar denotes the ensemble average.

In this study we assume the initial density fluxes to be zero - i.e.,

$$\Phi_{\rho i}(\vec{k}, 0) = 0 \ (i = 1, 2, 3), \tag{2.12}$$

- as in the previous numerical simulations. The effects of non-zero $\Phi_{\rho i}(\vec{k}, 0) = 0$ $(i = 1, 2, 3)$ could be assessed by exactly following the method described hereafter.

If, in addition, we assume that the initial velocity and density perturbations are both isotropic, the initial conditions are given by

$$\Phi_{ij}(\vec{k}, 0) = \frac{E(k)}{4\pi k^2}\left(\delta_{ij} - \frac{k_i k_j}{k^2}\right), \tag{2.13}$$

and

$$\Phi_{\rho\rho}(\vec{k}, 0) = \frac{S(k)}{4\pi k^2}2N^2. \tag{2.14}$$

Here

$$KE_0 = \int_0^\infty E(k)dk, \tag{2.15}$$

and

$$PE_0 = \frac{1}{2N^2}\int \Phi_{\rho\rho}(\vec{k}, 0)d\vec{k} = \int_0^\infty S(k)dk, \tag{2.16}$$

are the initial turbulent kinetic and the potential energy, respectively.

We now write the wavenumber vector in spherical coordinates as

$$\begin{aligned}k_1 &= k\sin\theta\cos\phi, \\ k_2 &= k\sin\theta\sin\phi, \\ k_3 &= k\cos\theta,\end{aligned} \tag{2.17}$$

so that

$$k^2 = k_1^2 + k_2^2 + k_3^2, \tag{2.18}$$

and

$$\sin\theta = \frac{(k_1^2 + k_2^2)^{\frac{1}{2}}}{k} = \frac{k_H}{k}, \tag{2.19}$$

where k_H is the horizontal wave number.

Variances and covariances

Substituting (2.13) and (2.14) into (2.11), we obtain the vertical flux of density as

$$\begin{aligned}\overline{\rho u_3}(t) &= \int \Phi_{\rho 3}(\vec{k},t)2\pi k^2 dk \sin\theta d\theta \\ &= \frac{N}{4}E_0^{(C)}\int_0^{\pi} d\theta \sin^2\theta \sin(2Nt\sin\theta),\end{aligned} \tag{2.20}$$

where $E_0^{(C)} = KE_0 - 2PE_0$ is the complementary energy. Other variances and covariances can be calculated similarly; examples are plotted in Figure 2.1 for the two initial conditions PE_0/KE_0=0 and 1/3. The latter is the case in which the potential energy is equal to the vertical kinetic energy (cf. Figure 3 of Hunt, Stretch & Britter, 1988). Note here that, as for inviscid unstratified shear flow (Townsend, 1976), all these functions depend only on the total initial kinetic turbulence energy and the potential turbulence energy (KE_0 and PE_0) and not on the precise form of the initial kinetic and potential energy spectra, $E(k)$ or $S(k)$, respectively. We also note that, as expected for a linear analysis, the oscillation periods of these functions are completely independent of the initial turbulent energy and depend only on the value of N. Accordingly, the zeros of $\overline{\rho u_3}(t)$ are determined only by an integral that contains Nt. On the other hand, the oscillation amplitudes are determined by $E_0^{(C)}$. The unsteady portions of the covariances all vanish when $E_0^{(C)} = 0$. This corresponds to the initial equilibrium state of the turbulence. When $PE_0 = 0$, the value of $E_0^{(C)}$ is KE_0, where as when $PE_0 = (1/3)KE_0$, it is $(1/3)KE_0$, which leads to an amplitude that is only 1/3 as large (see figure 2.1(d)).

The long-time ($Nt \gg 1$) approximation can be obtained from (2.20), using the method of steepest descents, as

$$\overline{\rho u_3}(t) = \frac{N}{4}E_0^{(C)}\left(\frac{\pi}{Nt}\right)^{\frac{1}{2}}\sin\left(2Nt - \frac{\pi}{4}\right). \tag{2.21}$$

This analytical method shows that the time-dependent portion of (2.20) comes from near $k_3 = 0$ ($\theta = \pi/2$); that is, from the infinite vertical wavelength. This suggests that, when we consider long-term development, we have to consider the effect of the 'finite' extention of fluid that we usually encounter in laboratory experiments. Exact comparison with DNS requires consideration of the periodic boundary conditions. However, the effects are important only in the unsteady part of (2.20). Insofar as the unsteady portion decays with time, the steady portion becomes dominant in the long-term, and therefore the confinement effect is not actually significant.

It is important to note in (2.21) that, even without viscosity and nonlinearity, the oscillating portions of the variances and the covariances decay with time in proportion to $t^{-\frac{1}{2}}$. The damping of oscillation is essentially a characteristic of inviscid fluid without nonlinearity. As time proceeds ($Nt \gg 1$), the contributing region of θ becomes much more restricted, to a narrower band near $\theta = \pi/2$, and the value of the integral decays with time. We also note that the oscillation period asymptotes over a long time to $t = \pi/N$, which is the period of buoyancy oscillation.

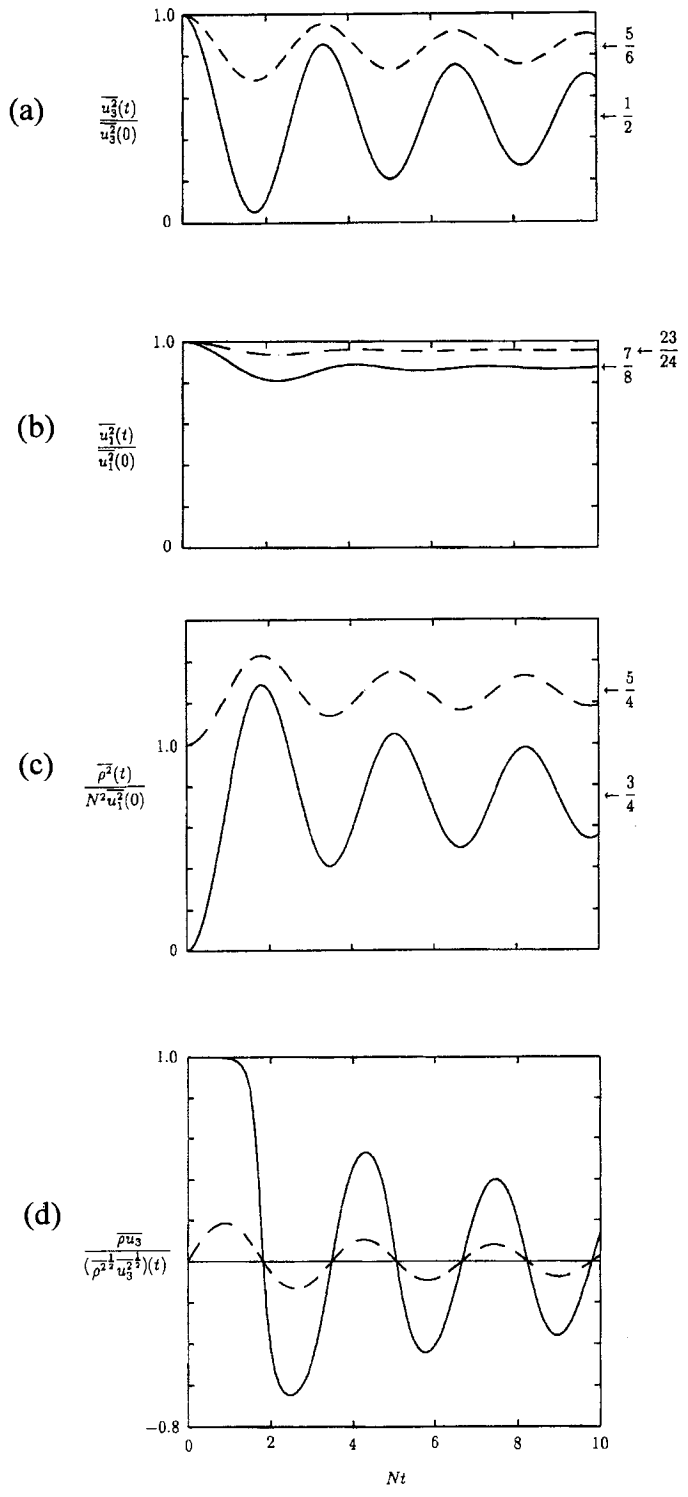

Fig. 2.1: **Time development of the covariances in inviscid fluid by RDT.** Solid lines show the results for $PE_0 = 0$, dashed lines show the results for $PE_0 = (1/3)KE_0$. The arrows show the values in the long-time limit. (a)$\overline{u_3^2}(t)/\overline{u_3^2}(0)$; (b)$\overline{u_1^2}(t)/\overline{u_1^2}(0)$; (c)$\overline{\rho^2}(t)/N^2\overline{u_1^2}(0)$; (d)$\overline{\rho u_3}/(\overline{\rho^2}^{\frac{1}{2}}\overline{u_3^2}^{\frac{1}{2}})(t)$.

2.1.4 Effects of viscosity and diffusion

Spectra

We next consider the same problem with viscosity and diffusion. The solution of (2.1)-(2.5) gives $\hat{u}_i$ $(i = 1, 2, 3)$ and $\hat{\rho}$ as

$$\hat{\rho} = Ae^{q_1 t} + Be^{q_2 t}, \tag{2.22}$$

$$\hat{u}_1 = e^{-\nu k^2 t}\left[\hat{u}_{10} + \frac{k_1 k_3}{k^2}\left\{\frac{A}{q_1+\nu k^2}\left(e^{(q_1+\nu k^2)t}-1\right) + \frac{B}{q_2+\nu k^2}\left(e^{(q_2+\nu k^2)t}-1\right)\right\}\right], \tag{2.23}$$

$$\hat{u}_2 = e^{-\nu k^2 t}\left[\hat{u}_{20} + \frac{k_2 k_3}{k^2}\left\{\frac{A}{q_1+\nu k^2}\left(e^{(q_1+\nu k^2)t}-1\right) + \frac{B}{q_2+\nu k^2}\left(e^{(q_2+\nu k^2)t}-1\right)\right\}\right], \tag{2.24}$$

$$\hat{u}_3 = \frac{1}{N^2}\left\{(q_1+\kappa k^2)Ae^{q_1 t} + (q_2+\kappa k^2)Be^{q_2 t}\right\}, \tag{2.25}$$

where

$$q_1 = \frac{1}{2}\left\{-(\nu+\kappa)k^2 + \sqrt{(\nu-\kappa)^2 k^4 - 4a^2}\right\}, \tag{2.26}$$

$$q_2 = \frac{1}{2}\left\{-(\nu+\kappa)k^2 - \sqrt{(\nu-\kappa)^2 k^4 - 4a^2}\right\}, \tag{2.27}$$

$$A = \frac{1}{q_2-q_1}\left\{(q_2+\kappa k^2)\hat{\rho}_0 - N^2\hat{u}_{30}\right\}, \tag{2.28}$$

$$B = \frac{1}{q_1-q_2}\left\{(q_1+\kappa k^2)\hat{\rho}_0 - N^2\hat{u}_{30}\right\}, \tag{2.29}$$

and a is given by (2.10).

The density-vertical velocity cospectrum then becomes

$$\begin{aligned}\Phi_{\rho 3}(\vec{k},t) &= \frac{1}{2}\overline{\hat{\rho}^*\hat{u}_3 + \hat{\rho}\hat{u}_3^*} \\ &= \frac{1}{\alpha^2}\Big[\sin^2\theta\{-(\nu-\kappa)k^2(1-\cos\alpha t) - \alpha\sin\alpha t\}\Phi_{\rho\rho}(\vec{k},0) \\ &\quad + N^2\{-(\nu-\kappa)k^2(1-\cos\alpha t) + \alpha\sin\alpha t\}\Phi_{33}(\vec{k},0)\Big]e^{-(\nu+\kappa)k^2 t},\end{aligned} \tag{2.30}$$

where

$$\alpha = \sqrt{4N^2\sin^2\theta - (\nu-\kappa)^2 k^4}. \tag{2.31}$$

Variances and covariances

From (2.30), the vertical density flux (assuming that the initial turbulence is isotropic) is given in terms of the initial spectrum as:

$$\begin{aligned}\overline{\rho u_3}(t) &= \frac{N^2}{2}\int_0^\infty dk e^{-(\nu+\kappa)k^2 t}\int_0^\pi d\theta\frac{\sin^3\theta}{\alpha^2} \\ &\quad \times\left[-(\nu-\kappa)k^2(1-\cos\alpha t)\left(E(k)+2S(k)\right) + \alpha\sin\alpha t\left(E(k)-2S(k)\right)\right].\end{aligned} \tag{2.32}$$

Other covariances can be calculated similarly, and we obtain the normalized vertical density flux by $\overline{\rho u_3}/(\overline{\rho^2}^{\frac{1}{2}}\overline{u_3^2}^{\frac{1}{2}})(t)$.

The one-dimensional spectrum in the x-direction corresponding to (2.30) can be calculated as

$$\begin{aligned}\Theta_{\rho 3}(k_1,t) &= \int_0^\infty r dr \int_0^{2\pi} d\varphi \Phi_{\rho 3}(\vec{k},t) \\ &= \int_0^\infty dr \frac{N^2}{4\pi\left(k_1^2+r^2\right)^2} e^{-(\nu+\kappa)\left(k_1^2+r^2\right)t} \int_0^{2\pi} d\varphi \frac{k_1^2+r^2\cos^2\varphi}{\alpha^2} \\ &\quad \times \left[-(\nu-\kappa)\left(k_1^2+r^2\right)(1-\cos\alpha t)\left(E\left(\sqrt{k_1^2+r^2}\right)+2S\left(\sqrt{k_1^2+r^2}\right)\right)\right. \\ &\quad \left.+\alpha\sin\alpha t\left(E\left(\sqrt{k_1^2+r^2}\right)-2S\left(\sqrt{k_1^2+r^2}\right)\right)\right], \qquad (2.33)\end{aligned}$$

with

$$\alpha = \left(\frac{4N^2\left(k_1^2+r^2\cos^2\varphi\right)-(\nu-\kappa)^2\left(k_1^2+r^2\right)^3}{k_1^2+r^2}\right)^{\frac{1}{2}}, \qquad (2.34)$$

where (r,φ) denotes cylindrical coordinates, k_1 is the wavenumber in the x-direction, r is the radial distance from the x axis, and φ is the azimuthal angle measured around the x axis.

An important character of the three-dimensional spectral function (2.30) is that when $Pr > 1$ (so that $\nu - \kappa > 0$), the viscous and diffusive effects act to induce the countergradient flux at high wavenumber k because of the term containing $-(\nu-\kappa)k^2$. On the other hand, when $Pr < 1$ (i.e., $\nu - \kappa < 0$), the viscous and diffusive effects act to prevent the countergradient flux at a high wave number. The covariance $\overline{\rho u_3}(t)$ given by (2.32) has the same characteristic. This explains why the water tank experiments for $Pr > 1$ ($Pr = 6$ (thermal stratification) and for $Pr = 600$ (salt stratification) (e.g., Itsweire, Helland & Van Atta, 1986; Komori & Nagata, 1996) often show a stronger countergradient flux than do the wind tunnel experiments ($Pr = 0.7 < 1$) (e.g., Lienhard & Van Atta, 1990). Using DNS, Gerz & Yamazaki (1993) found in their three-dimensional spectra a persistent countergradient flux at high wave number when $Pr = 2$, but did not observe it when $Pr = 1$ (see their Figure 14). When $Pr = 1$, α becomes simply $\alpha = 2N\sin\theta$ and (2.32) oscillates like $\sin(2Nt\sin\theta)$.

To see the special character of the turbulence when $Pr = 1$ (i.e., $\nu - \kappa = 0$), we write the covariances in this case explicitly; for example,

$$\overline{\rho u_3}(t) = \frac{N}{4}\int_0^\infty dk\,(E(k)-2S(k))\,e^{-2\nu k^2 t}\int_0^\pi d\theta\sin^2\theta\sin(2Nt\sin\theta). \qquad (2.35)$$

The oscillation periods of the covariances are independent of the initial conditions $E(k)$ and $S(k)$. They do not even depend on KE_0 and PE_0. They are determined only by integrals such as

$$\int_0^\pi d\theta\sin^2\theta\sin(2Nt\sin\theta), \qquad (2.36)$$

which are identical to those that determine the time development of the inviscid flux (2.20). Many studies using DNS have focussed on the case of $Pr = 1$ (e.g., Riley, Metcalfe & Weissman, 1981; Métais & Herring, 1989; Gerz & Yamazaki, 1993), but our analysis shows that this case has rather special properties.

2.1.5 Comparison with DNS and experiments

Now we compare our theory with the direct numerical simulations and laboratory experiments. In all the examples shown below, for comparison with DNS and experiments, we use an initial isotropic kinetic turbulent energy spectrum $E(k)$ that satisfies (2.15):

$$E(k) = KE_0 \left(\frac{2}{9\pi}\right)^{\frac{1}{2}} \left(\frac{2}{k_0}\right)^5 k^4 e^{-\frac{2k^2}{k_0^2}}, \tag{2.37}$$

with k_0 being the peak wave number. For the potential energy spectrum $S(k)$ we use the same form as the kinetic energy spectrum, which is given by

$$S(k) = PE_0 \left(\frac{2}{9\pi}\right)^{\frac{1}{2}} \left(\frac{2}{k_0}\right)^5 k^4 e^{-\frac{2k^2}{k_0^2}}, \tag{2.38}$$

and satisfies (2.16). These spectral forms correspond to the final period of decay of turbulence and have been used in the relevant DNS for flows without shear (Riley, Metcalfe & Weissman, 1981; Métais & Herring, 1989; Gerz & Yamazaki, 1993).

Figure 2.2a shows the time development of the normalized vertical density flux obtained by Gerz & Yamazaki (1993) for $Pr = 1$. In this example the initial kinetic energy is zero ($KE_0 = 0$) and the potential energy spectrum is given by (2.38). They showed that when the initial potential energy is large (their case B has energy 256 times larger than that of case C, and case A has energy 16 times larger than that of case C), the flux decays faster with time and the oscillation period increases for $Nt/2\pi > 1.5$. Note here that $\overline{\rho u_3}/(\overline{\rho^2}^{\frac{1}{2}}\overline{u_3^2}^{\frac{1}{2}}) = -\overline{Tu_3}/(\overline{T^2}^{\frac{1}{2}}\overline{u_3^2}^{\frac{1}{2}})$, if the perturbation temperature T is used instead of the perturbation density. Given that $Pr = 1$ and $KE_0 = 0$, the normalized fluxes obtained by RDT with viscous and diffusive effects agree with the inviscid fluxes. The RDT results do not depend on the form of $S(k)$. Because the normalized flux depends only on Nt and not on ν or κ (i.e., Re or Fr), the difference between Figure 2.2a and 2.2b comes only from the nonlinear effect. Gerz & Yamazaki (1993) argued that their case C, which has the smallest turbulence energy, shows very weak nonlinearity due to the fact that the oscillation period is approximately $Nt = \pi$. This is verified here by the almost complete agreement between their case C and the RDT results for $Nt/2\pi < 2.5$. In addition, the amplitude agrees well. Some differences for larger times (i.e., $Nt/2\pi > 2.5$) are likely to arise because DNS cannot resolve the larger scales ($k \sim 0$), the effects of which become dominant in a long-time development. We can say that the stronger decay and the increase in the period notable in cases A and B are purely nonlinear effects caused by the large turbulence energy. Gerz & Yamazaki, quoting personal communication with H.Wijesekera, argued that the majority of turbulent patches observed in the ocean correspond to their case C, although noticeable fractions of observed turbulent patches correspond to their case B. Thus, case C appears to be well representative of the natural turbulence in geophysical contexts.

Figure 2.3 shows a comparison of the normalized vertical density flux obtained by RDT with the DNS. In DNS, the turbulent Froude number satisfies $Fr < 1$ when $Nt > 2$ (Figure 7 of Métais & Herring, 1989), and the RDT would be applicable for that period. In RDT we assume the same form for $E(k)$ and $S(k)$ as that in (2.37) and (2.38), then the normalized flux agrees with the inviscid flux. The form of $E(k)$ is the same in DNS and RDT, and is given by (2.37). However, in DNS, an unstratified calculation

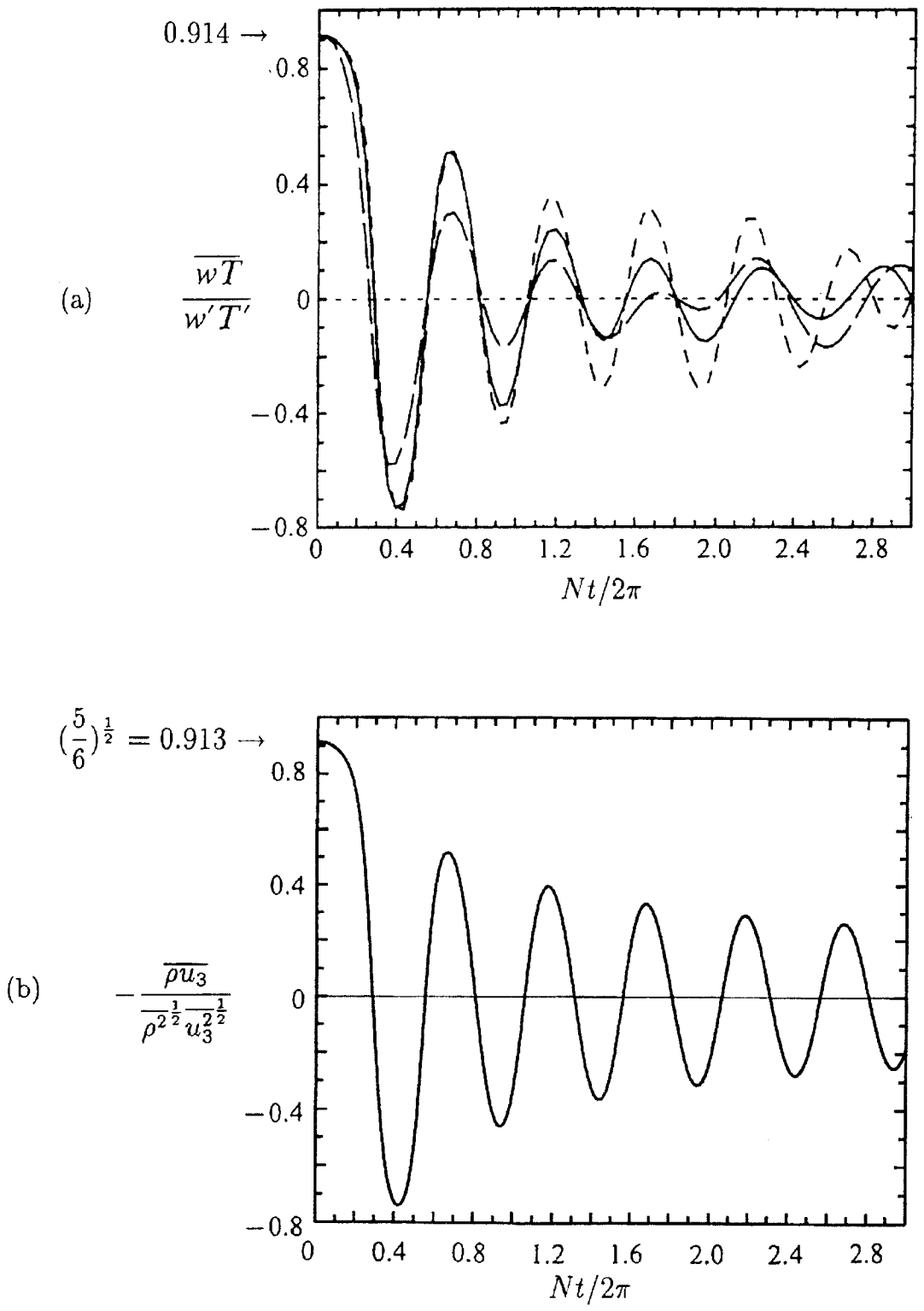

Fig. 2.2: **Time development of the normalized vertical density flux** when $Pr = 1$ and $KE_0 = 0$. (a)DNS results by Gerz & Yamazaki (1993, Figure 8): ————, case A ($PE_0 = 0.46$ in their unit); - - - - , case B ($PE_0 = 7.37$); --------, case C ($PE_0 = 0.029$). (b)RDT. In DNS, the nonlinear effect would be negligible when $Nt/2\pi > 0.48$.

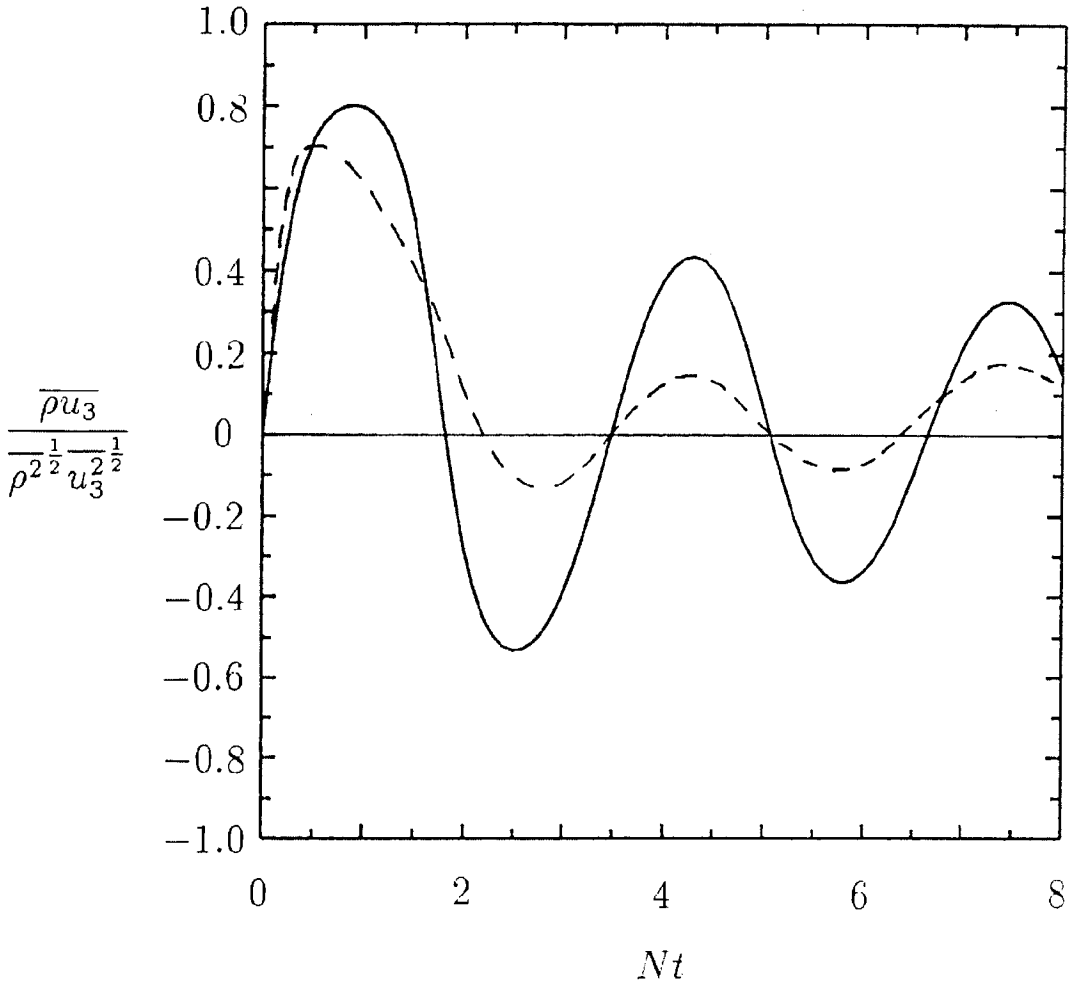

Fig. 2.3: **Time development of the normalized vertical density flux** when $Pr = 1$ and $PE_0/KE_0 = 0.05$. – – – –, DNS by Métais & Herring(1989, Figure 3); ————, RDT. In DNS, $Fr < 1$ is satisfied when $Nt > 2$.

was performed before stratification was switched on at time $t = 0.685$ to match the experimental conditions. This causes a change in the 'initial' kinetic energy spectrum and leads to the uncertainty in the initial condition necessary for the comparison with RDT results.

However, as the equation (2.35) shows, the zeros of the flux are independent of $E(k)$ and $S(k)$ when $Pr = 1$, in which case the differences between the zeros of the flux result purely from nonlinear effects. We find that the third sa and fourth zeros agree where as the second and fifth zeros show some differences. On the other hand, Figure 2.2a shows that even when the turbulence energy is very large, the zeros agree with the RDT at least for the first five zeros. This suggests that the difference of some zeros is not the effect of nonlinearity; rather, the effect of some numerical errors in DNS is a plausible explanation here.

Figure 2.4 shows the time development of the trace components of the anisotropy tensor defined by

$$b_{ij} = \frac{\overline{u_i u_j}}{\overline{u_1^2} + \overline{u_2^2} + \overline{u_3^2}} - \frac{1}{3}. \tag{2.39}$$

When $b_{ii} = 0$ $(i = 1, 2, 3)$, the turbulence is isotropic. Figure 2.4a, which is the result

of case C (small turbulence energy) of Gerz & Yamazaki (1993), agrees quantitatively with the RDT result given in Figure 2.4b. When $Pr = 1$ and $E(k) = 0$, the anisotropy tensor in RDT agrees with the inviscid result, because the integrals containing $S(k)$ are cancelled out. The trace components are

$$b_{11} = b_{22} = \frac{\frac{1}{6} - \frac{1}{4}\int_0^\pi d\theta \cos^2\theta \sin\theta \cos(2Nt\sin\theta)}{1 - \frac{1}{2}\int_0^\pi d\theta \cos^2\theta \sin\theta \cos(2Nt\sin\theta) - \frac{1}{2}\int_0^\pi d\theta \sin^3\theta \cos(2Nt\sin\theta)} - \frac{1}{3}, \tag{2.40}$$

and

$$b_{33} = \frac{\frac{2}{3} - \frac{1}{2}\int_0^\pi d\theta \sin^3\theta \cos(2Nt\sin\theta)}{1 - \frac{1}{2}\int_0^\pi d\theta \cos^2\theta \sin\theta \cos(2Nt\sin\theta) - \frac{1}{2}\int_0^\pi d\theta \sin^3\theta \cos(2Nt\sin\theta)} - \frac{1}{3}. \tag{2.41}$$

In the limit of $t \to 0$, we obtain $b_{11} = b_{22} = -7/30$, $b_{33} = 7/15$, and in the long-time limit ($t \to \infty$) we obtain $b_{11} = b_{22} = -1/6$, $b_{33} = 1/3$.

These results agree well with the DNS results by Gerz & Yamazaki (1993). A small difference in the long time could be the result of the weak nonlinearity and the effect of the periodic boundary conditions used in DNS.

Figure 2.5 shows the comparison of the normalized flux with air flow experiments by Yoon & Warhaft (1990). If we set the ratio $PE_0/KE_0 (= 0.15)$ so that the initial peak value of the normalized flux ($= 0.68$) agrees, subsequent time development agrees well. It seems that the excitation of turbulence begins earlier than $t = 0$ in the experiment. The agreement is remarkable considering the plausible difference in the initial spectral form of $E(k)$ and $S(k)$. Note the weak countergradient flux ($[-\overline{\rho u_3}/(\overline{\rho^2}^{\frac{1}{2}}\overline{u_3^2}^{\frac{1}{2}})]_{max} \sim 0.2$) in this case ($Pr < 1$) compared to those in the previous cases (Figure 2.2 and 2.3) where $Pr = 1$. The weak countergradient flux for $Pr < 1$ can be inferred from our expression of the flux (2.32) as discussed in 2.1.4.

Figure 2.6 shows the corresponding one-dimensional cospectrum $-k_1\Theta_{\rho 3}(k_1)$. In these figures, positive $-k_1\Theta_{\rho 3}(k_1)$ indicates that there is a counter-gradient flux.

In spite of the plausible difference in the initial energy spectrum forms $E(k)$ and $S(k)$, the time development is qualitatively the same for these spectra.

We see that the counter-gradient flux is retarded at high wave number, whereas it occurs faster at lower wave numbers. These results for low Prandtl number flow ($Pr < 1$) can be inferred from (2.33). In this case, there is slow development of the countergradient flux at much lower wavenumbers. We should note that the one-dimensional cospectrum (2.33) has a more complicated form than the three-dimensional cospectrum (2.30), so that this development of the countergradient flux at the lowest wave numbers is not so easily apparent, although it can be clarified from (2.33).

A further comparison with the air flow experiments by Lienhard & Van Atta (1990) (their case of $N = 2.42s^{-1}$ and mesh size $L_0 = 5.08cm$) is shown in Figure 2.7. In their experiments, countergradient flux is very weak even when it occurs. The validity of RDT is high when the turbulent Froude number Fr is small. As shown in Figure 18 of Yoon & Warhaft (1990), Fr is smaller (about 1/2) in the experiment of Yoon & Warhaft (1990) than in that of Lienhard & Van Atta (1990). Therefore, the nonlinear effect is comparatively smaller in the experiment of Yoon & Warhaft (1990). This explains why the results of experiments by Yoon & Warhaft (1990) show better agreement with those of RDT.

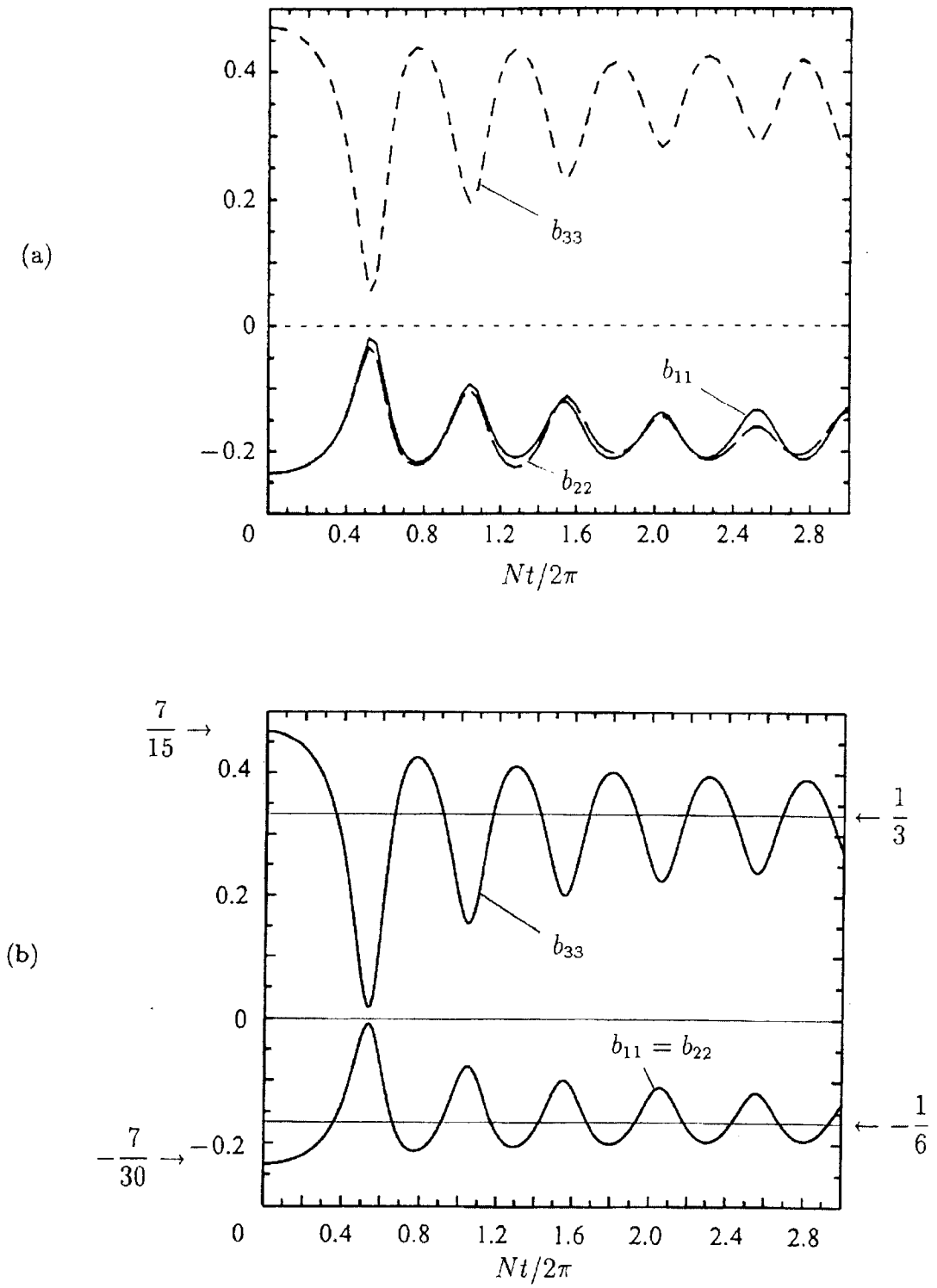

Fig. 2.4: **Time development of the trace components of the anisotropy tensor** $b_{ii}(i = 1, 2, 3)$ when $Pr = 1$ and $KE_0 = 0$. (a) DNS by Gerz & Yamazaki (1993, Figure 9(c)). (b)RDT.

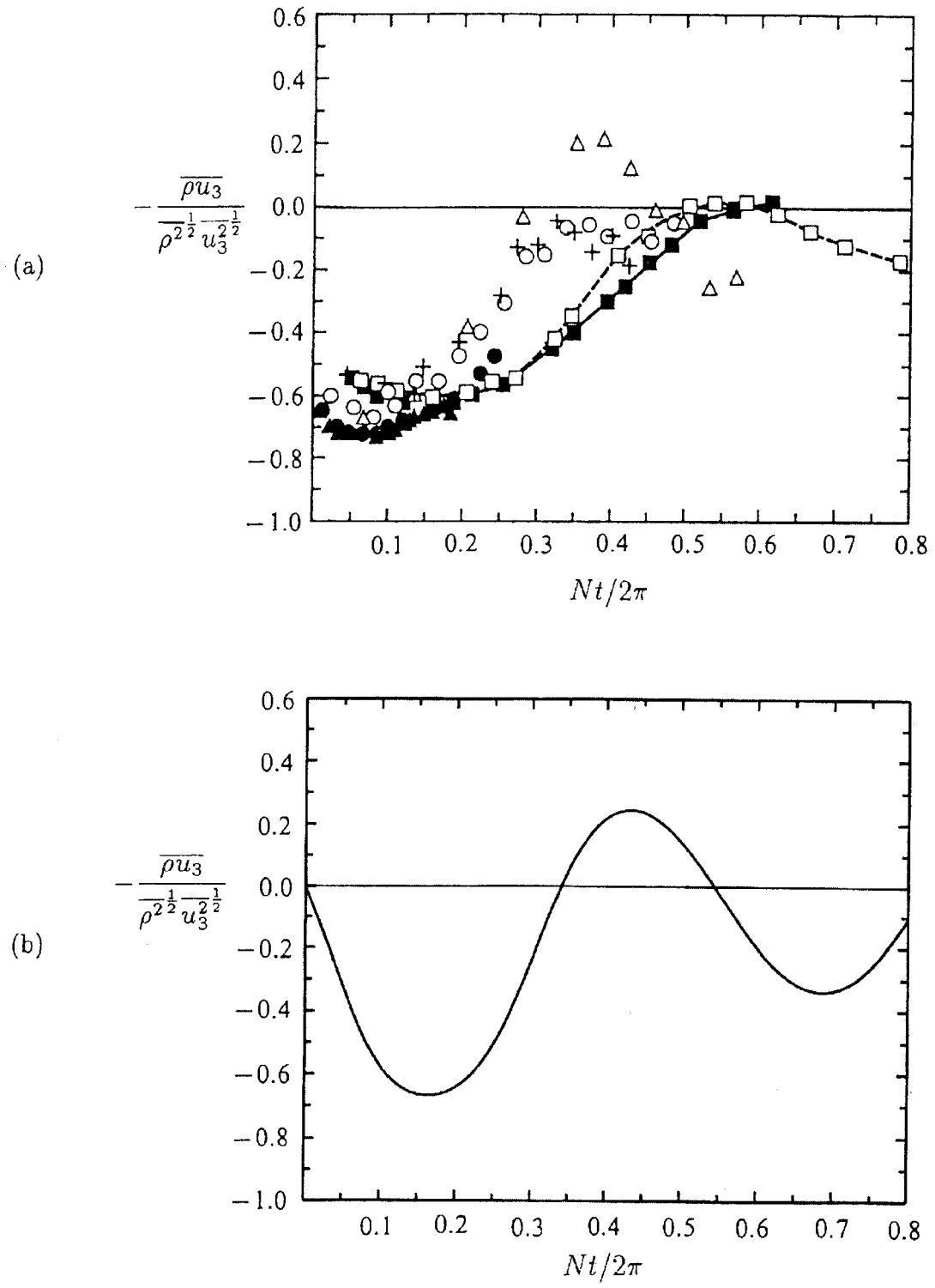

Fig. 2.5: **Time development of the normalized vertical density flux** when $Pr = 0.7$. (a) Wind tunnel experiments by Yoon & Warhaft (1990, $Fr < 1$ holds when $Nt/2\pi > 0.15$). △, $\overline{Fr} = 84.8, \overline{Re} = 4050$; ○, $\overline{Fr} = 114, \overline{Re} = 5100$; +, $\overline{Fr} = 127, \overline{Re} = 6070$; •, $\overline{Fr} = 192, \overline{Re} = 6040$; ▲, $\overline{Fr} = 253, \overline{Re} = 5670$. Wind tunnel experiments by Lienhard & Van Atta (1990, Figure 2(b), $Fr < 1$ holds when $Nt/2\pi > 0.25$); ■, $\overline{Fr} = 17.1, \overline{Re} = 7100$; ■, $\overline{Fr} = 22, \overline{Re} = 7900$. (b) RDT ($\overline{Fr} = 84.8, \overline{Re} = 4050$, $PE_0/KE_0 = 0.15$, $k_0 = 30$).

(a)

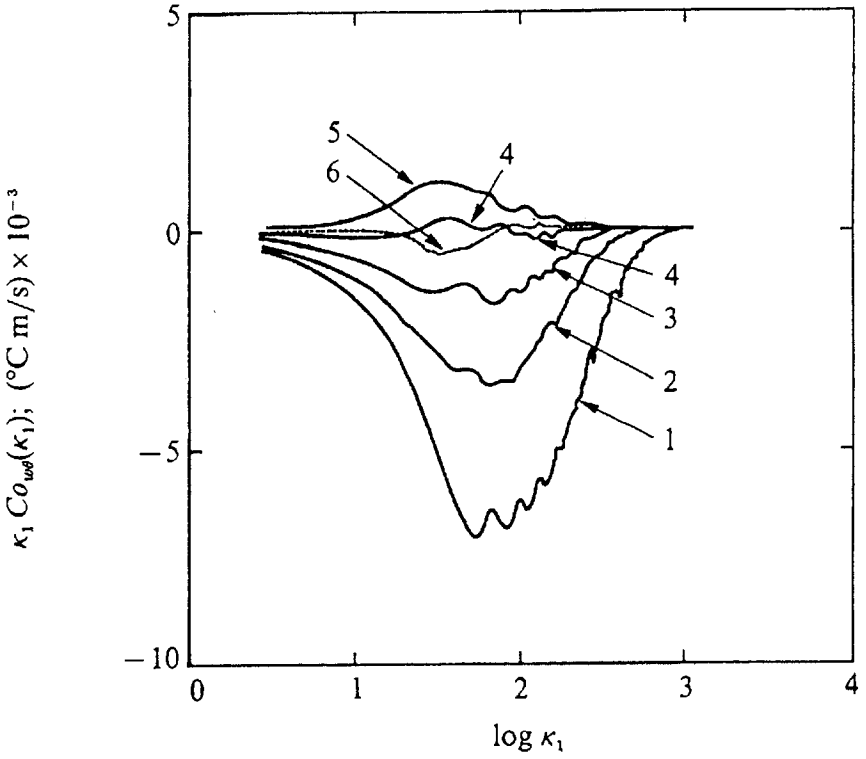

(b)

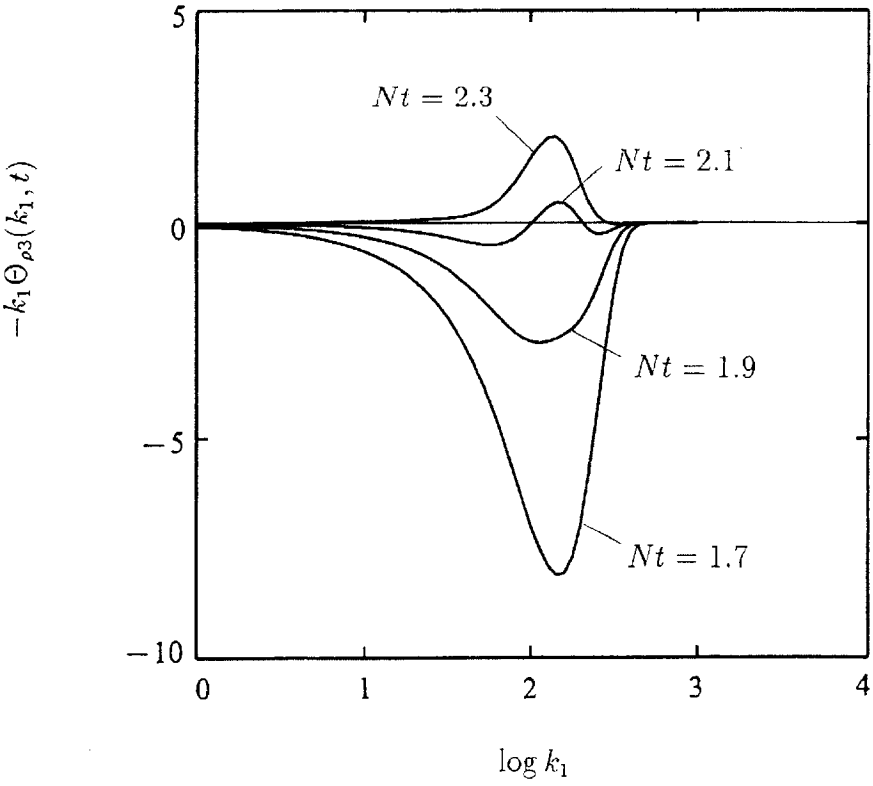

Fig. 2.6: **Time development of the one dimensional spectrum** $-k_1\Theta_{\rho 3}(k_1, t)$ corresponding to Figure 2.5 ($Pr = 0.7$, $\overline{Fr} = 84.8$, $\overline{Re} = 4050$). (a) Wind tunnel experiments by Yoon & Warhaft (1990, Figure 15(b), x: distance from the grid, M: mesh length of the grid, $Fr < 1$ holds where $x/M > 76.5$.) (1)$x/M = 36.5$; (2)76.5; (3)116.5; (4)156.5; (5)196.5; (6)236.5. (b) RDT ($PE_0/KE_0 = 0.15$, $k_0 = 30$).

(a)

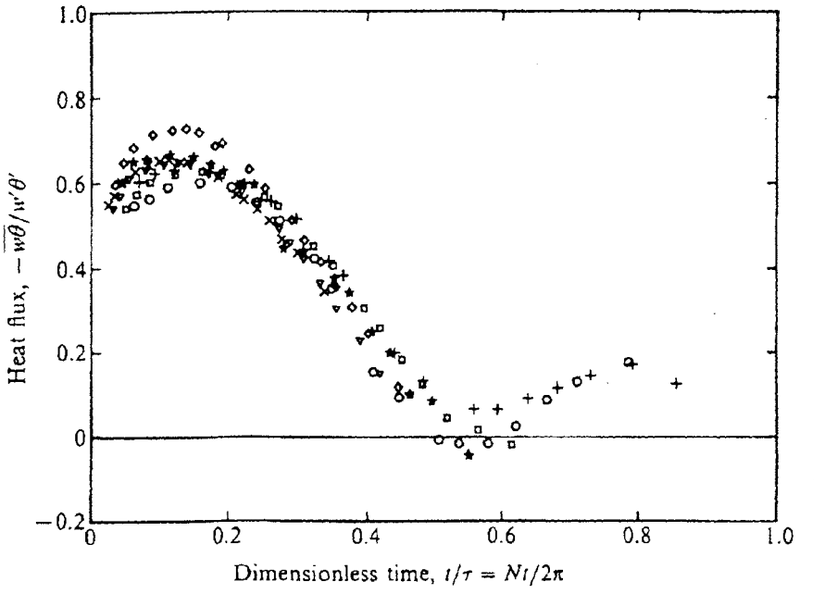

(b) $\dfrac{\overline{\rho u_3}}{\overline{\rho^2}^{\frac{1}{2}}\,\overline{u_3^2}^{\frac{1}{2}}}$

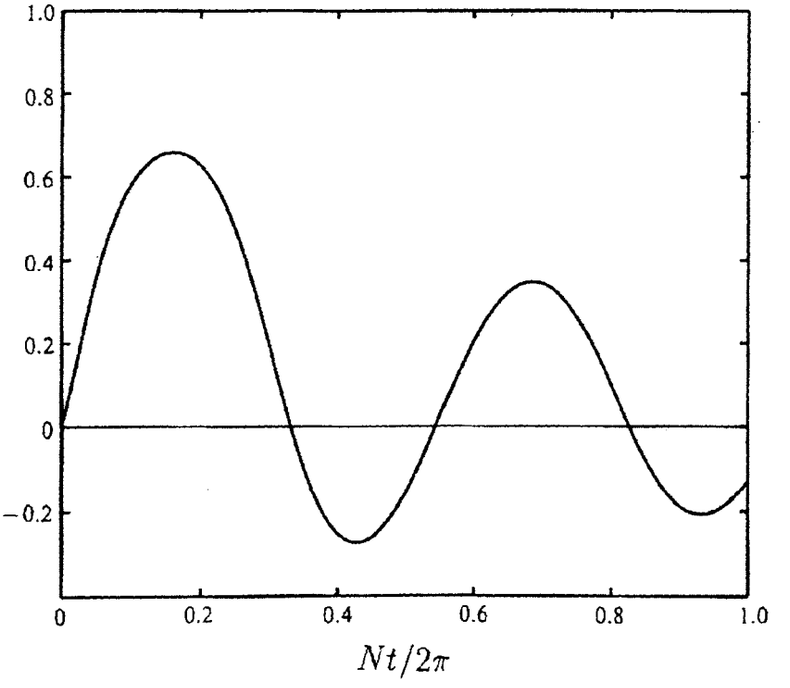

Fig. 2.7: **Time development of the normalized vertical density flux** when $Pr = 0.7$. (a)Wind tunnel experiments by Lienhard & Van Atta (1990, Figure 2(b), $Fr < 1$ holds when $Nt/2\pi > 0.25$); ○, $\overline{Fr} = 17.1, \overline{Re} = 7100$; ■, $\overline{Fr} = 22, \overline{Re} = 7900$; ▽, $\overline{Fr} = 33, \overline{Re} = 8400$; ×, $\overline{Fr} = 42, \overline{Re} = 8400$; +, $\overline{Fr} \approx 31, \overline{Re} \approx 3400$; ⋆, $\overline{Fr} = 47, \overline{Re} = 4400$; ◇, $\overline{Fr} \approx 62, \overline{Re} \approx 4200$. (b) RDT ($\overline{Fr} = 17.1$, $\overline{Re} = 7100$, $PE_0/KE_0 = 0.14$, $k_0 = 30$).

Figure 2.8 shows a comparison with the thermally stratified water experiments by Komori & Nagata (1996). Their experiments are for two-layer flow and not for a continuously stratified flow, but their one-dimensional cospectrum shows clearly the effect of the large Prandtl number ($Pr > 1$).

The comparison with RDT results shows good agreement in that the enhanced countergradient flux at high wave numbers exists. In the salt-water experiments by Itsweire, Helland & Van Atta (1986), no countergradient flux was observed at high wavenumber; Lienhard & Van Atta (1990) speculate that this might have been the result of relatively poor high wave-number resolution in their experiments.

To understand the decay of turbulence due to viscosity and diffusion, we show in Figure 2.9 the time development of the turbulence energy in the DNS of Gerz & Yamazaki (1993) (their case C; i.e., the case with the smallest turbulence energy) and the corresponding results by RDT. In this case $Pr = 1$, $E(k) = 0$ and $S(k)$ has the form of (2.38). Then, in RDT, the turbulent kinetic energy $KE(t)$ and the turbulent potential energy $PE(t)$ can be easily calculated from the integrals similar to (2.35) by setting $E(k) = 0$. Then the total turbulence energy is obtained as $TE(t) = KE(t) + PE(t)$. The results are

$$\begin{aligned} KE(t) &= \frac{1}{2}(\overline{u_1^2} + \overline{u_2^2} + \overline{u_3^2}) \\ &= \frac{1}{2}\int_0^\infty dk S(k) e^{-2\nu k^2 t} \\ &\quad \times \left(1 - \frac{1}{2}\int_0^\pi d\theta \cos^2\theta \sin\theta \cos(2Nt\sin\theta) - \frac{1}{2}\int_0^\pi d\theta \sin^3\theta \cos(2Nt\sin\theta)\right), \end{aligned} \tag{2.42}$$

$$\begin{aligned} PE(t) &= \frac{1}{2N^2}\overline{\rho^2} \\ &= \frac{1}{2}\int_0^\infty dk S(k) e^{-2\nu k^2 t}\left(\frac{1}{2} + \frac{1}{4}\int_0^\pi d\theta \sin\theta \cos(2Nt\sin\theta)\right), \end{aligned} \tag{2.43}$$

and

$$TE(t) = \int_0^\infty dk S(k) e^{-2\nu k^2 t}. \tag{2.44}$$

We can calculate this integral analytically by substituting (2.38), and find the decaying ratio as

$$\begin{aligned} \frac{TE(t)}{TE(0)} &= \frac{\int_0^\infty dk S(k) e^{-2\nu k^2 t}}{\int_0^\infty dk S(k)} \\ &= \left(\frac{1}{1 + \nu k_0^2 t}\right)^{\frac{5}{2}}. \end{aligned} \tag{2.45}$$

Using the same Reynolds number $Re = 57.4$ and the same peak wavenumber in the initial energy spectrum $k_0 = (8\pi)^{\frac{1}{2}}$ as in Gerz & Yamazaki (1993), we obtain the RDT counterpart (Figure 2.9b) of DNS results (Figure 2.9a). The comparison is good except that there is a slightly faster decay in DNS. Thus, the effective viscosity/diffusion (in this case $\nu = \kappa$) is a little larger in DNS. If the numerical viscosity is negligible in DNS, the difference comes only from the nonlinearity. This further supports the

(a)

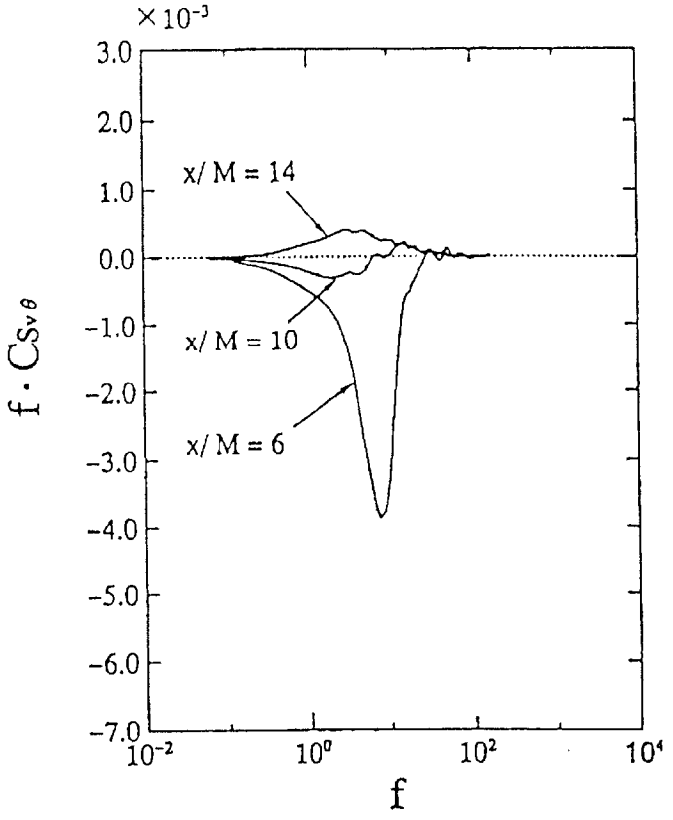

(b)

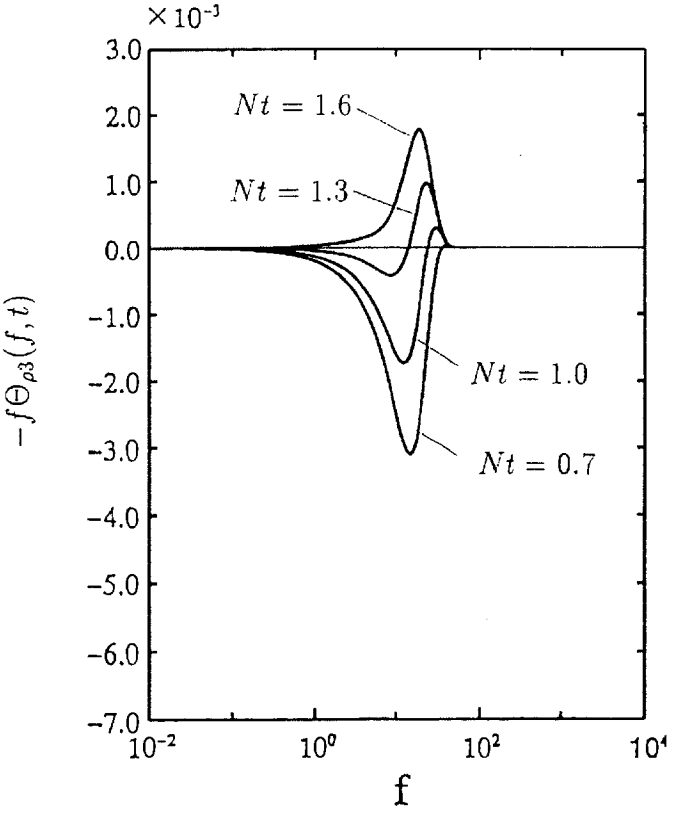

Fig. 2.8: **Time development of the one dimensional spectrum** $-f\Theta_{\rho 3}(f,t)$ ($f = k_1 U/2\pi$) near the first vanishing time of $\overline{\rho u_3}$ ($Pr = 6, \overline{Re} = 2500, \overline{Fr} = 2.86$). (a)Water tank experiments by Komori & Nagata (1996, Figure 2.9(b), x:distance from the grid, M:mesh length of the grid. $Fr < 1$ holds where $x/M > 10$). (b) RDT ($PE_0/KE_0 = 0.11$, $k_0 = 25$).

(a)

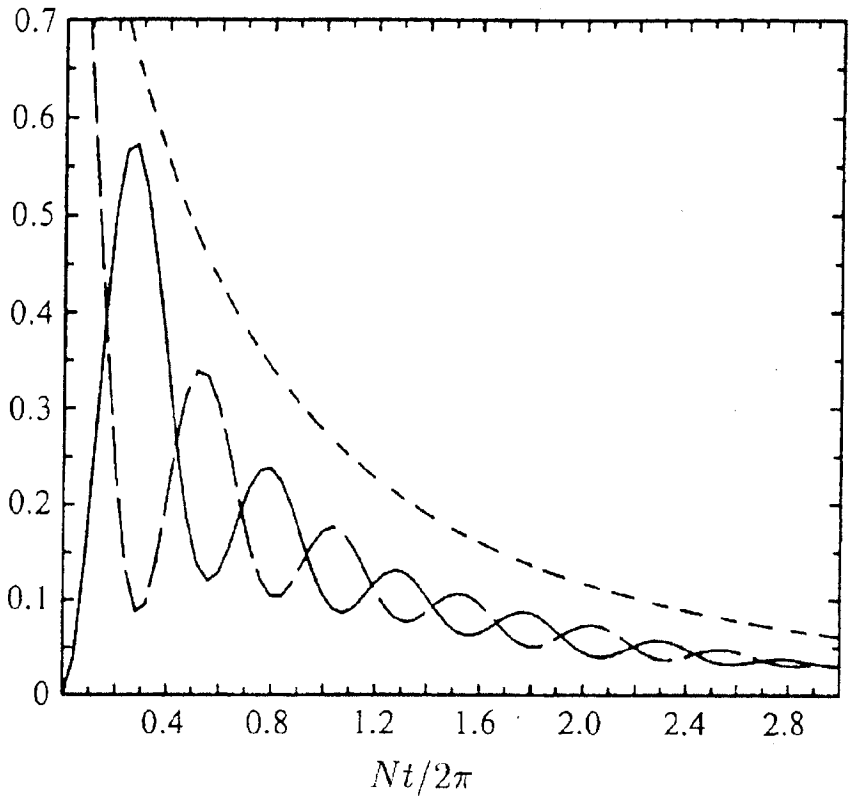

(b)

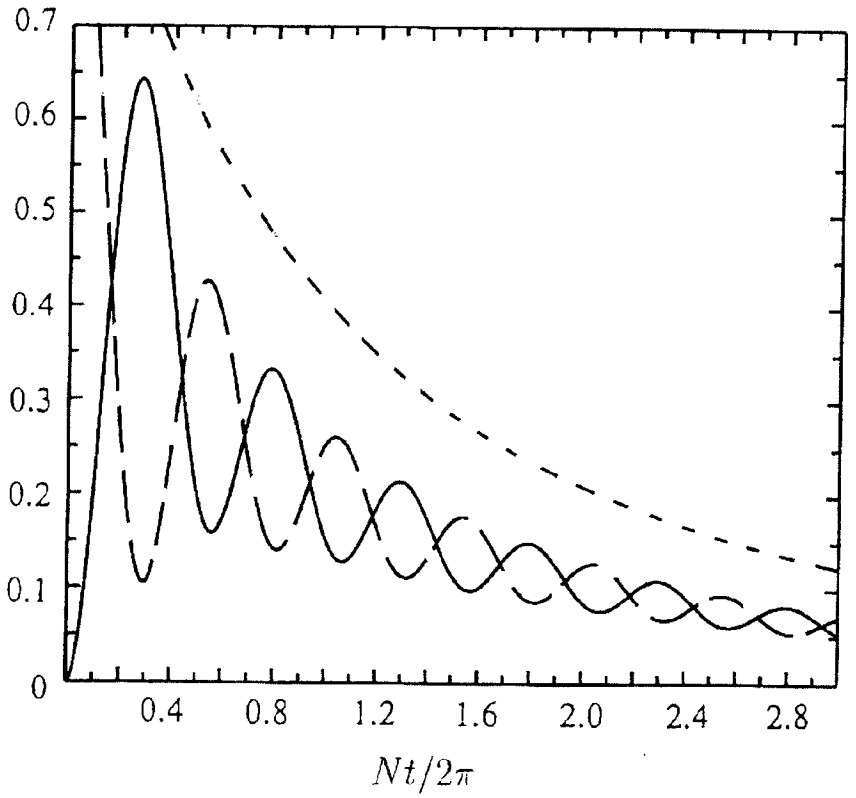

Fig. 2.9: **Time development of the kinetic, potential, and total turbulence energy** when $Pr = 1$ and $KE_0 = 0$. ——————, KE/KE_0; – – – –, PE/PE_0; --------, TE/TE_0. (a) DNS by Gerz & Yamazaki (1993, Figure 2.1(c)), (b)RDT.

conjecture that use of lower Prandtl and Reynolds numbers are appropriate to incorporate nonlinearity effects, When the nonlinearity is not large, its effect would be well described by these remedies. As we have seen in Figures 2.2 and 2.4, the non-dimensional ratio of the covariances agree excellently with RDT, even when there are some deviations in the decay rate of each covariance or the turbulent energies (Figure 2.9). This shows that the functional forms of the covariances are not affected by the nonlinearity, the only differences being in the effective value of the viscosity/diffusion coefficient or the Reynolds/Prandtl numbers.

2.1.6 Conclusions

We investigated the time development of the stratified unsheared turbulence using the rapid distortion theory (RDT). The results show that the time-dependent oscillations, including the countergradient phenomena, can largely be explained in terms of phase lags in linear oscillation rather than in terms of any new kind of nonlinear mixing processes. Our main results can be summarised as follows.

For inviscid fluid, we obtained the time-dependent covariances in explicit analytical forms and showed their short and long time limits. These limits clarified that the initial turbulent kinetic and potential energy determine the final distribution of energy among the velocity components and density perturbation. The covariances depend only on the initial total kinetic and potential energy and not on the precise form of the energy spectra. The oscillation period of the covariances, including the zeros of the vertical density flux, are completely independent of the initial condition.

For viscous/diffusive fluids, we have given the analytical form of the time-dependent three-dimensional spectral functions and expressed the corresponding one-dimensional spectra and covariances by rather simple integrals, which enable us to see the effect of the Prandtl and the Reynolds number clearly. We found that a high Prandtl number ($Pr > 1$) leads to counter-gradient flux occuring at high wave number, whereas a low Prandtl number ($Pr < 1$) inhibits the counter-gradient flux at high wave number. These characteristics explain the differences between water-tank and wind-tunnel experiments.

When $Pr = 1$, all the wave-number components in the three-dimensional spectrum function oscillate in phase, as in an inviscid fluid. Then the effects of viscosity and diffusion are limited to the damping of all the wave-number components in phase. The oscillation periods of the covariances also agree with those for an inviscid fluid and do not depend on the initial conditions (excepting the assumption of isotropy).

To estimate certain effects of nonlinearity that might dominate in high Reynolds number turbulence (c.f. Townsend, 1976), the use of an effective (eddy) viscosity and diffusion coefficient has been considered. (There are of course other effects of nonlinearity, such as modulating the frequency of the oscillation, that are not described by this approximation.) This leads the eddy Prandtl number Pr_t (see Townsend, 1976, pp. 358) and Reynolds number to be smaller than the molecular values. Applying these values in the linear theory leads to a decrease in the strength of the counter-gradient flux, and our results become closer to the moderate Reynolds number determined in laboratory experiments. We note that in atmospheric measurements of unsteady stably stratified turbulence at very high Reynolds number (where $Re \sim 10^4$ and $Fr \simeq 1$), such as those described by Nai-ping, Neff & Kaimal (1983), countergradient fluxes were observed. Significant countergradient fluxes also occur when density layers emerge in decaying turbulence.

2.2 Stably and Unstably Stratified Rotating Turbulence

2.2.1 Introduction

Although there have been many studies on turbulence focusing on stratification or rotation have been conducted, studies on stratified *and* rotating turbulence have been relatively few. Recently, Bartello (1995), Métais, Bartello, Garnier, Riley & Lesieur (1996) utilized wave/vortex decomposition in the analysis of DNS data for stratified rotating turbulence and investigated the nonlinear energy-transfer mechanisms. Bartello (1995) also investigated the time development of the kinetic and potential energy for $Pr = 1$ in decaying turbulence. More recently, Iida & Nagano (1999) and Tsujimura, Iida & Nagano (1998) investigated the same system by DNS for the case with rapid rotation.

In this section, we solve the RDT equations as analytically as possible to clarify the essential mechanisms governing the transport processes in stratified rotating turbulence. We first obtain the general analytical RDT solutions, then used them to calculate the variances and covariances such as the vertical density flux and the kinetic/potential energies for the initially isotropic and axisymmetric turbulence. Next we investigated the asymptotic behavior of those quantities and compared the results with the DNS and the experiments in order to clarify the heat/density transport mechanisms in stably stratified rotating turbulence.

2.2.2 RDT equations

We consider a homogeneous turbulent flow with vertical density stratification ($d\overline{\rho}/dx_3$) and system rotation around the vertical axis. The governing equations in the rotating frame under Boussinesq approximations are

$$\frac{\partial \boldsymbol{u}}{\partial t} + (\boldsymbol{u}\cdot\nabla)\boldsymbol{u} + 2\boldsymbol{\Omega}\times\boldsymbol{u} = -\frac{1}{\rho_0}\nabla p - g\hat{x_3}\frac{\rho}{\rho_0} + \nu\nabla^2\boldsymbol{u}, \tag{2.46}$$

$$\frac{\partial \rho}{\partial t} + (\boldsymbol{u}\cdot\nabla)\rho + u_3\frac{d\overline{\rho}}{dx_3} = \kappa\nabla^2\rho, \tag{2.47}$$

and

$$\mathrm{div}\boldsymbol{u} = 0, \tag{2.48}$$

where $\boldsymbol{u}$ is the velocity fluctuations, $\boldsymbol{\Omega} = (0, 0, \Omega)$ denotes the angular velocity Ω of the system rotation, and $\hat{x_3}$ is the unit vector in the vertical upward direction.

We linearize the above equations and introduce the spectral decompositions given by (2.3) and (2.4), then obtain the following set of ordinary differential equations (RDT equations):

$$\left(\frac{d}{dt} + \nu k^2\right)\hat{u_i} + \left(\delta_{ij} - \frac{k_i k_j}{k^2}\right)\epsilon_{j3l} f \hat{u_l} = \left(\frac{k_i k_3}{k^2} - \delta_{i3}\right)\hat{\rho}, \tag{2.49}$$

and

$$\left(\frac{d}{dt} + \kappa k^2\right)\hat{\rho} = N^2\hat{u_3}, \tag{2.50}$$

where $f = 2\Omega$ is the Coriolis parameter (twice the angular velocity Ω).

2.2.3 Inviscid fluid

We first consider the inviscid fluid with $\nu = \kappa = 0$. The RDT equations (2.49)-(2.50) give the general solutions for $\hat{u}_i(t)$ $(i = 1, 2, 3)$ and $\hat{\rho}(t)$.

Then we can calculate all the three-dimensional spectrum functions. If we again assume (2.12)–namely, the condition that the initial density fluxes are zero– the results become, for example,

$$\begin{aligned}\Phi_{\rho 3}(\vec{k}, t) &= \frac{1}{2}\overline{\hat{\rho}^* \hat{u}_3 + \hat{\rho}\hat{u}_3^*} \\ &= -\frac{k_1^2 + k_2^2}{k^2 a}\left[\cos at + \frac{f^2 k_3^2}{k^2 a^2}(1 - \cos at)\right] \sin at \Phi_{\rho\rho}(\boldsymbol{k}, 0) + \frac{N^2}{2a}\Phi_{33}(\boldsymbol{k}, 0) \sin 2at \\ &\quad + \frac{f^2 N^2 k_3^2}{a^3 k^4}\left(k_2^2 \Phi_{11}(\boldsymbol{k}, 0) + k_1^2 \Phi_{22}(\boldsymbol{k}, 0) - 2k_1 k_2 \Phi_{12}(\boldsymbol{k}, 0)\right)(1 - \cos at) \sin at \\ &\quad + \frac{f N^2 k_3}{a^2 k^2}\left(k_2 \Phi_{13}(\boldsymbol{k}, 0) - k_1 \Phi_{23}(\boldsymbol{k}, 0)\right)(\cos at - \cos 2at), \end{aligned} \tag{2.51}$$

where k denotes $|\boldsymbol{k}|$, the subscript 0 denotes the initial values, and the frequency a is defined by

$$a = \frac{(N^2(k_1^2 + k_2^2) + f^2 k_3^2)^{1/2}}{k}, \tag{2.52}$$

which shows the exact dispersion relation of the inertial gravity wave.

2.2.4 Initially isotropic turbulence

We consider the initially isotropic turbulence under stable stratification ($N^2 > 0$) whose initial conditions are again given by (2.13)-(2.16).

Integrating (2.51), we obtain the vertical density flux as

$$\begin{aligned}\overline{\rho u_3}(t) &= \int \Phi_{\rho 3}(\vec{k}, t) 2\pi k^2 dk \sin\theta d\theta \\ &= \frac{N^2}{2} E_0^{(C)} \int_0^{\pi} d\theta \frac{\sin^3\theta}{a^3} \sin at (N^2 \sin^2\theta \cos at + f^2 \cos^2\theta), \end{aligned} \tag{2.53}$$

where $E_0^{(C)} = KE_0 - 2PE_0$ is the complementary energy. Other variances and covariances can be calculated similarly.

In the case of pure rotation ($N = 0, f \neq 0$), energy distribution does not change with time and $\overline{u_1^2}(t) = \overline{u_2^2}(t) = \overline{u_3^2}(t) = \frac{2}{3}KE_0$ holds at all times.

This recovers the DNS results for initially isotropic rotating turbulence that retains the initial isotropy (Bardina, Ferziger & Rogallo 1985) and the results by linear theory (Greenspan 1968; Cambon & Jacquin 1989).

On the other hand, in the case of pure stratification ($f = 0, N \neq 0$), the above results reduce to the results described in 2.1.

In the special case of $N = f$, the dispersion relation for the inertial gravity wave gives $a = N = f$, showing that the group velocity of the wave is zero and the wave energy does not propagate. The integration in (2.53) can be done exactly to give the variances and the covariances at an arbitrary time. The results become

$$\overline{\rho u_3}(t) = \frac{2}{15} N E_0^{(C)} (\sin Nt + 2 \sin 2Nt), \tag{2.54}$$

$$\overline{u_1^2}(t) = \overline{u_2^2}(t) = \frac{2}{3}KE_0 + \frac{2}{15}E_0^{(C)}(\cos Nt - 1), \tag{2.55}$$

and

$$\overline{u_3^2}(t) = \frac{2}{3}KE_0 + \frac{4}{15}E_0^{(C)}(\cos 2Nt - 1). \tag{2.56}$$

We note that when $N = f$, oscillations in the variances and the covariances do not decay with time, which is in contrast to the case of $N \neq f$ In this case, $a(= N = f)$ is independent of θ so that all the spectral components oscillate at the same period $2\pi/N(= 2\pi/f)$, independent of the direction of the wave number and the three-dimensional spectra. Then there is an inviscid decay of oscillation, and the energies never reach constant values.

It is also important to note that $\overline{u_1^2}(= \overline{u_2^2})$ contains only the $\cos Nt$ component and not $\sin 2Nt$ or $\cos 2Nt$, showing that the horizontal kinetic enrgy oscillates slower than the vertical kinetic energy and the potential energy. As will be discussed later, slow oscillation with frequency N has been observed in DNS (Figure 2.11) when the initial turbulence is anisotropic and $N = f$ is satisfied. This is not due to the initial anisotropy but, rather, to $N = f$.

2.2.5 Initially axisymmetric turbulence

Because the atmospheric and oceanic flows are often nearly horizontal, it is important to determine whether different behaviors occur for initially axisymmetric turbulence. If we assume an initially axisymmetric and purely horizontal turbulence that satisfies $\overline{u_1^2}(0) = \overline{u_2^2}(0)(= KE_0)$ and $\overline{u_3^2}(0) = 0$, and also assume that the Reynolds stresses have zero helicity (Herring, 1974; Schumann & Patterson, 1978). The energy components can be calculated as

$$\begin{aligned}\overline{u_1^2}(t) &= \overline{u_2^2}(t) = \frac{1}{2}KE_0 \int_0^\pi d\theta \frac{\sin\theta}{a^4}\left[\left(a^2 + f^2\cos^2\theta(\cos at - 1)\right)^2 + a^2 f^2 \cos^4\theta \sin^2 at\right] \\ &+ \frac{N^2}{2}PE_0 \int_0^\pi d\theta \frac{\sin^3\theta\cos^2\theta}{a^4}\left[f^2(1-\cos at)^2 + a^2\sin^2 at\right]^2,\end{aligned} \tag{2.57}$$

and

$$\overline{u_3^2}(t) = f^2 KE_0 \int_0^\pi d\theta \frac{\sin^3\theta\cos^2\theta}{a^2}\sin^2 at + N^2 PE_0 \int_0^\pi d\theta \frac{\sin^5\theta}{a^2}\sin^2 at. \tag{2.58}$$

In contrast to the initially isotropic turbulence, pure rotation ($f \neq 0, N = 0$) modifies the distributions between the horizontal and vertical kinetic energies.

In the special case of $N = f$, the exact solutions become

$$\overline{u_1^2}(t) = \overline{u_2^2}(t) = \frac{11}{15}KE_0 + \frac{4}{15}PE_0 + \frac{4}{15}(KE_0 - PE_0)\cos Nt, \tag{2.59}$$

$$\overline{u_3^2}(t) = \frac{2}{15}(KE_0 + 4PE_0)(1 - \cos 2Nt). \tag{2.60}$$

We note again that, when $N = f$, oscillations in the variances and the covariances do not decay with time, as discussed in the case of initially isotropic turbulence (2.2.4).

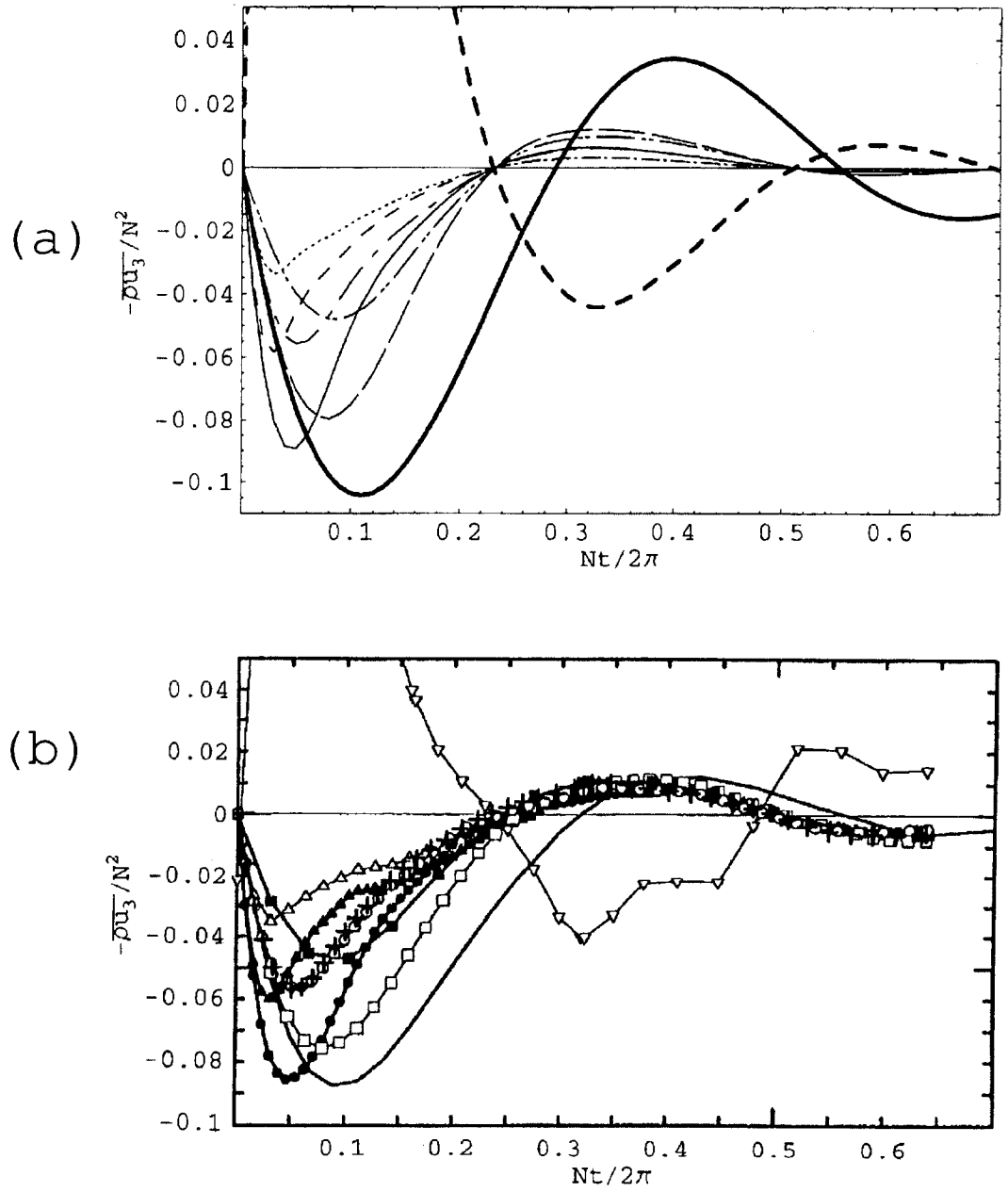

Fig. 2.10: **Time development of the vertical density flux** $-\overline{\rho u_3}/N^2$ for initially isotropic stably stratified rotating turbulence. (a) RDT($Pr = 1$): ————, $N = 2, f = 0$; ————, $N = 1, f = 10$; - - - - $N = 1, f = 20$; — — —, $N = 2, f = 10$; — . — . —, $N = 2, f = 20$; ....., $N = 2, f = 40$; — . . — . . —, $N = 4, f = 20$; – – – –, $PE_0 = 4KE_0, N = 2, f = 20$. (b) DNS by Iida & Nagano(1999)($Pr = 0.71$): ————,$N = 2, f = 0$; •, $N = 1, f = 10$; ▲, $N = 1, f = 20$; ■, $N = 2, f = 10$; ○, $N = 2, f = 20$; +, $N = 2, f = 20$ (solution of the linearized equations); △,$N = 2, f = 40$; ■, $N = 4, f = 20$; ▽, $PE_0 \neq 0, N = 2, f = 20$.

2.2.6 Unstable stratification

When the stratification is unstable, the most unstable mode grows fastest and will become dominant. Because of the exponential growth of that mode, the turbulence energy will become large and the assumption of linearity will break down in a short time.

However, determining which mechanisms work in this transition is still of some interest. The comparison of RDT with DNS and experiments will show that even for unstable stratification, the agreement is good at least for the initial time development.

When the stratification is unstable ($N^2 < 0$), the frequency a becomes purely imaginary for $\theta_0 < \theta < \pi - \theta_0$, where $\theta_0 = \tan^{-1}(-f^2/N^2)^{1/2}$ satisfies $0 \le \theta_0 \le \pi/2$. For this region, we then use $\cos at = \cosh(bt)$, $\sin at = \frac{1}{i}\sinh(bt)$, where $b = ia$. Then, when the initial turbulence is isotropic, the vertical density (heat) flux becomes

$$\begin{aligned}\overline{\rho u_3}(t) &= \frac{N^2}{2}E_0^{(C)}\left(\int_0^{\theta_0} + \int_{\pi-\theta_0}^{\pi}\right)d\theta\frac{\sin^3\theta}{a^3}\sin at(N^2\sin^2\theta\cos at + f^2\cos^2\theta) \\ &+ \frac{N^2}{2}E_0^{(C)}\int_{\theta_0}^{\pi-\theta_0}d\theta\frac{\sin^3\theta}{b^3}\sinh bt(N^2\sin^2\theta\cosh bt + f^2\cos^2\theta). \qquad (2.61)\end{aligned}$$

The normalized vertical density flux in the long-time limit becomes

$$\frac{\overline{\rho u_3}}{\overline{\rho^2}^{\frac{1}{2}}\overline{u_3^2}^{\frac{1}{2}}}(t\to\infty) = -1. \qquad (2.62)$$

We should note that this long-time limit value is independent of $E_0^{(C)}$; i.e., independent of the initial conditions.

2.2.7 Vertical vorticity

The variance of the vertical vorticity for initially isotropic turbulence can be calculated as

$$\begin{aligned}\overline{\omega_3^2}(t) &= \int\Phi_{\omega_3\omega_3}d\vec{k} = \int\overline{\hat{\omega}_3\hat{\omega}_3^*}d\vec{k} \\ &= \frac{1}{4}\overline{\vec{\omega}_0^2}\int_0^{\pi}d\theta\frac{\sin^3\theta}{a^4}\left[\left(a^2 - f^2\cos^2\theta(1-\cos at)\right)^2 + a^2f^2\cos^2\theta\sin^2 at\right] \\ &+ f^2N^2\int_0^{\infty}dkk^2S(k)\int_0^{\pi}d\theta\frac{\sin^5\theta\cos^2\theta}{a^4}(1-\cos at)^2, \qquad (2.63)\end{aligned}$$

where

$$\overline{\vec{\omega}_0^2} = \overline{\omega_{10}^2 + \omega_{20}^2 + \omega_{30}^2} = 2\int_0^{\infty}k^2E(k)dk, \qquad (2.64)$$

denotes twice the initial enstrophy.

2.2.8 Comparison with DNS and experiments

The results will now be compared with DNS and laboratory experiments.

Figure 2.10 shows the time development of the vertical density flux in the stablly stratified rotating turbulence. The RDT solutions with modification by viscosity and diffusion ($Pr = 1$, i.e. $\nu = \kappa$) become

$$-\frac{1}{N^2}\overline{\rho u_3}(t) = -\frac{1}{2}E_0^{(C)}\int_0^{\pi}d\theta\frac{\sin^3\theta}{a^3}\sin at(N^2\sin^2\theta\cos at + f^2\cos^2\theta)\frac{1}{(1+2\nu k_0^2t)^{3/2}}, \qquad (2.65)$$

and the long-time asymptotics become

$$-\frac{1}{N^2}\overline{\rho u_3}(t) = -\frac{1}{4N}E_0^{(c)}\left(\frac{\pi N}{t|N^2-f^2|}\right)^{\frac{1}{2}}\sin\left(2Nt \pm \frac{\pi}{4}\right)\frac{1}{(1+2\nu k_0^2 t)^{3/2}}, \tag{2.66}$$

where the sign $\pm$ represents $+$ when $f > N$, and $-$ when $f < N$.

The overall agreement between RDT and DNS is good. There is a phase difference between the case of $N = 2, f = 0$ and all the other cases. When there is no rotation, $N > f$ is satisfied and the flux is proportional to $\sin(2Nt - \pi/4)$, showing the phase delay. On the other hand, when rapid rotation is imposed, as it is in all the other cases, $N < f$ is satisfied and the flux is proportional to $\sin(2Nt + \pi/4)$, showing the phase advance. This is why in DNS the oscillation period appeared to be longer in the non-rotating case. The theoretical prediction of zeros by the long-time approximation is $Nt/2\pi = 0.3125, 0.5625, \ldots$ when $f < N$, and $Nt/2\pi = 0.1875, 0.4375, \ldots$ when $f > N$. The time difference in zeros is $1/8 = 0.125$. Although the method of the stationary phase is a long-time approximation and is formally applicable only at large times, it gives a good approximation even for $Nt = O(1)$.

At later times ($0.05 < Nt/2\pi < 0.2$), the rotation effects begin to work, but, as (2.66) suggests, the amplitude of the oscillation becomes approximately proportional to f^{-1}, provided that $f \gg N$ is satisfied as it is in the cases described in Figure 2.10. This is also observed in Figure 2.10a,b, noting that three values are used for f (=10, 20, and 40). The results for $f = 40$ show the largest amplitude, and the results for $f = 10$ show the smallest amplitude. However, the rotation effect, except for its effect on the amplitude as shown by (2.66), diminishes rapidly with time, and the time oscillation period ($= 2N$) is equal to twice the stratification parameter N. The amplitude difference for different values of f (and N) in a long time is smaller in DNS than in RDT. One possible explanation is the effect of nonlinearity.

In Figure 2.11, the effects of initial anisotropy (axisymmetric and purely horizontal turbulence) on stably stratified rotating turbulence are shown for the case of no initial potential energy ($PE_0 = 0$). We should note, however, that the results given here are for a special case of $N = f$ and the exact RDT solutions become (2.59) and (2.60) with the viscosity and diffusion effects ($Pr = 1$),

As is clear in (2.59) and (2.60), the horizontal kinetic energy $\overline{u_1^2}(= \overline{u_2^2})$ oscillates with frequency N in contrast to the other variances and covariances. This is also clearly seen in the DNS results. It is important to note that this frequency difference is due to the resonant condition $N = f$ and not to the initial anisotropy. Even when the initial turbulence is isotropic, we found the same results as described in 2.2.4. We should also note that decay of the amplitude occurs with time when $N = f$ is purely the viscosity/diffusion effect and not due to the inviscid mechanism.

Figure 2.12 shows the time-development of the normalized vertical density flux under unstable stratification with isotropic initial condition. All the curves for $-\overline{\rho u_3}/(\overline{\rho^2}\,\overline{u_3^2})^{1/2}$ asymptote to 1 in a long time. RDT results (Figure 2.12a) show the value calculated by using (2.60) for $\overline{\rho u_3}$ and other similar expressions for $\overline{\rho^2}$ and $\overline{u_3^2}$.

In DNS, there are two lines for the same $|N^2|^{1/2}/f$ but for different values of $|N^2|^{1/2}$ and f. These two lines almost coincide. Examination of the RDT solutions for the normalized vertical density flux shows that the value depends on at, f/a and $|N^2|^{1/2}/f$. Since at is determined by ft and $|N^2|^{1/2}/f$ except for θ, and f/a is determined by $|N^2|^{1/2}/f$, the flux is determined only by $|N^2|^{1/2}/f$ and ft. Then, for fixed ft, it is

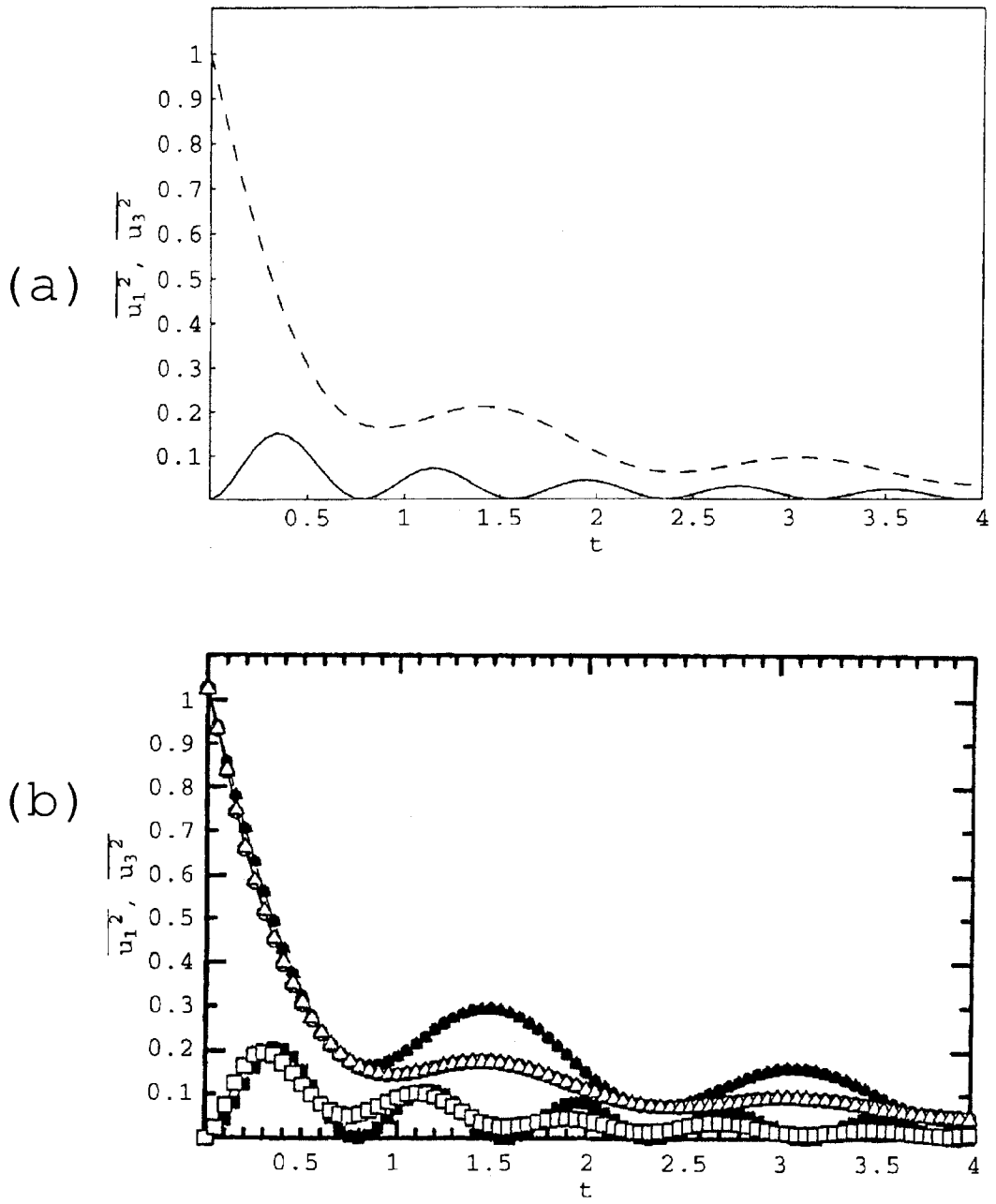

Fig. 2.11: **Time development of the horizontal and vertical kinetic energy for initially axisymmetric and two-dimensional stably stratified rotating turbulence** with $N = f(= 4)$. (a) RDT ($Pr = 1$): - - -,$\overline{u_1^2}(= \overline{u_2^2})$; ————,$\overline{u_3^2}$. (b) DNS by Tsujimura, Iida & Nagano (1998)($Pr = 0.71$). nonlinear: ○,$\overline{u_1^2}$; △,$\overline{u_2^2}$; ■,$\overline{u_3^2}$. linear: ●,$\overline{u_1^2}$; ▲,$\overline{u_2^2}$; ■,$\overline{u_3^2}$. The word linear means the solution of the linearised Navier-Stokes equations.

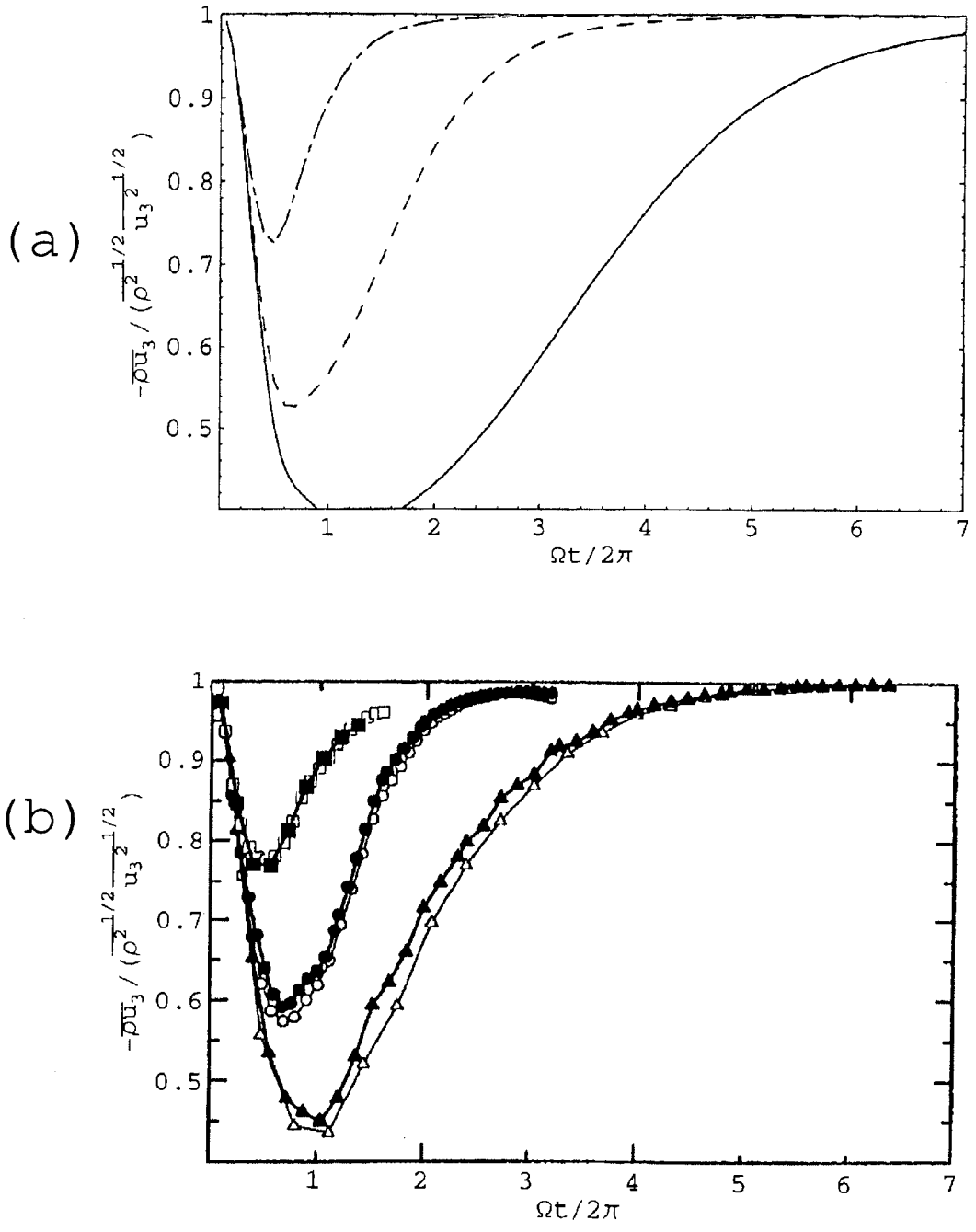

Fig. 2.12: **Time development of the normalized vertical density flux for initially isotropic unstably stratified rotating turbulence.** (a) RDT($Pr = 1$): ——,$|N^2|^{1/2}/f = 0.05$; — — — —,$|N^2|^{1/2}/f = 0.1$; — . — . —,$|N^2|^{1/2}/f = 0.2$. (b) DNS by Iida & Nagano (1999)($Pr = 0.71$): △,$|N^2|^{1/2} = 2, f = 40(|N^2|^{1/2}/f = 0.05)$; ▲,$|N^2|^{1/2} = 1, f = 20(|N^2|^{1/2}/f = 0.05)$; ○,$|N^2|^{1/2} = 2, f = 20(|N^2|^{1/2}/f = 0.1)$; ●,$|N^2|^{1/2} = 1, f = 10(|N^2|^{1/2}/f = 0.1)$; ■,$|N^2|^{1/2} = 2, f = 10(|N^2|^{1/2}/f = 0.2)$; ■,$|N^2|^{1/2} = 4, f = 20(|N^2|^{1/2}/f = 0.2)$.

determined solely by $|N^2|^{1/2}/f$. The agreement of the two curves supports the importance of the linear mechanisms, showing that there are no other parameters that affect the normalized vertical density flux.

Figure 2.13 shows the time development of the vertical vorticity variance for initially isotropic unstably stratified rotating turbulence. The RDT results in Figure 2.13a show the function given by (2.63) with $S(k) = 0$ since there is no initial potential energy in DNS. Combined with the effects of viscosity and diffusion, the RDT results correspond to DNS (but with $Pr = 1$) are

$$\overline{\omega_3^2}(t) = \frac{1}{4}\overline{\omega_0^2}\int_0^\pi d\theta \frac{\sin^3\theta}{a^4}\left[\left(a^2 - f^2\cos^2\theta(1-\cos at)\right)^2 + a^2 f^2\cos^2\theta\sin^2 at\right] \times \frac{1}{(1+2\nu k_0^2 t)^{5/2}}. \tag{2.67}$$

In the inviscid ($\nu = 0$) case, RDT results for the vertical vorticity are again determined solely by ft and $|N^2|^{\frac{1}{2}}/f$. Then for fixed ft, the vertical vorticity variance depends only on $|N^2|^{\frac{1}{2}}/f$. Then, in Figure 2.13 where $(\overline{\omega_3^2})^{1/2}/(f/2)$ is plotted, the difference due to f should appear. Indeed, both in RDT and DNS, the value of $(\overline{\omega_3^2})^{1/2}/(f/2)$ for the same $|N^2|^{\frac{1}{2}}/f$ but for f twice as large initially shows the half value ($t = 0$). In a long time, the two lines almost merge into one line, but this is actually an accidental agreement due to the effect of viscosity and diffusion.

Figure 2.14 shows the time development of the kinetic energies for initially isotropic unstably stratified rotating turbulence with no initial potential energy ($PE_0 = 0$). Initial decay is again due to the viscosity of the fluid. Inviscid RDT gives a monotonic increase of both the horizontal and vertical kinetic energies. However, the viscosity and diffusion effects initially appear as the leading order correction to the kinetic energies. Consequently, the effect of viscous damping appears first and then the growth due to unstable stratification appears later. The initial decay is stronger in the horizontal kinetic energy $\overline{u_1^2}$ than in the vertical kinetic energy $\overline{u_3^2}$. In their experiments on non-rotating unstably stratified fluids, Nagata & Komori (2000) (see their figure 2a) found the similar behavior.

2.2.9 Conclusions

In this study, we solved the RDT equations for both stably and unstably stratified rotating turbulence when the initial turbulence is either isotropic or axisymmetric.

Our results showed good agreement with those of DNS, including the fact that the rotation modifies the energy distribution between the kinetic energy and the potential energy. However, the effects of rotation on the 'unsteady' aspects of the stratified turbulence are not very large because the Coriolis parameter f is always coupled with $\cos\theta$ or the vertical wave number k_3 in the form of $f\cos\theta$ or fk_3, which vanishes for the dominantly contributing angle $\theta = \pi/2$ to the variances and the covariances. The wave number direction that makes the most contribution (i.e., the horizontal direction ($k_3 = 0$) or the barotropic mode), is the same as that in the non-rotating stratified turbulence. Therefore, the stratification effects dominate the unsteady aspects of turbulence even in the presence of system rotation.

In the special case of $N = f$, the time oscillations of the energies and the fluxes do not show inviscid decay like $\propto t^{-1/2}$ observed in the general case of $N \neq f$, which includes the

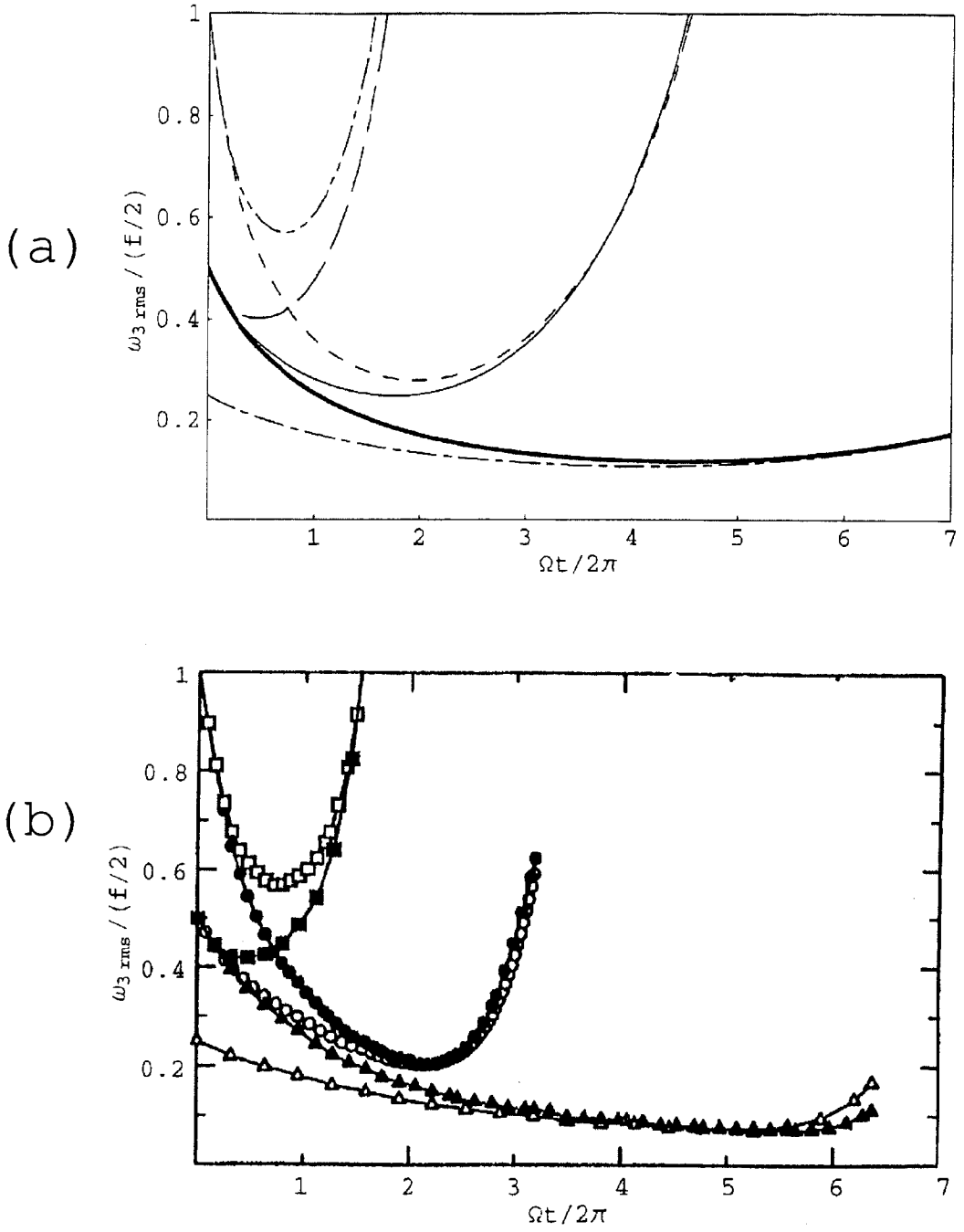

Fig. 2.13: **Time development of $(\overline{\omega_3^2})^{1/2}/(f/2)$ for initially isotropic unstably stratified rotating turbulence.** (a) RDT($Pr = 1$): —.—.—.—,$|N^2|^{1/2} = 2, f = 40(|N^2|^{1/2}/f = 0.05)$; ——————,$|N^2|^{1/2} = 1, f = 20(|N^2|^{1/2}/f = 0.05)$; – – – – – –,$|N^2|^{1/2} = 2, f = 20(|N^2|^{1/2}/f = 0.1)$; – – – – – –,$|N^2|^{1/2} = 1, f = 10(|N^2|^{1/2}/f = 0.1)$; — . . — . . —,$|N^2|^{1/2} = 2, f = 10(|N^2|^{1/2}/f = 0.2)$; — — — —,$|N^2|^{1/2} = 4, f = 20(|N^2|^{1/2}/f = 0.2)$. (b) DNS by Iida & Nagano (1999)($Pr = 0.71$): △,$|N^2|^{1/2} = 2, f = 40(|N^2|^{1/2}/f = 0.05)$; ▲,$|N^2|^{1/2} = 1, f = 20(|N^2|^{1/2}/f = 0.05)$; ○,$|N^2|^{1/2} = 2, f = 20(|N^2|^{1/2}/f = 0.1)$; ●,$|N^2|^{1/2} = 1, f = 10(|N^2|^{1/2}/f = 0.1)$; ■,$|N^2|^{1/2} = 2, f = 10(|N^2|^{1/2}/f = 0.2)$; ■,$|N^2|^{1/2} = 4, f = 20(|N^2|^{1/2}/f = 0.2)$.

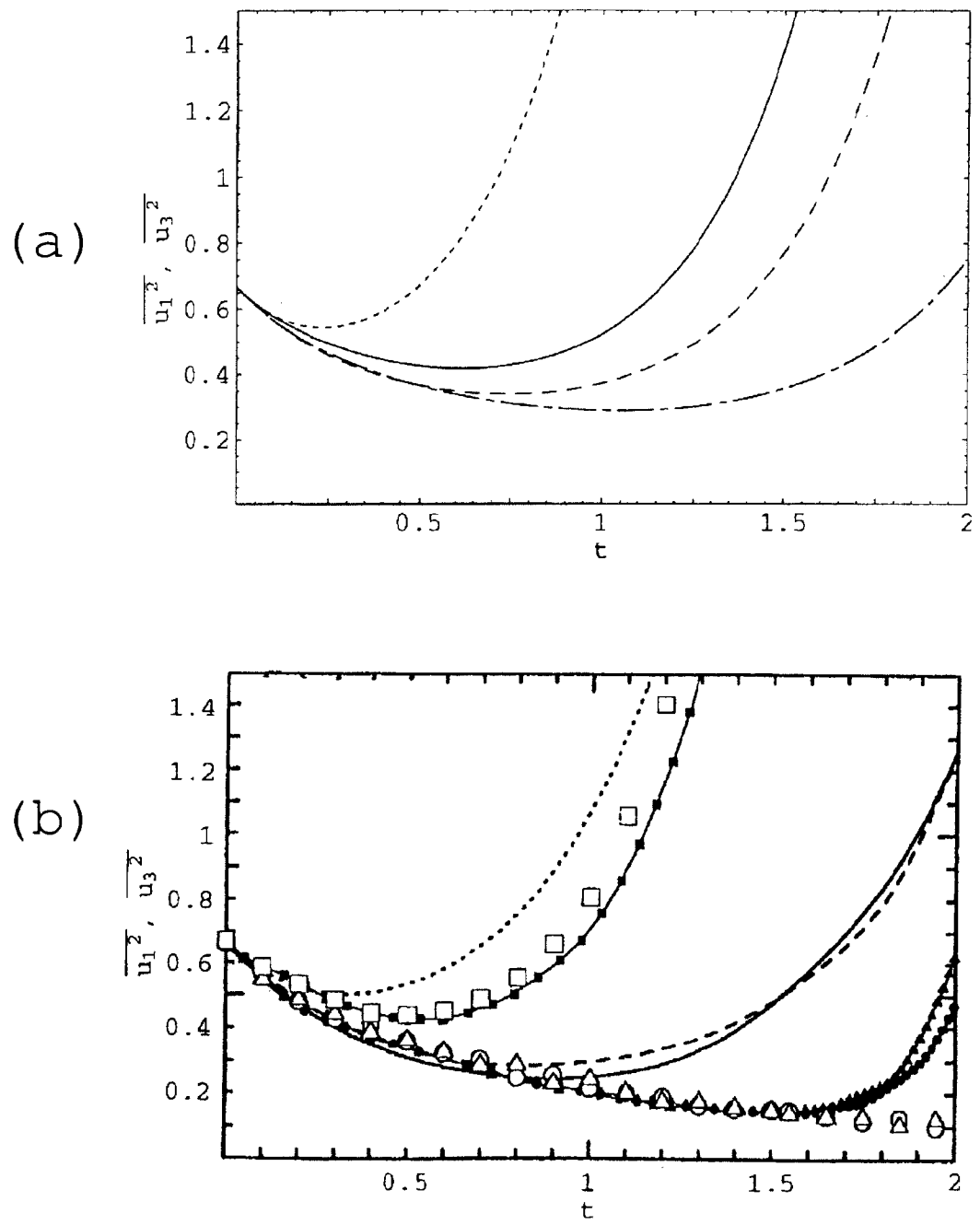

Fig. 2.14: **Time development of the horizontal and vertical kinetic energy for initially isotropic unstably stratified rotating and non-rotating turbulence.** ($|N^2|^{1/2} = 2, f = 20$) (a) RDT ($Pr = 1$): - - - -,$\overline{u_1^2}(= \overline{u_2^2})$ non-rotating; —.—.—,$\overline{u_1^2}(= \overline{u_2^2})$ rotating; .....,$\overline{u_3^2}$ non-rotating; ————,$\overline{u_3^2}$ rotating. (b) DNS by Iida & Nagano (1999)($Pr = 0.71$). Nonlinear, non-rotating: ————,$\overline{u_1^2}$; - - - -,$\overline{u_2^2}$; .....,$\overline{u_3^2}$. nonlinear, rotating: •,$\overline{u_1^2}$; ▲,$\overline{u_2^2}$; ■,$\overline{u_3^2}$. linear, rotating: ○,$\overline{u_1^2}$; △,$\overline{u_2^2}$; ■,$\overline{u_3^2}$. The word "linear" means the solution of the linearized Navier-Stokes equations.

case of pure stratification ($f = 0$) (cf. 2.1). Thus, the energy components never reach constant values. This is because all the wave-number components oscillate in phase, irrespective of their directions, so that the contributing components are not restricted to the horizontal wave-numbers. We note that, in this case, the exchange between the horizontal kinetic energy and the potential energy occurs at low frequency N, and the horizontal energies $\overline{u_1^2}$ and $\overline{u_2^2}$ oscillate at that frequency. On the other hand, the energy exchange at the normal high frequency $2N$ occurs exclusively between the vertical kinetic energy and the potential energy.

In the case of pure rotation ($f \neq 0, N = 0$), solutions by RDT showed that any turbulence initially axisymmetric around the vertical axis returns to isotropy by linear mechanisms. This is in agreement with the previous DNS and the numerical solutions of RDT equations with viscosity (Cambon & Jacquin 1989).

It is of interest to note that the time development of even the small scale characteristics of turbulence as represented by vertical vorticity could be explained well by RDT, although further studies on the energy spectra would be necessary to clarify this point.

The RDT for unstably stratified results explains that the initial decay in the time development of the kinetic energy components is due to viscosity effects that initially become dominant; the growth due to unstable stratification appears at later times. This also agrees with the results of previous DNS and the experiments. It may be concluded that the linear processes described by RDT are dominant at least for a relatively short time before the exponential growth of turbulence due to instability, and the subsequent nonlinear saturation of the growth becomes dominant for $|N^2|^{1/2}t > O(1)$.

2.3 Passive Scalar Diffusion in Stratified Turbulence

2.3.1 Introduction

Passive scalar diffusion in stratified turbulence is generally relevant to pollution problems, though few fundamental studies concentrateing on the difference between passive and active (i.e. heat or density) scalars have been conducted. It is true that if the initial conditions and the molecular diffusion coefficients are the same in the passive and active scalars, the solution is the same and the turbulent diffusion coefficients should also be the same. Our question then becomes, "Under which conditions do they become different?".

In one previous study, for exmple, Warhaft (1976) calculated the vertical fluxes of passive and active scalars using the turbulence model proposed by Launder (1975) on the pressure-strain term, and showed the possibility that the turbulent diffusion coefficient for the passive and active scalars becomes different particularly if the cross-correlation coefficient between the active and passive scalars is small. However, most of the discussions in the literature are based on the energy-flux budget equations for *stationary* turbulence; the effects of unsteadiness or the initial conditions of turbulence have not been considered.

One of the first fundamental numerical simulations for the passive scalar diffusion in stratified turbulence (but with mean shear) was performed by Kaltenbach, Gerz and Schumann (1994). They investigated the time development of the cross-correlation coefficients between the passive scalar c, active scalar ρ, and the vertical velocity u_3 (i.e., $R_{c\rho}$, R_{c3} and $R_{\rho 3}$) and found that $R_{c\rho}$ reaches a rather large value (≥ 0.8) in a long time even when there is no initial correlation between c and ρ ($R_{c\rho}(t=0)=0$).

The first laboratory experiments that investigated the effects of initial conditions were performed by Nagata and Komori (2001). In their experiments, the passive scalar was released from a nozzle so that there was no initial correlation between the passive and active scalar ($R_{c\rho}(t=0)=0$). Time development of $R_{c\rho}$ showed that it reaches a small value (~ 0.25), which might be due to the low initial correlation. Indeed, in their previous experiments (Komori & Nagata, 1996), the difference between R_{c3} and $R_{\rho 3}$ was small when ρ and c had a much larger initial correlation, leading to the counter-gradient passive scalar flux under strongly stratified conditions.

In this study, we solve the problem of passive scalar diffusion in stably stratified turbulence for the first time as an "initial value problem", which takes into account all the initial conditions in order to clarify what determines the subsequent time development of the various fluxes. We here use the rapid distortion theory (RDT), which has been found to give accurate solutions for strongly stratified turbulence. The theory is based on the linearized governing equations, and therefore, as noted previously, has limited applicability conditions. However, it is the only theory that can take into consideration the effects of the initial conditions. The results will be useful to determine the suitable initial conditions for future numerical and experimental studies.

2.3.2 RDT equations

We consider an inviscid fluid with uniform vertical density stratification ($d\overline{\rho}/dx_3 = const.$) and with uniform vertical passive scalar gradient ($d\overline{c}/dx_3 = const.$). The governing equations for this system are the same as (2.46)–(2.48) (except that $\mathbf{\Omega}=0$), with an

additional passive scalar equation given by

$$\frac{\partial c}{\partial t} + (\boldsymbol{u} \cdot \boldsymbol{\nabla})c + u_3 \frac{d\overline{c}}{dx_3} = 0, \tag{2.68}$$

where $\overline{c}(x_3)$ is the undisturbed passive scalar distribution and c is the passive scalar perturbation from $\overline{c}(x_3)$. We substitute the spectral decompositions

$$c(\boldsymbol{x}, t) = \sum_{\vec{k}} \hat{c}(\boldsymbol{k}, t) e^{i\vec{k}\cdot\vec{x}}, \tag{2.69}$$

into (2.68) and obtain an additional equation for the spectral component $\hat{c}$.

If we neglect the nonlinear terms in the governing equations, we can obtain the RDT (Rapid Distortion Theory) equations (2.1)–(2.2) and also

$$\frac{d\hat{c}}{dt} = -\gamma \hat{u}_3, \tag{2.70}$$

where $\gamma = d\overline{c}/dx_3$ is the mean passive scalar gradient, which is a constant independent of x_3.

2.3.3 Solutions of RDT equations

Solutions of the RDT equations (2.1), (2.2), and (2.70) give (2.6)–(2.9) and

$$\hat{c}(\boldsymbol{k}, t) = \hat{c}_0 + \frac{\gamma}{N^2}\hat{\rho}_0(1 - \cos at) - \frac{\gamma}{a}\hat{u}_{30} \sin at. \tag{2.71}$$

where a is the angular frequency of the internal gravity wave defined by (2.10).

We note here that $\hat{c}(t)$ has a *steady* term $\hat{c}_0 + (\gamma/N^2)\hat{\rho}_0$, which does not exist in $\hat{\rho}(t)$. As will be shown later, this will lead to a slowly oscillating term with frequency N in $\overline{cu_3}$, which does not appear in $\overline{\rho u_3}$ where only rapidly oscillating components (frequency $2N$) exist. The steady component is determined by $\hat{c}_0$, $\hat{\rho}_0$ and γ/N^2, meaning that the initial conditions as well as the mean active and passive scalar gradient are important.

2.3.4 Fluxes

We assume that the initial fluxes of density and passive scalar are zero, as is the case in the usual experiments for grid turbulence and in the previous DNS, so that

$$\Phi_{\rho i}(\boldsymbol{k}, t = 0) = \frac{1}{2}\overline{\hat{\rho}_0^* \hat{u}_{i0} + \hat{\rho}_0 \hat{u}_{i0}^*} = 0 \ (i = 1, 2, 3), \tag{2.72}$$

$$\Phi_{ci}(\boldsymbol{k}, t = 0) = \frac{1}{2}\overline{\hat{c}_0^* \hat{u}_{i0} + \hat{c}_0 \hat{u}_{i0}^*} = 0 \ (i = 1, 2, 3), \tag{2.73}$$

where the overline denotes the ensemble average.

If we also assume that the initial fluctuations are isotropic, the initial conditions are given by (2.13), (2.14) and

$$\Phi_{cc}(\boldsymbol{k}, 0) = \frac{Q(k)}{4\pi k^2}, \tag{2.74}$$

$$\Phi_{c\rho}(\boldsymbol{k}, 0) = \frac{R(k)}{4\pi k^2}. \tag{2.75}$$

When integrated, these spectra give

$$\overline{c^2}(0) = \int_0^\infty Q(k)dk, \tag{2.76}$$

$$\overline{c\rho}(0) = \int_0^\infty R(k)dk. \tag{2.77}$$

Then integrating in the whole spectral space, we can calculate the variances and the covariances as

$$\begin{aligned}
\overline{c^2}(t) &= \int \Phi_{cc}(\boldsymbol{k},t)2\pi k^2 dk \sin\theta d\theta \\
&= \overline{c^2}(0) + \frac{2\gamma}{N^2}\overline{c\rho}(0) + \frac{\gamma^2}{2N^2}(KE_0 + 6PE_0) \\
&- \frac{\gamma}{N^2}(\overline{c\rho}(0) + 2\gamma PE_0)\int_0^\pi d\theta \sin\theta\cos(Nt\sin\theta) \\
&- \frac{\gamma^2}{4N^2}(KE_0 - 2PE_0)\int_0^\pi d\theta \sin\theta\cos(2Nt\sin\theta),
\end{aligned} \tag{2.78}$$

$$\begin{aligned}
\overline{c\rho}(t) &= -\frac{\gamma}{2}(KE_0 + 2PE_0) + \frac{1}{2}(\overline{c\rho}(0) + 2\gamma PE_0)\int_0^\pi d\theta \sin\theta\cos(Nt\sin\theta) \\
&+ \frac{\gamma}{4}(KE_0 - 2PE_0)\int_0^\pi d\theta \sin\theta\cos(2Nt\sin\theta),
\end{aligned} \tag{2.79}$$

$$\begin{aligned}
\overline{cu_3}(t) &= -\frac{1}{2N}(\overline{c\rho}(0) + 2\gamma PE_0)\int_0^\pi d\theta \sin^2\theta\sin(Nt\sin\theta) \\
&- \frac{\gamma}{4N}(KE_0 - 2PE_0)\int_0^\pi d\theta \sin^2\theta\sin(2Nt\sin\theta).
\end{aligned} \tag{2.80}$$

In the notation of this paper, the turbulent diffusion coefficients for the active (density) and passive scalar fluxes are given by

$$K_\rho(t) = \frac{\overline{\rho u_3}(t)}{N^2}, \tag{2.81}$$

and

$$K_c(t) = -\frac{\overline{cu_3}(t)}{\frac{d\overline{c}}{dx_3}} = -\frac{\overline{cu_3}(t)}{\gamma}. \tag{2.82}$$

Then

$$K_\rho(t) = K_c(t), \tag{2.83}$$

is equivalent to the condition

$$\frac{\overline{cu_3}(t)}{\overline{\rho u_3}(t)} = -\frac{\gamma}{N^2}. \tag{2.84}$$

As is clear in comparison of (2.80) with (2.20), this is equivalent to

$$\overline{c\rho}(0) + 2\gamma PE_0 = 0, \tag{2.85}$$

in the initial condition. Therefore, we can conclude that for the difference between K_ρ and K_c, initial density fluctuation ($PE_0 \neq 0$) is necessary, given that if $PE_0 = 0$, it means $\Phi_{\rho\rho} = 0$ at all wave numbers (i.e., $\hat{\rho} \equiv 0$), so that $\overline{c\rho}(0) = 0$.

We should also note that if $\gamma\overline{c\rho}(0) > 0$ (i.e., if γ and $\overline{c\rho}(0)$ are of the same sign), the difference between $\overline{cu_3}$ and $\overline{\rho u_3}$ becomes larger as $|\overline{c\rho}(0) + 2\gamma PE_0|$ becomes larger. On the other hand, if $\gamma\overline{c\rho}(0) < 0$ (i.e., if γ and $\overline{c\rho}(0)$ are of opposite sign), there exists a possibility of $\overline{c\rho}(0) + 2\gamma PE_0 = 0$ (and hence $K_\rho = K_c$) even if $PE_0 > 0$. Then, the sign of vertical mean gradient γ is important for the difference between K_ρ and K_c.

Above results suggest that, in the usual grid-generated turbulence where $PE_0 \sim 0$ and the initial correlation $\overline{c\rho}(0) \sim 0$ are both small, $\overline{cu_3} \sim (\gamma/N^2)\overline{\rho u_3}$ (i.e., $K_\rho \sim K_c$) holds.

This conclusion is apparently contrary to previous arguments (Warhaft 1976; Kaltenbach et al. 1994) that "When $\overline{c\rho}(0) = 0$, there will be a large difference between $\overline{cu_3}$ and $\overline{\rho u_3}$ in the subsequent time development". However, in previous studies the discussions have been made based on the energy-flux budget equations for "stationary" turbulence, and no considerations was given to the unsteadiness or the initial conditions. On the other hand, we have considered here the effects of the initial conditions explicitly, and have solved the initial-value problem. Differences in the results show that the identification of steadiness or unsteadiness of turbulence is important in modeling the turbulent fluxes.

As is clear in (2.80), the effects of PE_0 and $\overline{c\rho}(0)$ appear as slowly oscillating components with frequency N, and they are superimposed on the rapidly oscillating components with frequency $2N$, which exist independent of the value of $\overline{c\rho}(0) + 2\gamma PE_0$. The slowly oscillating components also appear in $\overline{c^2}$ (cf. (2.78)) and $\overline{c\rho}$ (cf. (2.79)), both of which are related to the passive scalar c.

Kaltenbach et al. (1994) performed a DNS under initial conditions of $\overline{c\rho}(0) = 0$ (and $PE_0 = 0$) with the expectation that initial statistical independence between the passive and active scalars would lead to a subsequent large difference in their turbulent diffusion (see their Fig. 21). The short-time approximations for the correlation coefficients under these conditions can be calculated using (2.78)–(2.80), etc. For example, the correlation coefficient between the passive and active scalars, i.e., $R_{c\rho} = \overline{c\rho}/(\overline{c^2}^{1/2}\overline{\rho^2}^{1/2})$ becomes

$$R_{c\rho}(Nt \ll 1) = -\left(\frac{2\gamma^2 KE_0}{3N^2\overline{c^2}(0)}\right)^{1/2}(Nt) + ..., \tag{2.86}$$

and $R_{c3} = \overline{cu_3}/(\overline{c^2}^{1/2}\overline{u_3^2}^{1/2})$ becomes

$$R_{c3}(Nt \ll 1) = -\left(\frac{2\gamma^2 KE_0}{3N^2\overline{c^2}(0)}\right)^{1/2}(Nt) + ..., \tag{2.87}$$

which agrees with $R_{c\rho}(Nt \ll 1)$. Corresponding to this result ($R_{c\rho} \sim R_{c3}$), $R_{\rho 3} = \overline{\rho u_3}/(\overline{\rho^2}^{1/2}\overline{u_3^2}^{1/2})$ becomes

$$R_{\rho 3}(Nt \ll 1) = 1 + ... \tag{2.88}$$

To confirm these results and also to see the longer time development, we show in Figure 2.15 the time development of $R_{c\rho}$, R_{c3} and $R_{\rho 3}$ obtained using (2.78)–(2.80) and (2.20), which are valid at arbitrary times. Here we have used the same initial conditions as used by Kaltenbach et al. (1994); i.e., $PE_0 = \overline{c\rho}(0) = 0$ and $N^2\overline{c^2}(0)/(\gamma^2 KE_0) = 3.67$.

If $PE_0 = \overline{c\rho}(0) = 0$, all the time developments are determined by $N^2\overline{c^2}(0)/(\gamma^2 KE_0)$ in RDT. For example, R_{c3} at an arbitrary time is given by

$$R_{c3}(t) = \frac{-\frac{1}{4}sign(\gamma)\int_0^\pi d\theta \sin^2\theta \sin(2Nt\sin\theta)}{\left(\frac{N^2\overline{c^2}(0)}{\gamma^2 KE_0} + \frac{1}{2} - \frac{1}{4}\int_0^\pi d\theta \sin\theta\cos(2Nt\sin\theta)\right)^{1/2}\left(\frac{1}{3} + \frac{1}{4}\int_0^\pi d\theta \sin^3\theta\cos(2Nt\sin\theta)\right)^{1/2}}. \tag{2.89}$$

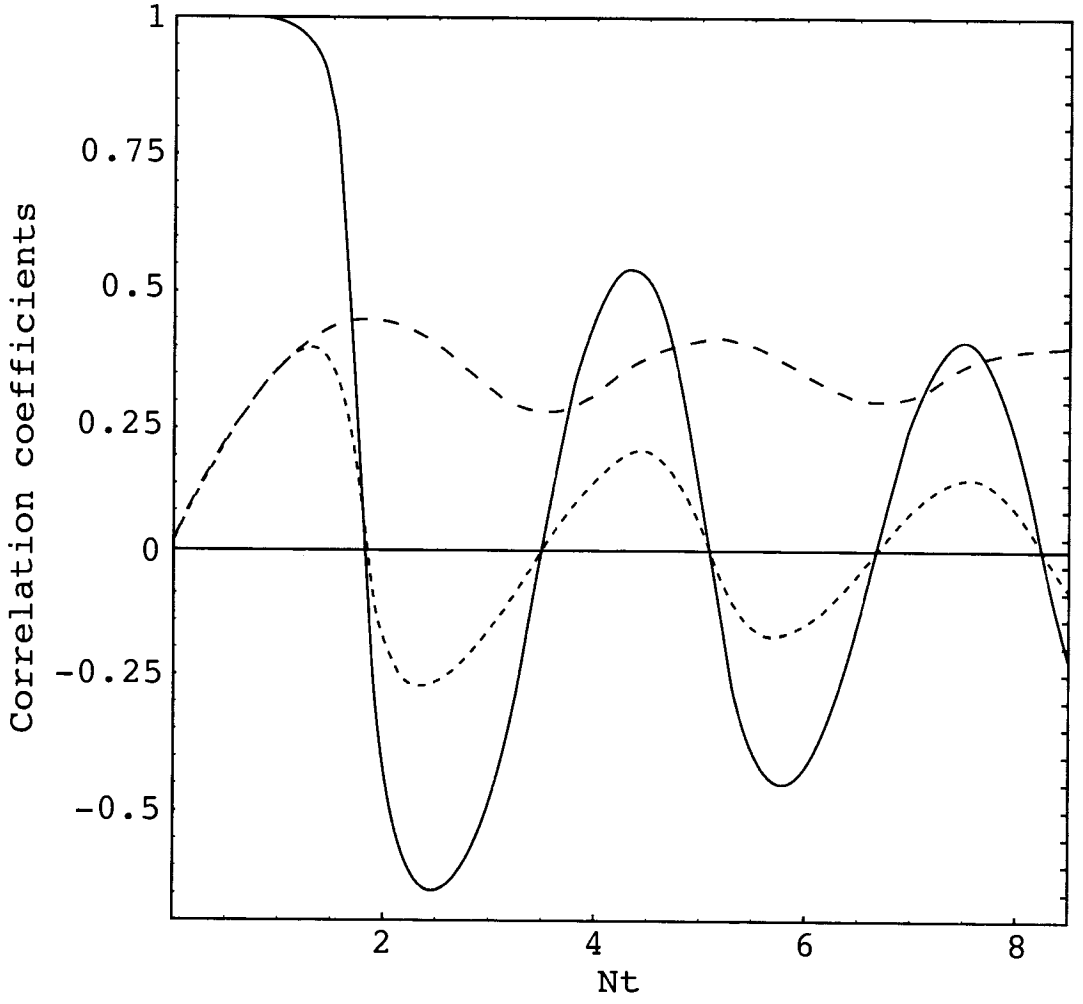

Fig. 2.15: Time development of the correlation coefficients obtained by RDT for $PE_0 = \overline{c\rho}(0) = 0$ and $N^2\overline{c^2}(0)/(\gamma^2 KE_0) = 3.67$. ————, $R_{\rho 3}$; – – – –, $R_{c\rho}$; ·····, R_{c3}.

We should be reminded that due to the mean shear ($Ri = 0.5$) addressed in DNS by Kaltenbach et al., long-time development will not agree with the RDT results obtained for $Ri = \infty$ (no shear). For example, it has been known that the existence of mean shear leads to different $R_{\rho 3}$ in a long time (Holt et al. 1992). However, we can expect good agreement for the short-time ($Nt \leq 1$) development. Indeed, in agreement with Figure 2.15, the DNS by Kaltenbach et al. shows (see their Fig. 21a) that $-R_{c\theta}(= R_{c\rho}) = R_{c3}$ and $-R_{\theta 3}(= R_{\rho 3}) \sim 1$ (θ: temperature fluctuation) for $Nt \ll 1$. In addition, $R_{c\rho}$ and R_{c3} grow in proportion to the non-dimensional time Nt, and the proportionality coefficient is $(2\gamma^2 KE_0/3N^2\overline{c^2}(0))^{1/2} = 0.43$, again in agreement with the RDT predictions.

2.3.5 Conclusions

The effects of initial conditions on the passive and active scalar fluxes in unsteady stratified turbulence have been analyzed using the rapid distortion theory (RDT). Solutions of the RDT equations for the initially isotropic turbulence show that if $PE_0 = \overline{c\rho}(0) = 0$ (more generally, if $\overline{c\rho}(0) + 2\gamma PE_0 = 0$), the turbulent diffusion coefficients satisfy $K_\rho(t) = K_c(t)$ at all times. If, in addition, $\overline{c^2}(0)$ is small $(N^2\overline{c^2}(0)/(\gamma^2 KE_0) \ll 1)$, correlation between active and passive scalars becomes large; i.e., $|R_{c\rho}| \sim 1 (Nt \gg 1)$. This means that the previous argument based on the 'stationality' of turbulence, that the correlation coefficient $R_{c\rho}$ becomes generally small if $\overline{c\rho}(0) = 0$ initially, is not correct in unsteady turbulence. Corresponding to this large correlation, counter-gradient *passive* scalar flux occurs when there is a counter-gradient *active* scalar flux.

In contrast, if $\overline{c^2}(0)$ is large $(N^2\overline{c^2}(0)/(\gamma^2 KE_0) \geq 1)$, the final correlation becomes small; i.e., $|R_{c\rho}| \ll 1 (Nt \gg 1)$. Given that $K_\rho = K_c$ holds under the conditions of $PE_0 = \overline{c\rho}(0) = 0$, this means that $K_\rho = K_c$ does not necessarily correspond to $|R_{c\rho}| = 1$. Therefore, it is not correct to use $|R_{c\rho}| = 1$ as a general criterion for $K_\rho = K_c$. The above results show that the initial conditions and the unsteadiness are important to estimate the turbulent diffusion coefficient in 'unsteady' turbulence.

The results of this study clearly show the possible importance of the initial conditions on the unsteady turbulence, which data will be useful for the parameter determinations in future DNS, experiments, and modeling of the turbulent diffusion.

Earth's rotation and the vertical density stratification of fluids determine the most important/dynamical aspects of geophysical flows. Since the governing equations of those fluids have been well known, they are now solved numerically in the atmospheric and oceanic models quite routinely. However, we can not resolve all the length/time scales at the same time since there is a huge difference in the largest and smallest scales in geophysical flows. This scale difference requires unrealizable vast computer resources, and leads inevitably to the "modelling" of flows/turbulence. But the modelling should depend on the scales, and it implies many uncertainties. Since the flows of rotating stratified fluid consist of vortices and waves, fuller knowledge of them and their interactions, as investigated in this study, would be of great help in constructing the numerical models used for the environmental problems, including the climate prediction. Finally, the authors are grateful to Dr. Naoya Takahashi of University of Electro-Communications for his help in preparing a beautiful TEX-stylefile. Without his tremendous efforts this monograph would never have been completed.

References

Bardina, J., Ferziger, J. H. and Rogallo, R. S. (1985) Effect of rotation on isotropic turbulence: computation and modeling, *J. Fluid Mech.*, **154**: 321–336.

Bartello, P. (1995) Geostrophic adjustment and inverse cascades in rotating stratified turbulence, *J. Atmos. Sci.*, **52**: 4410–4428.

Cambon, C. and Jacquin, L. (1989) Spectral approach to non-isotropic turbulence subjected to rotation, *J. Fluid Mech.*, **202**: 295–317.

Gerz, T. and Yamazaki, H. (1993) Direct numerical simulation of buoyancy-driven turbulence in stably stratified fluid, *J. Fluid Mech.*, **249**: 415-440.

Greenspan, H. P. (1968) *The Theory of Rotating Fluids* (Cambridge University Press, 327pp.)

Herring, J. R. (1974) Approach of axisymmetric turbulence to isotropy, *Phys. Fluids*, **17**: 859–872.

Holt, S. E., Koseff, J. R. and Ferziger, J. H. (1992) A numerical study of the evolution and structure of homogeneous stably stratified turbulence, *J. Fluid Mech.*, **237**: 499.

Hunt, J. C. R., Stretch, D. D. and Britter, R. E. (1988) Length scales in stably stratified turbulent flows and their use in turbulence models, *Stably Stratified Flow and Dense Gas Dispersion* (J.S.Puttock ed., Clarendon Press, 430pp.), 285-321.

Hunt, J. C. R. and Carruthers, D. J. (1990) Rapid distortion theory and the 'problems' of turbulence, *J. Fluid Mech.*, **212**: 497-532.

Iida, O. and Nagano, Y. (1999) Coherent structure and heat transfer in geostrophic flow under density stratification, *Phys. Fluids*, **11**: 368–377.

Itsweire, E. C., Helland, K. N. and Van Atta, C. W. (1986) The evolution of grid-generated turbulence in a stably stratified fluid, *J. Fluid Mech.*, **162**: 299-338.

Kaltenbach, H.-J., Gerz, T. and Schumann, U. (1994) Large eddy simulation of homogeneous turbulence and diffusion in stably stratified shear flow, *J. Fluid Mech.* **280**: 1.

Komori, S., Ueda, H., Ogino, F. and Mizushina, T. (1983) Turbulence structure in stably stratified open-channel flow, *J. Fluid Mech.*, **130**: 13-26.

Komori, S. and Nagata, K. (1996) Effects of molecular diffusivities on counter-gradient scalar and momentum transfer in strong stable stratification, *J. Fluid Mech.*, **326**: 205–237.

Launder, B. E. (1975) On the effects of a gravitational field on the turbulent transport of heat and momentum, *J. Fluid Mech.*, **67**: 569.

Lienhard, J. H. and Van Atta, C. W. (1990) The decay of turbulence in thermally stratified flow, *J. Fluid Mech.*, **210**: 57-112.

M'etais, O., Bartello, P., Garnier, E., Riley, J.J. and Lesieur, M. (1996) Inverse cascade in stably stratified rotating turbulence, *Dyn. Atmos. Oceans*, **23**: 193–203.

M'etais, O. and Herring, J. (1989) Numerical simulations of freely evolving turbulence in stably stratified fluids, *J. Fluid Mech.*, **202**: 117-148.

Nagata, K and Komori, S. (2000) The effects of unstable stratification and mean shear on the chemical reaction in grid turbulence, *J. Fluid Mech.*, **408**: 39–52.

Nagata, K. and Komori, S. (2001) The difference in turbulent diffusion between active and passive scalars in stable thermal stratification, *J. Fluid Mech.*, **430**: 361.

Nai-ping, L., Neff, W. D. and Kaimal, J. C. (1983) Wave and turbulence structure in a disturbed nocturnal inversion, *Studies of Nocturnal Stable Layers at BAO.* 83 (Kaimal, J. C. ed., NOAA), 53-73.

Riley, J. J., Metcalfe, R. W. and Weissman, M. A. (1981) Direct numerical simulations of homogeneous turbulence in density stratified fluids, *Nonlinear Properties of Internal Waves. AIP Conference Proc. vol. 76* (American Institute of Physics, 351pp.), 79-112.

Schumann, U. and Patterson, G. S. (1978) Numerical study of the return of axisymmetric turbulence to isotropy, *J. Fluid Mech.*, **88**: 711-735.

Townsend, A. A. (1976) *The structure of turbulent shear flow* (Cambridge University Press, 429pp.)

Tsujimura, S., Iida, O. and Nagano, Y. (1998) Effects of rotation on unstably stratified turbulence, *Proc. Int. Conf. on Turbulent Heat Transfer 2, Manchester, U. K. vol.1* 5-58 – 5-71.

Warhaft, Z. (1976) Heat and moisture flux in the stratified boundary layer, *Q. J. Roy. Met. Soc.*, **102**: 703.

Yoon, K. and Warhaft, Z. (1990) The evolution of grid generated turbulence under conditions of stable thermal stratification, *J. Fluid Mech.*, **215**: 601-638.

CGER'S SUPERCOMPUTER MONOGRAPH REPORT
Back Numbers

Vol. 1 CGER-I021-'96
TURBULENCE STRUCTURE AND CO_2 TRANSFER AT THE AIR-SEA INTERFACE AND TURBULENT DIFFUSION IN THERMALLY-STRATIFIED FLOWS

Vol. 2 CGER-I022-'96
A Transient CO_2 Experiment with the MRI CGCM -Annual Mean Response -

Vol. 3 CGER-I025-'97
Study on the Climate System and Mass Transport by a Climate Model

Vol. 4 CGER-I028-'97
Development of a global 1-D chemically radiatively coupled model and an introduction to the development of a chemically coupled General Circulation Model

Vol. 5 CGER-I035-'99
THREE-DIMENSIONAL CIRCULATION MODEL DRIVEN BY WIND, DENSITY, AND TIDAL FORCE FOR ECOSYSTEM ANALYSIS OF COASTAL SEAS

Vol. 6 CGER-I040-2000
Tropical Precipitation Patterns in Response to a Local Warm SST Area Placed at the Equator of an Aqua Planet

Vol. 7 CGER-I045-2001
New Meteorological Research Institute Coupled GCM (MRI-CGCM2)
- Transient Response to Greenhouse Gas and Aerosol Scenarios -

Vol. 8 CGER-I055-2003
Transient Climate Change Simulations in the 21st Century with the CCSR/NIES CGCM under a New Set of IPCC Scenarios

As for the Vol.2 to Vol.8, copies can be obtained from:
Research Integration Section
Center for Global Environmental Research
National Institute for Environmental Studies
16-2, Onogawa, Tsukuba, Ibaraki 305-8506, Japan

All copies in PDF format are available from:
http://www-cger.nies.go.jp/cger-e/e_report/r_index-e.html